Università degli Studi di Padova

DIPARTIMENTO DI FISICA E ASTRONOMIA "GALILEO GALILEI"

Corso di Laurea Magistrale in Astronomia

Tesi di Laurea Magistrale

Analysis of Hollows located on the Mercury High-Magnesium Region

Laureando:
Marco Merusi
Matricola 1133373

Relatore:
Prof. Francesco Marzari

Correlatori:
Dr. Gabriele Cremonese
Dr.ssa Alice Lucchetti

Sommario

Il presente lavoro di tesi è finalizzato ad un'analisi dettagliata di particolari strutture presenti sulla superficie di Mercurio denominate *hollows*. Gli hollows sono depressioni superficiali brillanti rispetto al terreno circostante ed interessanti in quanto la loro natura e composizione non è stata ancora univocamente definita. In questo lavoro sono stati analizzati gli hollows localizzati nella regione di Mercurio caratterizzata da un'elevata abbondanza di Magnesio. Basandosi sui dati presenti in letteratura e analizzando le immagini acquisite dallo strumento MDIS (Mercury Dual Imaging Camera) della missione NASA MESSENGER (MErcury Surface, Space ENvironment, GEochemistry and Ranging), sono stati analizzati gli hollows nella regione ad alto Magnesio per capire se esistesse una qualche correlazione con questo terreno. I gruppi di hollows individuati sono stati divisi a seconda dell'unità geologica in cui si trovano, in particolare abbiamo trovato che sono principalmente concentrati in corrispondenza di crateri da impatto. Sono stati poi selezionati gli hollows localizzati in corrispondenza di particolari parti di crateri quali il fondo del cratere, il picco centrale e il bordo. La presenza di strutture in diverse parti del cratere potrebbe significare che gli hollows siano il risultato di un processo di escavazione di materiale che si trova a diverse profondità nella crosta planetaria. Allo stesso tempo, la presenza di hollows in corrispondenza di materiali piroclastici supporterebbe la teoria per cui gli hollows si formerebbero tramite l'esaurimento di gas volatili da strati di materiale vulcanico. Sono stati poi analizzati gruppi di hollows in maggior dettaglio utilizzando il software ESRI ArcGIS tramite il quale abbiamo misurato il raggio medio e l'area totale. I risultati sulle aree suggeriscono che le nostre misure, diverse da quelle riportate precedentemente in letteratura, siano più realistiche poiché sono state utilizzate immagini ad una più elevata risoluzione. I raggi misurati sono invece simili tra i gruppi di hollows considerati, confermando ulteriormente il fatto che la formazione di hollows potrebbe essere la conseguenza di uno stesso processo (rilascio dello stesso tipo di materiale volatile) e che la differenza tra queste strutture sia principalmente legata al tipo di terreno in cui si formano.

Abstract

The aim of this thesis is the analysis of peculiar structures, named hollows, defined as shallow, rimless, irregular bright depressions on Mercury's surface. These structures are interesting because their nature and composition is still under debate. We focus our attention on hollows located inside a region characterized by a high abundance of Magnesium (HMR, High-Magnesium Region). Thanks to previous datasets published in literature and to images acquired by the MDIS (Mercury Dual Imaging Camera) instrument onboard NASA MESSENGER (MErcury Surface, Space ENvironment, GEochemistry and Ranging) mission, we analyze hollows in order to find any correlation with the geochemical terrain in which they are located. The hollows groups have been studied depending on the geological unit in which they formed, finding that they are mainly concentrated in impact craters. In addition, we found that hollows are located in different parts of impact structures, such as floor, central peak, peak-ring and rim, suggesting that the excavation process forming hollows involves material located at different depths in the Mercury's crust. We also identified hollows in association with pyroclastic material supporting the idea that hollows formed through the depletion of volatiles from volcanic material strata. Finally, we analyzed in greater detail some hollows groups using the ESRI ArcGIS software measuring their area and dimension. The area results suggest that our measurements, being different from what previously reported, are more precise because of the use of higher resolution images. The hollows dimensions result similar between all hollows groups meaning that probably the formation process involving the depletion of volatiles is the same for all hollows. The main difference between hollows is maybe due to the bedrock terrain in which they formed, but this type of difference can be exploited only through further spectral analysis.

Contents

List of Figures

List of Tables

One day on Mercury lasts 1408 hours.
Just like mondays on Earth.

Anonymous

Introduction

The subject of this Master thesis regards the analysis of peculiar geological features on the surface of Mercury, known as hollows. In particular, we focused on those hollows occurring inside a limited region showing a high abundance of Magnesium. Hollows have been described as shallow rimless depressions with irregular shapes and steep walls and characterized by bright floors and halos and a blue hue. They can be found as single entities or in rich clusters and have been principally associated with impacts as they occur mostly within craters and basins, though in some cases they lie on flat or rough terrains not related to impact craters. The study of hollows is relatively recent, as their bright appearance had been observed for the first time by NASA Mariner 10 mission in the Seventies, but the greatest step forward was made thanks to NASA MESSENGER (MErcury Surface, Space ENvironment, GEochemistry, and Ranging) mission, which sent a huge amount of data and images to the Earth during the first half of the current decade. Indeed, our work is based on the data from two instruments of MESSENGER: i) the Mercury Dual Imaging Camera (MDIS), which consisted in the Wide-Angle Camera (WAC, which yielded wide-field images allowing us to frame the geomorphological setting hosting hollows) and the Narrow-Angle Camera (NAC, which returned high-resolution narrow-field images by which we could observe and analyze hollows in greater detail), and ii) the X-Ray Spectrometer (XRS), which measured the abundances of several elements in the top millimeter of Mercury's crust.

In order to fix the general frame of this thesis, in chapter 1 we give an overview of the main physical characteristics of Mercury, the history of observations and exploration of the planet, a description of NASA MESSENGER mission and its instruments MDIS and XRS mentioned above.

Chapter 2 is completely dedicated to the 'state of art' of the scientific research on hollows. Indeed, after an introduction on the different types of terrain units observed on Mercury (each one having a peculiar spectral behavior) in which it is possible to find hollows, we describe the association of hollows with different geological settings (especially craters and parts of craters) and terrain units. Subsequently, the main geomorphological

aspects of hollows are summarized, such as the typical depth and the tendency of hollows to form in regions (latitudinal or longitudinal stripes) and crater slopes which are subject to different lighting conditions. Then, the different formation hypotheses of hollows are reported. Many authors agree on the fact that the shallow depressions generate from a collapse when volatile substances are depleted from volatile-bearing materials in the top layer of the crust. Two kinds of mechanisms are thought to be responsible for the depletion of volatiles: i) an exogenic one, consisting in sputtering by solar wind ions, micrometeorites and photons which destroy the volatile-bearing phases, and ii) an endogenic one, providing that volcanic gases erupted get sequestered beneath a cap rock associated with pyroclastic material, and then exposed to the surface and redistributed by impacts. Both hypotheses can count on observational proofs, the former can be considered as a consequence of correlation between the longitudinal variation of areal extension of hollows and solar insolation, while the latter is supported by the presence of hollows near volcanic pits or vents and in association with pyroclastic material.

Chapter 3 is an overview on the composition of Mercury, and especially its superficial layer. As a result of XRS measurements, *Weider et al.* (2015) retrieved several elemental ratio maps, namely maps showing the relative abundance of different elements with respect to a common species. In the map of Magnesium, we focus on a limited region characterized by a high abundance of this element, known as the High-Magnesium Region. Therefore, we examine the two theories suggested for the formation of this region: the former concerning the impact by a large body, the latter providing volcanic activity and resurfacing.

In chapter 4 we show the detailed analysis that we performed on hollows occurring in the High-Magnesium Region. The base of the analysis consisted in three datasets by *Thomas et al.* (2016) and *Blewett et al.* (2016), including the coordinates and the areal extensions of several hollows groups, defined through the occurrence of hollows within a common crater or within 50 km from each other if lying outside craters. After restricting the analysis to only those in the HMR (fully listed in Appendix A), we divided these groups in four categories, depending on the host setting: floor/rim, peak/peak-ring, smaller craters within larger basins and terrains not related to impacts. We retrieved interesting statistical results coming from the fraction of groups for each category and the areas of the single groups. These results are then correlated with the geological settings in which hollows formed and with the formation hypotheses illustrated in chapter 3. In addition, we performed a more refined analysis on hollows. We selected four hollows groups for each category and mapped all hollows thanks to the software ESRI ArcGIS, in which it was possible to project NAC images containing hollows on a global map of Mercury. Through these measurements, we obtained the mean size of hollows and the

total area of each group, that we compared with the data from the literature suggesting some constraints on the formation mechanism of hollows.

Finally, in the Conclusion chapter we present a summary of all the results retrieved from our analysis and the future work that we can perform in the next future to advance our knowledge of hollows, considering that they will be an important scientific target of the upcoming BepiColombo mission.

Chapter 1

The planet Mercury and its space exploration

1.1 A peculiar terrestrial planet

Having an equatorial diameter of 4878 km, Mercury (figure 1.1) is the smallest of the eight planets forming the Solar System, slightly larger than the Earth's Moon (*Strom*, 1997). It is the closest planet to the Sun, having a highly eccentric elliptical orbit ranging from 0.31 AU ($\sim$ 46 million km) at perihelion to 0.47 AU ($\sim$ 70 million km) at aphelion. This causes Mercury to have a large thermal diurnal variation, oscillating between 100 K and 700 K (*Vasavada et al.*, 1999). While it takes almost 88 terrestrial days to complete a full cycle around the Sun, it rotates around its own axis in 58.6 days, thus fixing a 3:2 resonance between the rotation to revolution periods (*Colombo & Shapiro*, 1966). Furthermore, its orbit is characterized by precession of the perihelion, which has been explained by Einstein's Theory of General Relativity in the last Century (*Einstein*, 1915). According to recent studies (*Smith et al.*, 2012), Mercury has a highly differentiated interior, with a solid inner core (probably of the same size of that of the Earth) and a liquid outer core, both rich in Iron and Nickel, a mantle made of silicates and a rocky superficial crust. The planet has also a dipolar magnetic field much weaker than that of the Earth ($\sim$ 1% in strength, *Ness et al.*, 1974) and despite the small size of Mercury, this field is supposed to be intrinsic and not dynamo-generated (*Stephenson*, 1976; *Aharonson et al.*, 2004). In addition, the observations by NASA MESSENGER mission allowed to discover that the magnetospheric system does not coincide with the planetary sphere, indeed it was possible to infer that the magnetic field of Mercury has an internal axial dipole which is offset by 480 km to the North of the equatorial plane (*Wicht & Heyner*, 2017). Although Mercury has the highest uncompressed density (5.3 g/cm^3) in the Solar System (*Anderson et al.*,

1987), its low mass provides a very weak gravitational attraction not allowing to retain an appreciable atmosphere. However, Mercury is surrounded by a thin exosphere, which is mainly constituted by Sodium, Magnesium, Oxygen, Hydrogen, Potassium and Calcium (*McClintock et al.*, 2016). As a consequence, the pressure at the surface is only 10^{-3} Pa (*Domingue et al.*, 2007). The main physical and orbital features are listed in table 1.1.

(a)   (b)
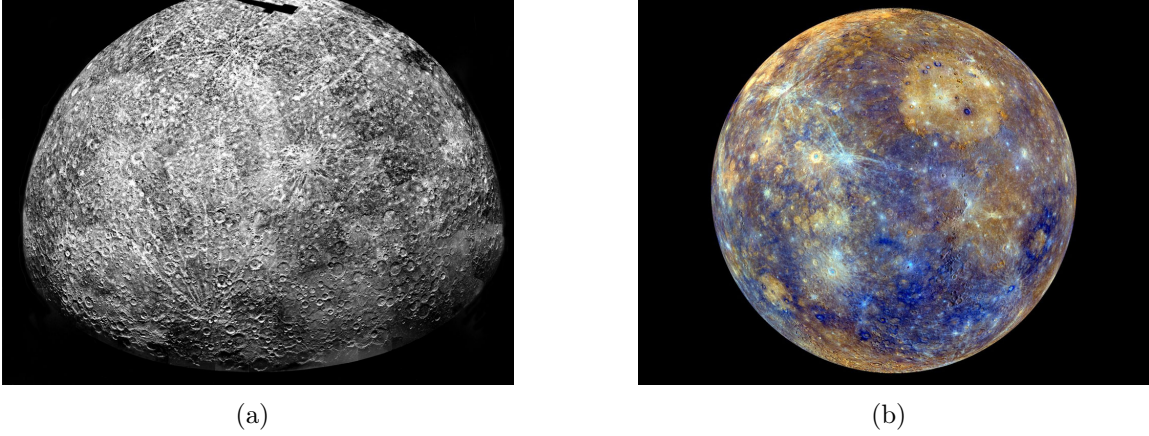
Figure 1.1: *(a) Computer photomosaic of the Southern hemisphere of Mercury composed by images captured by Mariner 10 between 1974 and 1975. (b) Enhanced-color image taken by NASA MESSENGER. The contrasting colours show the differences in the composition of terrains on the planet. Credits: NASA / JHU Applied Physics Lab / Carnegie Inst. Washington.*

(a)

Physical features	
Mass [10^{24} kg]	0.33011
Equatorial radius [km]	2439.7
Mean density [kg/m^3]	5427
Surface gravity [m/s^2]	3.70
Escape velocity [km/s]	4.3
Bond albedo	0.068
Black Body temperature [K]	439.6

(b)

Orbital parameters	
Semi-major axis [10^6 km]	57.91
Sidereal orbit period [Earth days]	87.969
Perihelion [10^6 km]	46.00
Aphelion [10^6 km]	69.82
Orbit inclination [deg]	7.00
Orbit eccentricity	0.2056
Length of day [hours]	4222.6

Table 1.1: *Summary of (a) the main physical features and (b) the orbital parameters of Mercury. Credit: NASA.*

As shown by the images sent to Earth by NASA Mariner 10 and MESSENGER (MErcury Surface, Space ENvironment, GEochemistry and Ranging) missions (which will be illustrated in greater detail in the next section), the surface of Mercury seems to be comparable to the Moon: it is rich of impact craters, basins and terrains of different chemical and mineralogical composition. This is a consequence of the very thin exosphere that cannot protect the planet from meteoric bombardment and, in addition, it is not sufficient to modify the surface through erosion. The density of craters on Mercury is similar to

the one of the Moon for diameters ranging from 128 to 512 km, while is much lower for diameters ranging from 20 to 128 km (*Fassett et al.*, 2011). The study of craters enriching the surface of Mercury allowed to develop a chronostratigraphic classification able to separate the evolution of Mercury in different periods of different lengths (*Neukum et al.*, 2001), as shown in figure 1.2. The chronology of Mercury is organized as the following: Pre-Tolstojan era (prior to 3.97 Gyr), Tolstojan era (started with the formation of Tolstoj basin at 3.97 Gyr), Calorian era (from the formation of Caloris basin at 3.77 Gyr), Mansurian era (from 3.5 to 1 Gyr) and Kuiperian era (from 1 Gyr until the current time).

During Mariner 10 mission, the spherical surface of Mercury was divided into 15 regions named 'quadrangles' (*Davies et al.*, 1978), which are still now in use: two of them cover the polar caps (90ºS to 65ºS and 65ºN to 90ºN), while the other 13 are distributed in three latitudinal stripes. The quadrangles were named after observing albedo features and principal topographic features, such as Raditladi (quadrangle code H-04) and Eminescu (H-09) from the homonym basins.
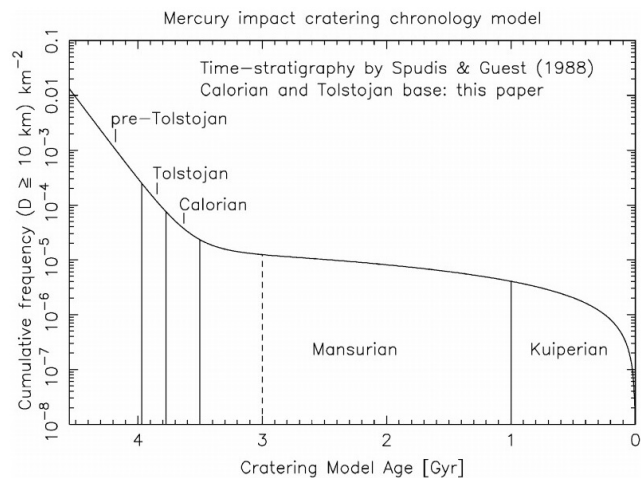
Figure 1.2: *Model of impact cratering chronology of Mercury (Neukum et al., 2001) applied to the time-stratigraphic system (Spudis & Guest, 1988). The cumulative cratering frequency on the y-axis is given for crater sizes D > 10 km. From Neukum et al., 2001.*

1.2   Exploration of Mercury

Already spotted by the Assyrians and the Babylonians, the planet was assigned the name *Hermes* (son of Zeus, messenger of the gods) by the Greeks and his roman homologous was given the name *Mercurius*. The first observations at the telescope were performed by Galileo Galilei (1564-1642) in the 17th Century, though the instrument was not powerful enough to fully resolve the rocky body. Later Giovanni Battista Zupi (1590-1650) was able to detect the phases of Mercury, finally stating that it was orbiting around the Sun, and Pierre Gassendi (1592-1655) first documented its transit in front of our star, based on Kepler's predictions. Between the 19th and the 20th Century Giovanni Schiaparelli (1835-1910) realized detailed maps of Mercury, and subsequently Eugène Michel Antoniadi

(1870-1944) and Percival Lowell (1855-1916) assigned topographic names to superficial features (figure 1.3) and estimated the albedo. In the early 20th Century, the observation of Mercury transit in front of the Sun allowed Albert Einstein (1879-1955) to confirm its Theory of General Relativity, which was able to predict the deviation of Mercury's motion (the precession of the perihelion) from the classical Newtonian theory in 1915. In 1965 Giuseppe Colombo (1920-1984) discovered the 3:2 resonance effect between the rotation and the orbital periods of Mercury (instead of the synchronous 1:1 previously suggested by Schiaparelli), which was confirmed in the next few years by radar measurements carried out from Arecibo radio-telescope. In addition, his studies on orbital mechanics brought to the realization of planetary flybys and the slingshot effect, which became a common practice in space missions until today.

In general, the apparent angular closeness between Mercury and the Sun has always made difficult the observation of the planet from Earth-based telescopes and, hence, it resulted as the less studied body in the Solar System. For this reason, in 1973 NASA launched Mariner 10 mission (figure 1.4), which performed three flybys (computed by Giuseppe Colombo a few years before) around Mercury between 1974 and 1975. Thanks to the data collected, the following discoveries were achieved: 1) the mapping of 45% of its surface at a resolution of about 1 km/px and a few images at about 100 m/pixel (*Murray*, 1975); 2) the measurement of the magnetic field (*Ness et al.*, 1974, 1975) that was really unexpected; 3) the measurement of ultraviolet signatures of H, He, and O in Mercury's atmosphere (*Broadfoot et*

Figure 1.3: *Lowell's map of Mercury, November 1896. From Lowell, 1897.*

al., 1974, 1976); 4) the documentation of the time-variable nature of Mercury's magnetosphere (*Ogilvie et al.*, 1974; *Simpson et al.*, 1974) and 5) the determination of some physical characteristics of Mercury's surface materials (*Chase et al.*, 1974). This revealed that the surface of Mercury was covered by dust and craters, quite similar to the Moon and to Schiaparelli's and Antoniadi's drawings. 30 years after Mariner 10, in 2004 NASA launched the second mission to Mercury called MESSENGER (MErcury Surface, Space ENvironment, GEochemistry and Ranging, *Solomon et al.*, 2007), which allowed to take a

Figure 1.4: *Illustration of NASA Mariner 10 spacecraft. Credit: NASA.*

giant leap in the knowledge of the planet. Between 2011 and 2015 MESSENGER acquired a huge amount of data and images, hence, revealing some intriguing properties of Mercury. The mission will be illustrated in greater detail in the next section.

Further information about the planet will be provided by the next mission, Bepi-Colombo, planned by the European Space Agency (ESA) in collaboration with JAXA (Japanese Aerospace eXploration Agency) that will be launched in October 2018. It includes two spacecrafts, the ESA Mercury Planetary Orbiter (MPO, *Benkhoff et al.*, 2010) and the JAXA Mercury Magnetospheric Orbiter (MMO, *Hayakawa et al.*, 2004), that will investigate different aspects of the planet thanks to the suite of instruments on-board the two modules. The MPO will carry remote sensing and radio science experiments to map the entire surface of the planet, to study the geological evolution of the body and its inner structure, while the MMO will carry field and particle science instrumentation, to study the magnetosphere and its relation with the surface, the exosphere and the interplanetary medium.

1.2.1 MESSENGER mission

MESSENGER spacecraft (*Solomon et al.*, 2007) was launched by NASA on August 3rd, 2004 and, after three flybys of the planet in 2008-2009, it entered a near-polar orbit around Mercury in March 2011. Its orbit was highly elliptical, with a periapsis of 200 km and apoapsis of 15193 km. The mission was carried on until the exhaustion of propellant

and eventually on April 30th, 2015 the probe crashed on the surface, probably creating a crater of several meters in diameter. The spacecraft carried the following seven different instruments (figure 1.5) chosen to fulfill the science objectives of the mission:

- **MDIS** (Mercury Dual Imaging System), wide-angle plus narrow-angle imagers that mapped landforms, tracked variations in surface spectra and gathered topographic measurements (*Hawkins et al.*, 2007);

- **GRNS** (Gamma Ray and Neutron Spectrometer), used to map the relative abundances of gamma rays and neutrons emitted from the planet (*Goldsten et al.*, 2007);

- **XRS** (X-Ray Spectrometer), detected emitted X-rays to measure the abundances of various elements in the material of Mercury's crust (*Schlemm et al.*, 2007);

- **MAG** (Magnetometer), mapped the Mercury's magnetic field and searched for regions of magnetized rocks in the crust (*Anderson et al.*, 2007);

- **MLA** (Mercury Laser Altimeter), determined the planet's topography (*Cavanaugh et al.*, 2007);

- **MASCS** (Mercury Atmospheric and Surface Composition Spectrometer), which measured the abundance of atmospheric gases around Mercury and detected minerals in its surface materials (*McClintock & Lankton*, 2007);

- **EPPS** (Energetic Particle and Plasma Spectrometer), which studied the energetic particles in the magnetosphere of Mercury (*Andrews et al.*, 2007).

In addition, there was also the Radio Science experiment, that used the Doppler effect to measure very slight changes in the spacecraft's velocity due to Mercury's mass distribution anomalies, including variations in the thickness of its crust (*Srinivasan et al.*, 2007). Among the above instruments, the images acquired by the MDIS instrument were crucial in the realization of the present thesis, while the maps obtained by the X-Ray Spectrometer were used to define the Mercury region chosen for this study.

1.2.2   MDIS instrument

The Mercury Dual Imaging System (MDIS, *Hawkins et al.*, 2007) included both a Wide-Angle Camera (WAC) and a Narrow-Angle Camera (NAC) developed to image and map the surface of Mercury (figure 1.6(a)). The Wide-Angle Camera (WAC) had a 10.5º×10.5º field of view and observed Mercury through 12 different filters across the wavelength range
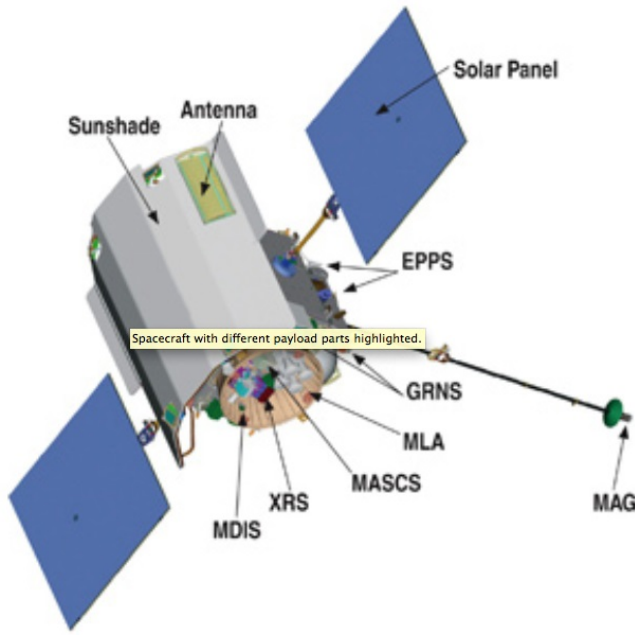
Figure 1.5: *Model of NASA Messenger spacecraft with the payload instruments. Credit: NASA.*

395 to 1040 nm. The Narrow-Angle Camera (NAC) had a 1.5º×1.5º field of view and took images of Mercury at high resolution in the single 700-800 nm band filter. The NAC and WAC cameras worked one at time, allowing them to share a common set of control electronics, and were cooled in order to mantain a suitable operating temperature especially at the hottest side of the orbit. The structure carrying the MDIS instrument was mounted on a transversal axis in such a way to have the possibility to pivot and reach any angle of view. During the three flybys in 2008 and 2009, the two cameras were used to obtain a near-global coverage (excluding the polar regions and two narrow longitudinal bands) at ~ 500 m/px and a multispectral mapping at ~ 2 km/px. After the orbit insertion of MESSENGER, the purpose of MDIS consisted in the acquisition of four mosaics: a nadir-looking global photomosaic at 750 nm at relatively low-incidence angles and < 250 m/px, a 25º-off-nadir to complement the previous one for stereo imaging, the completion of the multispectral coverage of the flyby phase, and high-resolution image strips crossing the main geomorphological features of the planet.

WAC and NAC images can be easily discerned by the image name. In fact, NAC images are denoted by 'EN' at the beginning and 'M' at the end of the name, while WAC images have 'EW' at the beginning and a letter from 'A' to 'L' at the end of the name, depending on the wavelength of the filter used by the WAC camera.

1.2.3 XRS instrument

The X-Ray Spectrometer (XRS, *Schlemm et al.*, 2007) measured the elemental composition in the top millimeter of Mercury's surface (figure 1.6(b)). It had a hexagonal 12º Field of

View, narrow enough to avoid the X-ray radiation coming from the star background but allowing a spatial resolution ranging from 42 km at periapsis to 3200 km at apoapsis, due to the high ellipticity of the spacecraft. The instrument was composed by three gas-filled proportional counter (GPC) detectors (Mercury X-Ray Unit, MXU) pointing towards the planet, a small Silicon solid-state detector (Solar Assembly for X-Rays, SAX) looking directly at the Sun and shielded by Beryllium foils, and the associated electronics (Main Electronics for X-Rays, MEX). The MXU detected the X-ray emissions (called X-Ray Fluorescence, XRF) coming from the surface after solar X-rays hit the surface, while the SAX tracked the X-ray radiation bombarding Mercury. The four detectors of XRS could discern the K_α lines for Magnesium, Aluminum, Silicon, Sulfur, Calcium, Titanium and Iron inside the energy range 1 to 10 keV, and in particular the three detectors of the MXU were used to maximize the area of the active detector and to resolve the abundances of the lighter elements on the surface of the planet. Characteristic XRF data could be retrieved during two different periods of solar activity: the K_α lines of Mg, Al and Si in the 'soft' X-rays at low energies (less than ~ 2 keV) could be distinguished during quiet-Sun periods, thanks to thin absorption filters mounted on two detectors of the MXU, while solar flares produced significant XRFs which allowed to estimate the concentrations of heavier elements (Fe, Ti, Ca and S).

(a) (b)
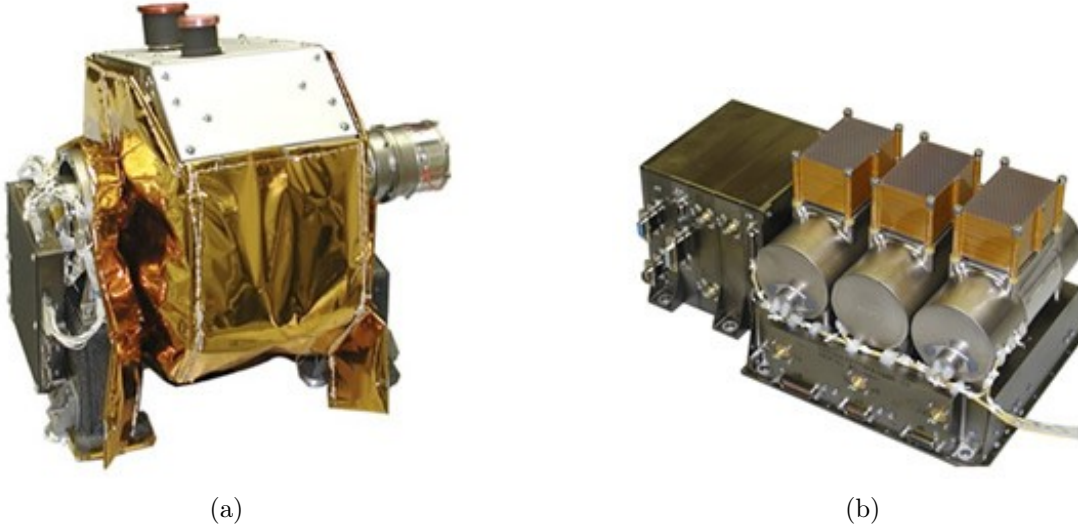
Figure 1.6: *(a) The Mercury Dual Imaging System. The WAC and NAC imagers are fixed on a Beryllium radiator on top of the instrument. Credit: NASA / JHU Applied Physics Lab / Carnegie Inst. (b) The X-Ray Spectrometer onboard MESSENGER payload. The three gas-filled proportional counters are visible. Credit: NASA / JHU Applied.*

Chapter 2

Peculiar features on the surface of Mercury: the hollows

Mercury's crust shows a variety of terrains (some examples in figure 2.3) with different reflectances and relative spectra (*Murray et al.*, 1974). During the first NASA MESSEN-GER flybys two types of spectral units were classified with a lower reflectance than the global average: the LBP (Low-reflectance Blue Plains) and the LRM (Low Reflectance Material). As illustrated by *Denevi et al.* (2009), the former has a reflectance $\sim 15\%$ lower than the global average, and this reflectance grows going from the visible to the near-infrared wavelengths with a slighter slope than the average of Mercury (consequently, the adjective 'Blue'). This kind of material can be found in the proximity of impact craters and basins and has probably been placed by impacts or volcanic processes. The latter has a reflectance $\sim 30\%$ lower than the global average and constitutes more or less 15% of the surface of the planet, under the forms of ejecta from impact craters, annular deposits around impact basins, stripes of dark material excavated by impacts and also non-impact structures with volcanic origin (*Denevi et al.*, 2009). LBP and LRM significantly differ from the HRP unit (High-reflectance Red Plains), which can be defined as plains with a higher reflectance than the global average and a steeper 'redder' spectral slope (figure 2.2) in the visible to near-infrared range (*Denevi et al.*, 2009). The LPB and LRM units are also different from the BCFD (Bright Crater Floor Deposits) unit, which are bright terrains within craters hosting hollows and with bright haloes (*Blewett et al.*, 2009), whose origin is still uncertain (*Thomas et al.*, 2016). In addition, between low- and high-reflectance materials there is the IT (Intermediate Terrain) unit, having a similar slope to the LRM but a higher reflectance than LRM (*Blewett et al.*, 2013). A particular type of the LRM consists in the so-called 'dark spots' (figure 2.1(a)): *Xiao et al.* (2013) described these features as the material with the lowest average reflectance detected on Mercury with
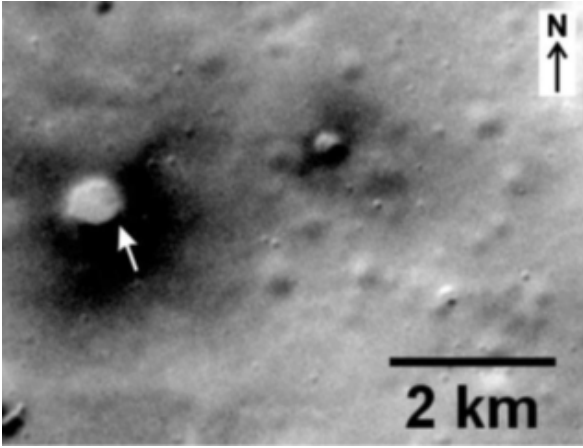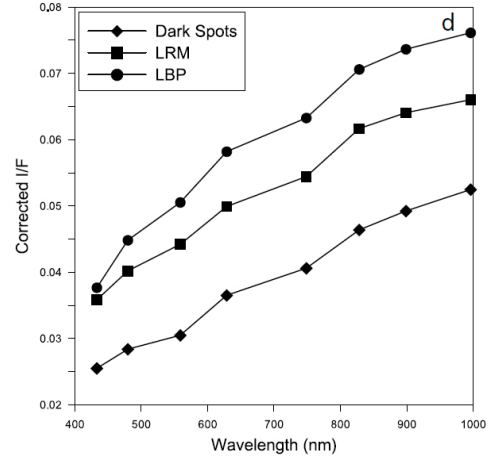
(a)   (b)

Figure 2.1: *(a) Image EN0234070626M is a particular of the northern hemisphere (60º N, 109º E) at a resolution of 18 m/px, showing examples of dark spots. An irregularly shaped, rimless depression is visible at the center of the dark spot (white arrow), having a higher reflectance than the surrounding dark spots. (b) The typical spectra of dark spots, LRM and LBP units are plotted. From Xiao et al., 2013.*

a spectral slope similar to the one of the LRM (figure 2.1(b)). Dark spots have diffuse margins and are found as isolated entities on several terrains and morphological settings on the planet, such as LBP, intercrater plains and impact craters, while no dark spots have been observed on HRP material. Other components of the surface of Mercury are the pyroclastic deposits and the impact melt flow. The pyroclastic deposits are materials emplaced by explosive volcanic eruptions, having a higher reflectance than the surroundings and a 'redder' spectral slope similar to the HRP (*Blewett et al.*, 2014). Conversely, impact melts are materials which have undergone fusion due to meteoric impact and have a low reflectance and a relatively flat spectral slope (*Klima et al.*, 2011).
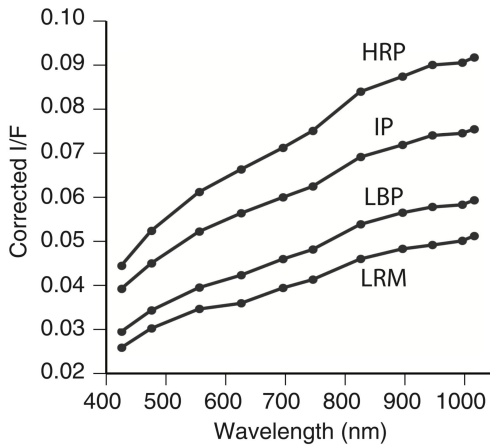
Figure 2.2: *The spectra characterizing the different spectral units identified on Mercury are reported. IP stands for Intermediate Plain, which is equivalent to the Intermediate Terrain. From Denevi et al., 2009.*
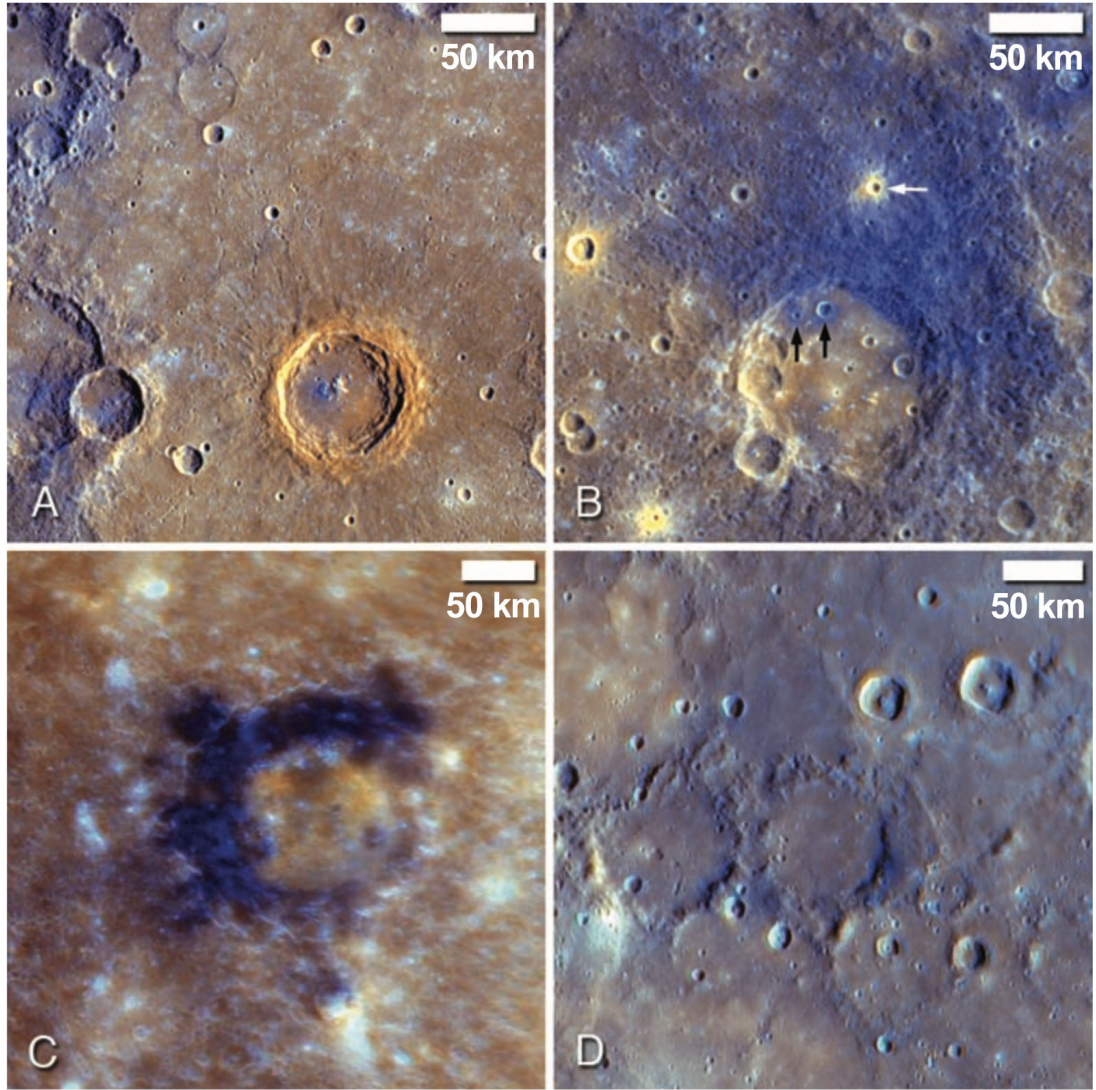
Figure 2.3: *Examples of different units of Mercury's surface. (A) The ejecta of the crater in the lower part of the image (centered at 4°S, -56°E) represents a HRP unit, while the HRP in the crater floor may have been buried in IP (Intermediate Plain). (B) Example of LRM exhumed from beneath smooth plains in crater Titian (4°S, -43°E); the white arrow indicates a small crater which re-exposed plains material, the black arrows point to LRM exposed from below younger smooth plains. (C) Asymmetrical distribution of LRM in unnamed crater (9°S, 20°E). (D) LBP units NW of Caloris basin (43°N, 121°E), not spectrally discernible from the older craters that they host. From Denevi et al., 2009.*

Among the different terrain units identified on the surface of Mercury, to date, the study of peculiar features, called "hollows", is one of the most interesting open fields of research concerning the geology and evolution of the surface of the planet. Hollows were first noted in Mariner 10 images as patches of high-reflectance material inside some craters (*Dzurisin*, 1977). Then, thanks to MESSENGER insertion in orbit, high-resolution MDIS NAC images revealed those patches as irregular small rimless depressions with flat

floors and steep walls, bright interiors and halos, and a bluish hue in multispectral images (*Blewett et al.*, 2011). They were named hollows in order to distinguish them from volcanic vents and pits, whose formation is due to withdrawal of underlying magma (*Gillis-Davis et al.*, 2009). Hollows can be found as single entities of tens of meters across or groups
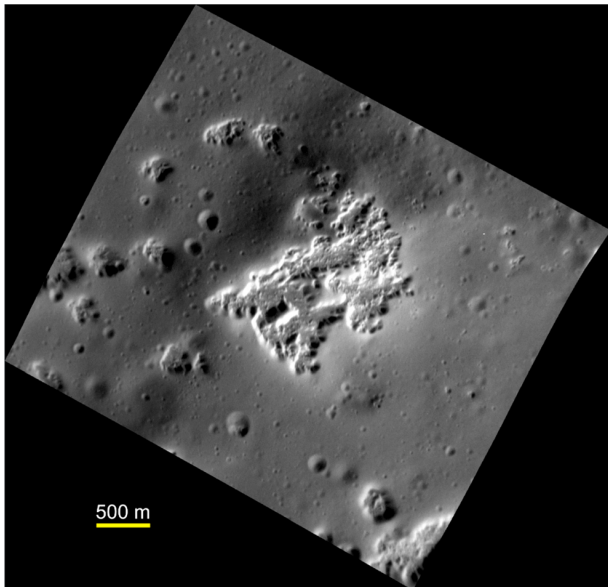
Figure 2.4: *Typical appearance of a cluster of hollows near the peak-ring of Scarlatti basin (39.9°N, -101.8°E). The image was taken by the Narrow-Angle Camera (3.8 m/pixel). From Blewett et al., 2016.*

up to tens of kilometers across (figure 2.4), while the measurements of internal shadows from high-resolution NAC images permitted to estimate their depths as few tens of meters (*Blewett et al.*, 2011). They usually occur in regions with a lower reflectance than the average of Mercury, whose most of this material is under the form of regional deposit (LRM and LBP), and in localized deposits and 'dark spots' with a lower reflectance than LRM (*Blewett et al.*, 2011, 2013; *Xiao et al.*, 2013; *Thomas et al.*, 2014). In the next section, we illustrate the main characteristics of hollows, including morphology, their association with different terrains of Mercury, in addition to their possible formation and evolution.

2.1 Hermean hollows properties

2.1.1 Geological locations and their terrains association

Although hollows were initially associated to the floors of impact craters (*Blewett et al.*, 2009), they have been detected in several different geological settings (figure 2.5) that can be summarized as crater floors, crater walls and rims, central peaks and peak rings and also outside craters. Hollows are often found in combinations of the first three settings within the same crater. In general, they fill impact craters in 84.5% of cases, which correspond to the 97.5% of the total extension of hollows (figure 2.6, *Thomas et al.*, 2014). Several
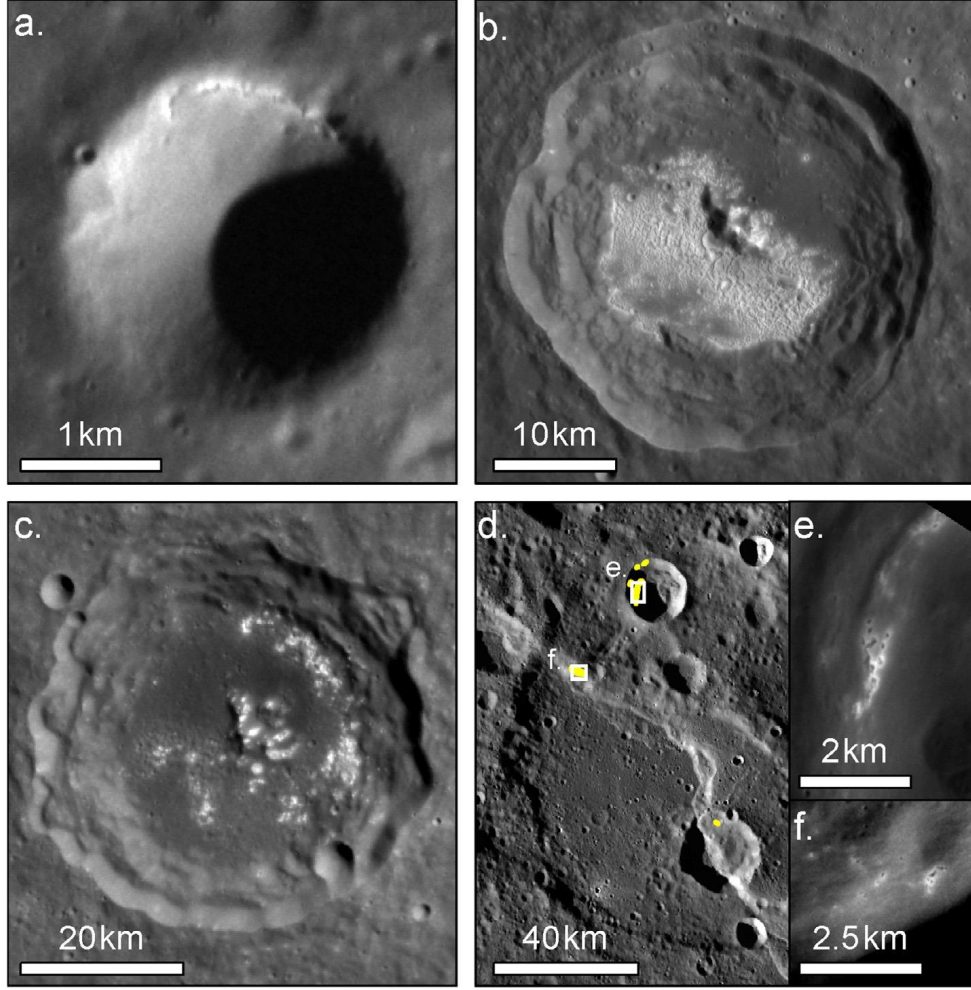
Figure 2.5: *Examples of the most frequent locations of hollows in association with craters. (a) At the inner rim of a small crater (57.4°N, -58.6°E, EN0238696485M); (b) on the floor and on the peak structure of Hopper crater (12.5°S, -55.8°E, EN0223616383M); (c) clustered in a band confining with the inner wall of Nampeyo crater (40.3°S, -49.9°E, EN0253678867M); (d) in a young impact within the degraded Duccio crater (58.2°N, -52.3°E, monochrome mosaic), outlined in yellow; (e) close-up of hollows in a younger impact crater (EN0223658124M); (f) close-up of hollows on a thrust (EN0223614937M). From Thomas et al., 2014.*

crater floors host rich clusters of hollows, which can be separated by distances up to 5 km or, in some cases, merged to form an 'etched terrain', a continuous hollowed area (*Blewett et al.*, 2011; *Thomas et al.*, 2014), or again formed at the base of crater peaks and walls and enlarged by scarp retreat (*Vaughan et al.*, 2012). Some groups of hollows with a smaller areal extension were found in older craters probably dated back to the Mansurian age, between 3.5 and 1 billion years ago, with topographical heights degraded by impact erosion (*Blewett et al.*, 2013). In addition, hollows have been observed in bands on the rims of craters, on terraces and on slightly sloped walls. It is spotted that their position probably depends on the crater side facing direct solar insolation (*Blewett et al.*, 2013). Central peaks and peak rings of complex craters host multitudes of hollows,

17
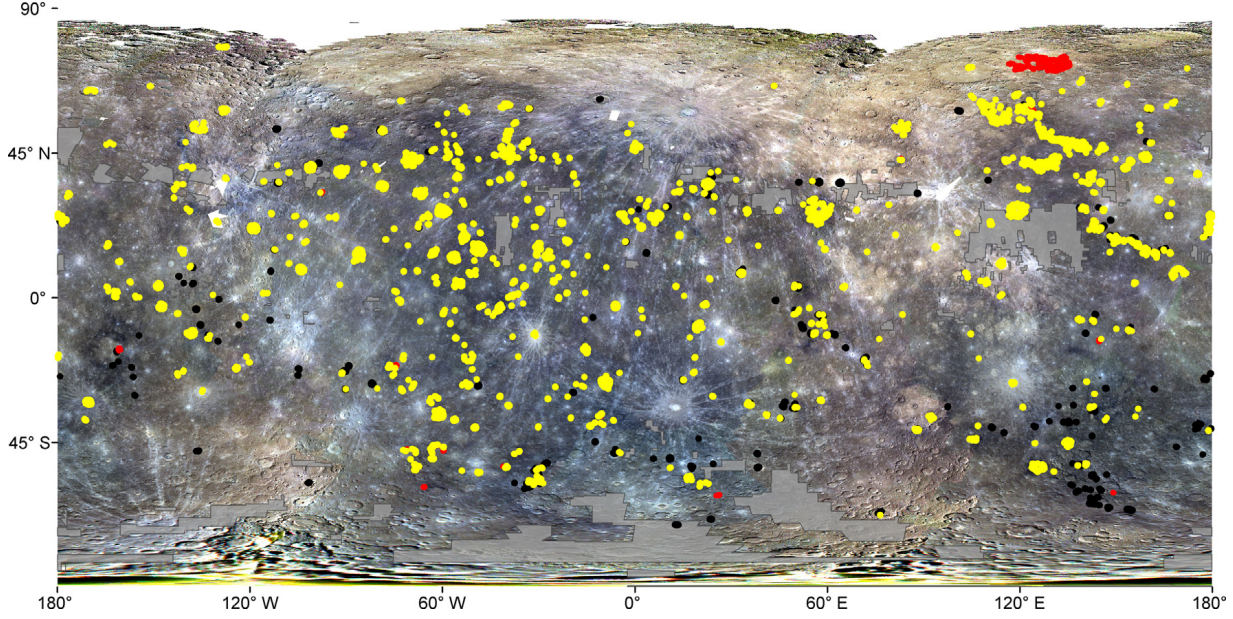
Figure 2.6: *Global occurrence of hollows, pits and spectrally red pitted ground. Yellow: hollows; black: pits; red: spectrally red pitted ground; grey: area not imaged at < 180 m/px. (Base mosaic: MESSENGER global colour v3). From Thomas et al., 2014.*

especially around the base of these inner structures (*Thomas et al.*, 2014). In some basins (such as the Caloris one), several small hollows groups were found on the rims and were associated with pyroclastic pits. When hollows were detected outside impact craters, they appeared as single entities or rare groups with a small areal extension if compared to the mean extension within craters. They occurred on flat portions of rough terrains or in linear patterns cross-cutting geological units (*Blewett et al.*, 2013). After Mariner 10 mission, the bright patches of hollows were supposed to be only on crater floors (BCFDs, *Dzurisin*, 1977), while more recent works allowed to establish a strong connection with LRM and LBP, including the dark spots (figure 2.7). Generally, the LRM was suggested to have formed deeply in the crust of the planet, and subsequently it was brought to the surface by impacts (*Denevi et al.*, 2009). According to *Vaughan et al.* (2012), LRM itself may be the factor causing hollow formation, as the phase that gives the LRM a low reflectance may give birth to hollows through self-removal or destruction. *Blewett et al.* (2013) showed the association between hollows and low-reflectance units was a common feature from the observation of the global map (in particular between -80°E and -60°E, where LRM is dominant). According to the same study, even hollows found in HRP have formed in the underlying LRM which was excavated by impacts. The 96% of the total hollowed area analyzed by *Thomas et al.* (2014) seemed to be associated with regional or localized LRM, while only $\sim 7\%$ with HRP and $\sim 8\%$ with LBP. Dark spots commonly host rimless depressions and hollows with bright haloes (but not all hollows on the planet
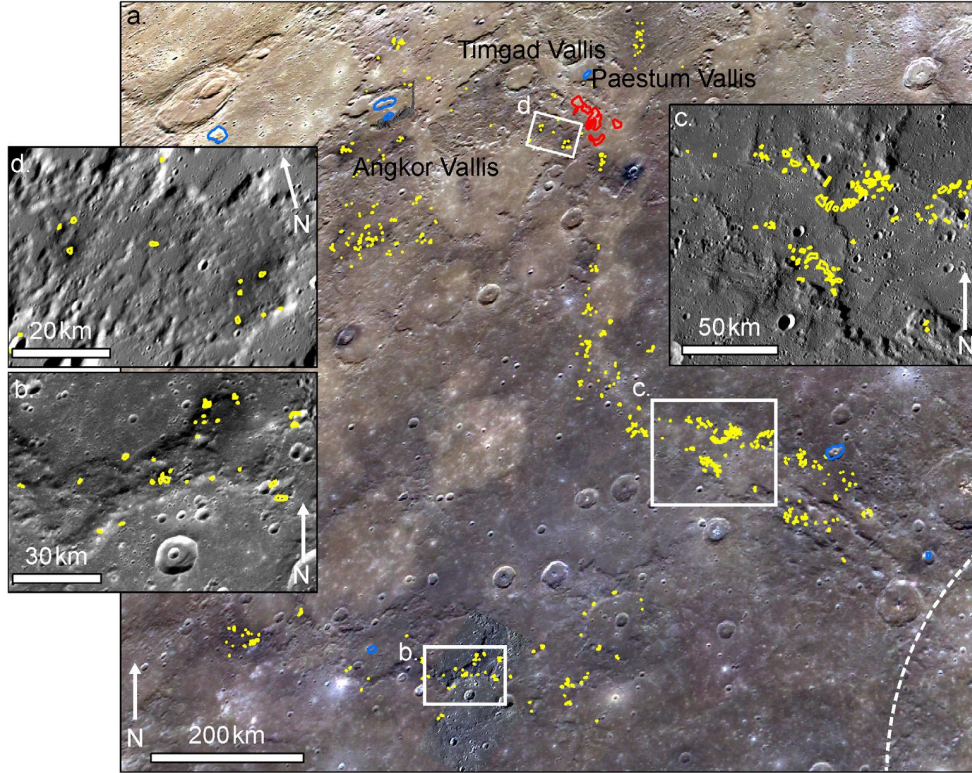
Figure 2.7: *(a) Association of some dispersed clusters of hollows (outlined in yellow) with different units at northwest of the Caloris basin. The region at NW hosts possible lava channels, several pits (outlined in blue) and areas of spectrally red pitted ground (outlined in red); (b) hollow formation in the southern region occurs on LRM forming degraded crater rims (EW0264188888G); (c) hollows in the mid-part of the northern grouping form in the proximity of a smooth, curvilinear unit of HRP; (d) hollows occur in dark spots on regions of the non-plains surface (mosaic of images EW0231135561G, EW0231135600G and EW0231135586G). From Thomas et al., 2014.*

are surrounded by dark spots). As shown by *Xiao et al.* (2013), less than 30% of hollows are characterized by dark spots, thus leading to two hypotheses: i) hollows may initially form with dark spots, whose thin deposits lose the low reflectance due to vertical crustal mixing, or ii) only some hollows may have formed with dark spots and others without, thus there is no age relationship between the two features. Hollows have been observed in some craters in proximity of pyroclastic deposits, of clearly volcanic origin (*Blewett et al.,* 2011): the analysis of these sites would suggest that, as they are host in the dark LRM material which partially covers those craters, the LRM substrate may be buried under a thin mantle of pyroclastic deposits (*Blewett et al.,* 2013). *Thomas et al.* (2014) found a strong association between hollows and non-impact-related pits within craters since most of these pits showed spectrally-red deposits, probably of pyroclastic nature. The contrary is not true, as only 22% of hollows groups were found within a radius of 50 km around a pit or a 'pitted spectrally area' and, in addition, almost all of these had bright red deposits, implying pyroclastic activity.

2.1.2 Morphological characteristics

The depth of these structures was calculated from NAC images at sufficiently high resolution through the measurement of the shadow length cast by the hollow edge, knowing the solar incidence angle (figure 2.8). *Blewett et al.* (2011) found a hollow mean depth of 44 m, while *Vaughan et al.* (2012) obtained an estimate of 30 m. *Thomas et al.* (2014) measured 108 shadows in 27 groups of hollows, and found an average depth of 47 ± 21 meters, with data ranging from 5 ± 0.75 m to 98 ± 19.5 m. Subsequently, the continuous addition of images in the last two years of MESSENGER operations allowed *Blewett et al.* (2016) to dispose of a bigger number of images at a suitably higher resolution. In that work 882 images were considered at an average resolution of 13.3 ± 4.9 m/px and 565 of them were used for a total of 2518 shadow measurements. These high-resolution images were uniformly distributed in longitude, while the distribution in latitude revealed a higher number of images at the middle latitudes in the northern hemisphere due to MESSENGER eccentric orbit. The images mean solar incidence angle was $67.3^{\circ} \pm 9.4^{\circ}$, while the mean value of the hollow depth estimate distribution was 24 ± 16 m, with a tail at greater depths. This value was smaller than the previous works mentioned above: this shows that higher resolution images allowed to measure the depths of smaller hollows which are assumed to be shallower than the larger ones. In addition, it was pointed out that the solar incidence angle (computed through azimuth and elevation of the Sun) has an important role: higher angles project longer shadows which can be resolved in lower quality images, while high resolution images are needed to resolve shadows by smaller incidence angles.
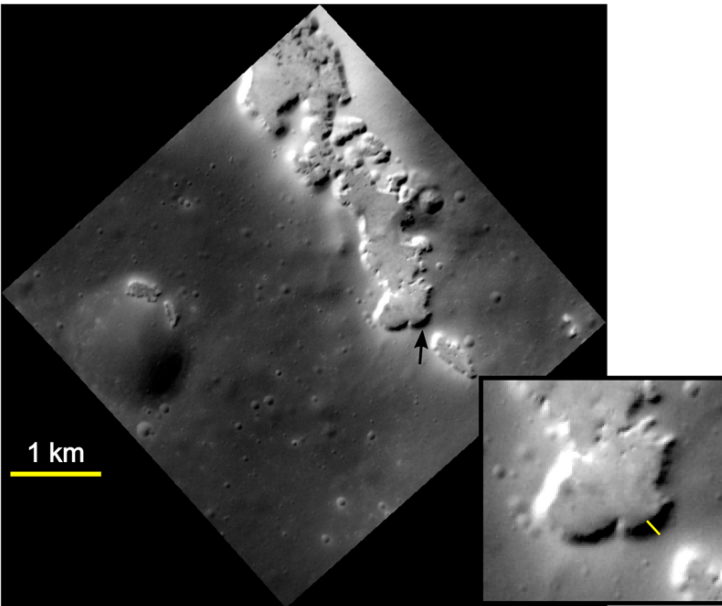
Figure 2.8: *Example of the measurement of the hollow depth from the projected shadow. The image (EN1058851700M) shows a cluster of hollows (43ºN 115.4ºE). The shadow (yellow segment in the lower right snippet) is 69.5 m, giving a depth of 55 m. From Blewett et al., 2016.*

The tendency of hollows to form on Sun-facing crater slopes and geographical strips was investigated in detail by some authors. *Blewett et al.* (2011) first noted that hollows on equator-facing walls would experience maximal solar heating, thus concluding that the development of hollows may be promoted by high temperatures. This assertion was initially confirmed by the observation of other hollows on slopes facing one of Mercury's 'hot poles' (*Blewett et al.*, 2013). Indeed, the elliptical orbit of Mercury causes a variation in insolation along the equator, going from the 'hot poles' (0°E and 180°E) which are under the Sun at perihelion, to the 'cold poles' (-90°E and 90°E) under the Sun at aphelion. In order to realize a more detailed statistics, *Thomas et al.* (2014) investigated the role of solar heating in the formation of hollows by measuring the variation of areal extent in longitude and latitude, and the slope aspect. They made use of all MDIS NAC images with resolutions < 180 m/px to study hollows closely, while WAC images in three different spectral filters with resolutions < 1000 m/px were analyzed to study the spectral features of the substrates. As a result, they found 445 groups of hollows (which were extended to 608 in *Thomas et al.*, 2016) with a mean extension of 129 km^2 and totally covering 57400 km^2. The groups were formed on the basis of the occurrence of hollows inside the same crater or in a location within 50 km from each other when they were outside craters. In general, thanks to the good image coverage, they could affirm that hollows are rare at high northern latitudes, while no similar constrain could be placed on the high southern latitudes, where the image resolution was quite low due to the eccentric orbit of MESSENGER. *Thomas et al.* (2014) measured the areal extent of hollows in 20° bins in longitude (in a 30°S to 30°N equatorial strip normalizing this area to the total area imaged at < 180 m/px). As expected by the solar insolation hypothesis, the fraction of hollowed area was minimum around the cold poles and reached a maximum at the 0°E hot pole, but a similar maximum around the other hot pole at 180°E was not observed (figure 2.9(a)). As the region in the equatorial strip between 150°E and 180°E is partially constituted by plains, the areal extent of hollows was normalized to the fraction of non-plains in each bin, in order to test if plains affected the occurrence of hollows. In this case, the occurrence of the second maximum at 180°E was observed, thus establishing a strong correlation between the extent of hollows (in non-plain regions) and the intensity of mean insolation, though it was not a sufficient condition. A strong peak in the areal extension was also observed between -60°E and -40°E, but it was interpreted as an anomaly and was not considered. The same procedure was applied for the latitudinal variation (figure 2.9(b)): the hollowed area was measured in 30° bins in latitude. There resulted to be a wide variation at different latitudes, mainly due to observational bias. Indeed, at northern latitudes higher than 60°N the solar incidence angle was too high to detect hollows inside
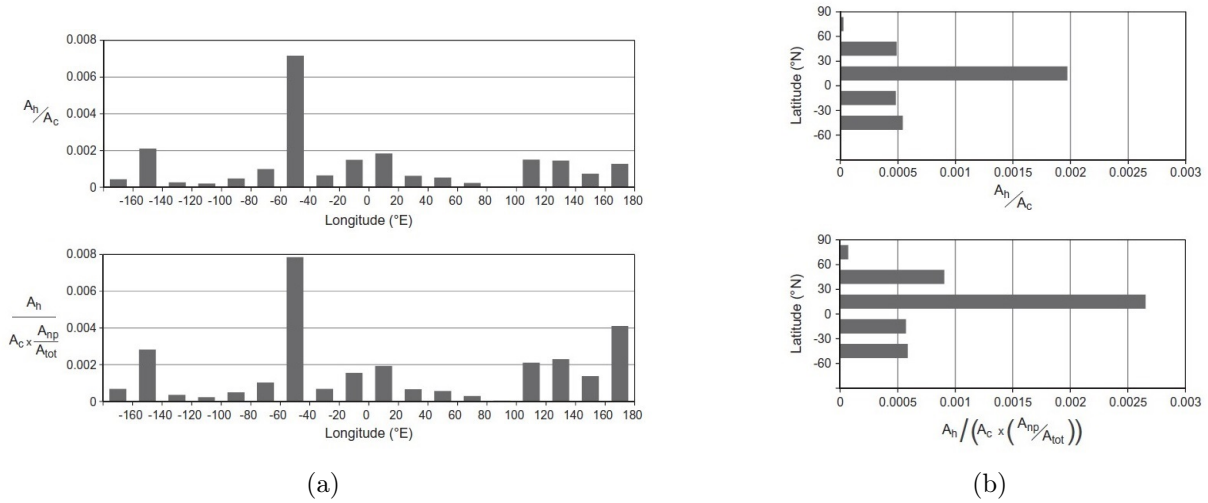
Figure 2.9: *(a) longitudinal variation in the areal extension of hollows (in 20° bins) in the 30°S to 30°N region. (b) the latitudinal variation (in 30° bins). The two top panels represent the hollowed area (A_h) normalized by the total area imaged at < 180 m/px (A_c). The bottom panels show the hollowed area normalized by the total non-plains area (A_{np}/A_{tot}) imaged at < 180 m/px. From Thomas et al., 2014.*

shadowed craters, while at higher southern latitudes than 60°S, as already mentioned, the resolution was too low to identify hollows. At middle latitudes, in both normalization cases (with respect to the total hollowed area and the total non-plain hollowed area) the northern hemisphere experienced a larger hollowed area than the southern hemisphere, thus suggesting that the former is favored or the latter is discouraged by some factor.

Thomas et al. (2014) also analyzed the relationship between the solar heating and the slope aspect (figure 2.10) previously studied by *Blewett et al.* (2011, 2013). *Thomas et al.* (2014) found a strong correlation in only 8% of the hollows groups considered, but this low fraction may be due to the fact that in many images of hollows at mid- or high latitudes only the Sun-facing slope was illuminated. In addition, in these cases the lighting conditions were not sufficiently suitable to promote hollow formation on the opposing slope, therefore a preferential hollow formation slope was not observed. Moreover, given that most hollows have been detected on different slopes within the same group or on flat surfaces, they concluded hollows do not commonly form on Sun-facing slopes.

2.1.3 Formation and evolution mechanisms

The absence of superimposed craters on hollows makes them morphologically fresh structures, probably implying their formation is still occurring. Actually, the exact process is not yet fully explained, but most authors converge to the hypothesis of the loss of volatiles as the generation of hollows. *Blewett et al.* (2013) supported the idea that hollows form in
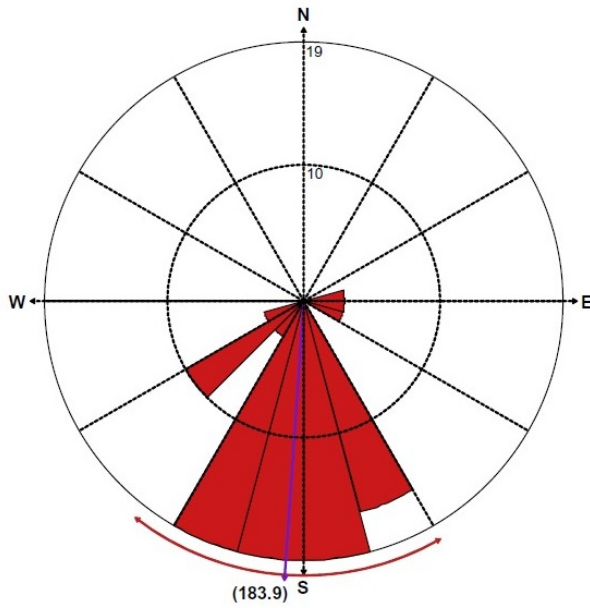
Figure 2.10: *Appearance of slopes on which hollows preferentially form within craters in the northern hemisphere. The purple arrow indicates the mean angle (with respect to North), the red arc is one standard deviation. It shows a correlation with the Sun-facing slopes. From Thomas et al., 2014.*

units which contain a phase that may become unstable when it is exposed to the surface: this phase can be destroyed by high temperatures or ion sputtering, and consequently the material is lost, leading to the formation and the enlarging of shallow depressions. The loss of volatiles forming the surface of Mercury is still under investigation, but two mechanisms were proposed. The former asserted that, due to the low rotation and the lack of an atmosphere, volcanic gases could condense on the night-side at low temperature and along fractures in the subsurface and then be buried by volcanic pyroclastic deposits. The volatile-rich deposits would be sequestered under a cap rock, brought to the surface and redistributed by impacts: volatiles would then sublime from craters and ejecta, thus forming depressions through collapse (figure 2.11(a)). Chlorine is a volatile element typical of volcanic gases that may be involved in this process, but it was not detected by GRNS (possibly due to low resolution). The second hypothesis concerned the contribution of high temperatures by intense solar heating and sputtering by energetic ions and microm-eteoroid, which could destroy the volatile-bearing phases (figure 2.11(b)). The volatiles taken into account in this hypothesis included different minerals such as Sulfur, whose mineral abundance as sulfide can play an important role in the formation of hollows, and Sodium and Potassium, which are provided to the exosphere through space weathering. The depth of hollows may be determined by the thickness of the volatile-bearing layer or a thermally insulating lag which prevents loss of volatiles. The duality of endogenic and exogenic processes was also shared by *Thomas et al.* (2014). In the previous hollows morphological analysis, we report that hollow formation and insolation intensity seemed to be correlated, though hollows have been observed on different crater slopes (*Thomas*
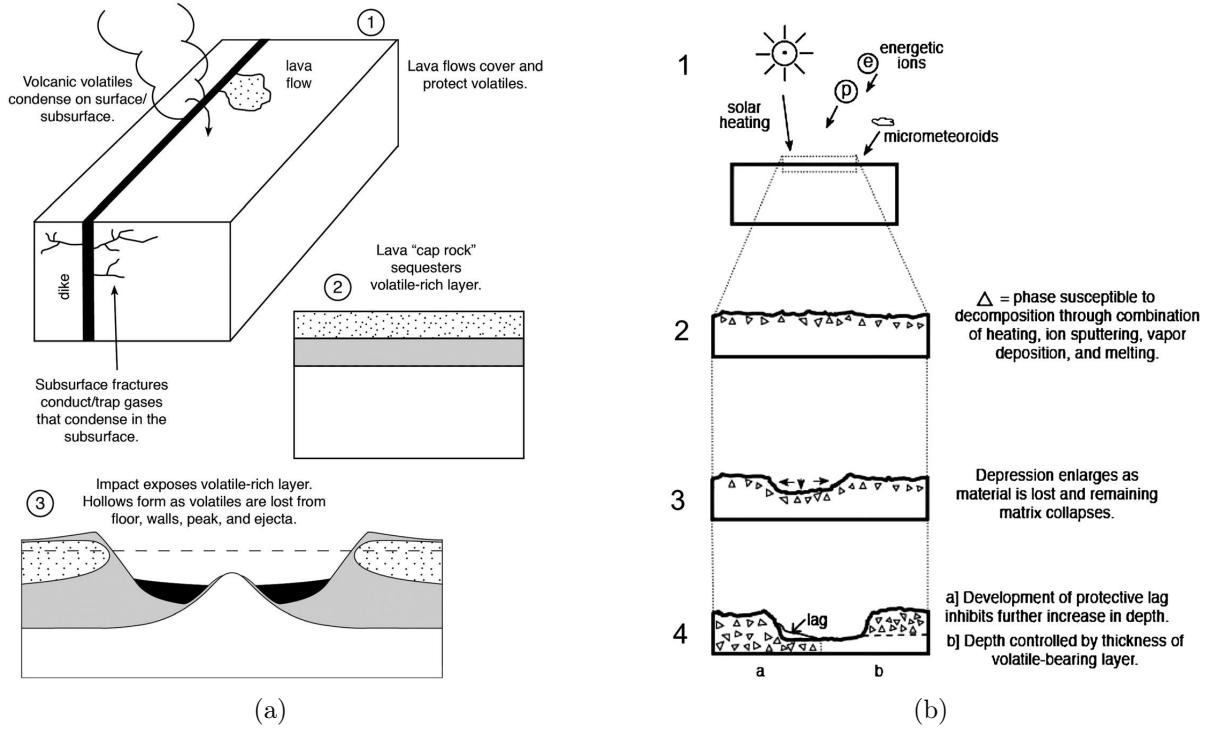
Figure 2.11: *(a) Illustration of hollow formation hypothesis as a consequence of sequestration of volatiles. (b) Theory of hollow formation through solar heating or space weathering. High temperatures, ion sputtering and micrometeoroid bombardment decompose volatile-bearing minerals, leading to hollow formation (1 to 3). When (4a) a protective armor of material builds up, or (4b) the volatile-bearing layer is consumed, the enlargement of the depression stops. From Blewett et al., 2013.*

et al., 2014). This would confirm not only the hypothesis of the sublimation of volatile components, but also the photon-stimulated desorption (PSD), by which atoms are excited by UV radiation and are desorbed and escape to the exosphere. This process is stronger at perihelion than at aphelion, hence, being consistent with the longitudinal variation of hollowed surface. However, as it operates only on the topmost layer of atoms, it requires a very efficient mechanism of volatile-transfer, hence, it is not expected to play an important role in generating hollows, but rather enhancing it. Another exogenic process considered also by *Thomas et al.* (2014) was the ion sputtering by solar wind, which was assumed to be stronger at higher latitudes, where magnetic field lines are open. However, due to the difficulty in detecting hollows at high latitudes, it was not possible to verify this statement. In *Thomas et al.* (2014) work two endogenic processes were also examined: the former, already investigated by *Blewett et al.* (2013), concerned the ascending of the volatile component to the surface and subsequent sublimation, while the latter included the ascension of volatiles as gases and the collapse of surface material. From the observation of hollows near volcanic pits, they concluded that the first hypothesis is more likely to

control hollow-forming than insolation, while the collapse hypothesis may be more suitable explanation for the shallow areas of pitted ground having spectrally red deposits. Another topic discussed by *Thomas et al.* (2014) regarded how the volatiles were brought to the surface. As most hollows are found within craters and their proximal ejecta, *Blewett et al.* (2011) had already suggested that hollows form in material excavated and exposed by impacts. In particular, hollows occur in the LRM on peak rings, which are the section coming from the greatest depth within the planet. Moreover, if there is a correlation between the crater age and the extent of hollows, older craters should host a larger extent of hollows. However, the original extent may have been partially buried by ejecta, and the hollow formation would stop if the required material is limited. Hollows have also been observed in very old craters, which required a supply of hollow-forming material long after the impact: this provision may have been renewed through smaller craters inside the parent crater. The generation of hollows in dark spots was discussed by *Xiao et al.* (2013), according to whom these dark spots may form during outgassing simultaneously to hollow formation, which probably occurred through deposition of dark material made of volatiles, followed by its sublimation. *Thomas et al.* (2016) investigated the spectral reflectance behavior of several geological features and found that the spectral slope of BCFDs and hollow floors is controlled mainly by maturity and composition, besides grain size. Indeed, the two units have a higher reflectance than the 'potentially-hollowable' surrounding terrains. Maturity was a central point in this argumentation: the intense solar particle flux and the micrometeoroid bombardment make any exposed surface on Mercury darker and redder, meaning that fresher units (most hollow floors) should have higher reflectance and flatter spectrum than older units. Therefore, *Thomas et al.* (2016) assumed that, if the spectrum of hollow floors is determined by 'immaturity' alone, it would not be sufficient to identify the volatiles that escaped at hollow formation. Nevertheless, this assumption was not consistent with their results, in particular the difference between the spectral slopes of hollow floors and BCFDs, the spectral slope at UV wavelength of 'immature' parent material, and the specific crustal morphology. Further explanation for a possible formation mechanism of hollows was presented by *Blewett et al.* (2016) involving graphite, which is the only mineral that would float on the melt mantle composition. This ocean of magma and graphite would have mixed with volcanic and impact materials and contributed to the LRM low reflectance (*Peplowski et al.*, 2016). According to *Blewett et al.* (2016), solar ion bombardment ($4H^+$) could bind to the C atoms of graphite, thus obtaining a gas of methane (CH_4): this reaction is quite efficient at room temperature and produces a species that is easily desorbed, favoring the formation of hollows through collapse. Therefore, the high reflectance of hollows may be due to the removal of the

25

darkening agent.

The formation rate of hollows was also investigated giving a first estimate within Raditladi basin (*Blewett et al.*, 2011), indeed, considering the age of the basin as 1 Gyr (*Strom et al.*, 2008), if hollows started forming just after the basin, they computed a growth rate of 1 cm per 70'000 years. In addition, *Blewett et al.* (2016) analyzed hollows in Balanchine crater, which was dated back to 300 Myr, thus finding an average enlarging rate of 1 cm per 10'000 years. These estimates must be assumed as lower limits due to the following factors: i) it is not possible to determine if hollows started forming just after the basin, ii) the growth rate may have not been constant during time, and iii) hollows may have grown radially from the center instead of the opposite tendency. In addition, since the LRM and LBP surfaces are not all covered with hollows, they suggested that the triggering mechanism would be the reaching of the right combination of physical conditions that may consist in some threshold concentration of volatiles or temperatures.

Finally, in a recent work, it was suggested that hollows are not only related to remnant material coming from a process that involves devolatilization. Indeed, performing geomorphological and compositional analysis on three different craters hosting hollows, it was suggested that sulfides alone cannot explain the hollows visible spectra. Hence, other minerals have to be taken into consideration as candidates for explaining the spectral properties of hollows, such as pyroxenes presenting transitional elements, like Cr, Ti and Ni. This means that hollows terrains are the expression of both the remnant material coming from a process that involve degassing and the bedrock-forming material in which they formed (*Lucchetti et al.*, 2018).

Chapter 3

Composition of Mercury from XRS measurements

As all the terrestrial planets in the Solar System, Mercury has a chemical composition reflecting the materials which constituted the proto-planetary disk approximately 4.5 billion years ago. While the internal composition of the planet can be theorized from indirect geophysical analyses, the elemental abundances of the superficial layer can be directly measured thanks to the advanced instruments of MESSENGER: it is then possible to study the processes which modified the surface, such as volcanism and impacts, excavating and exhuming the underlying materials. One of the major components of Mercury interior is assumed to be Iron for several reasons such as the high uncompressed density (5.4 g/cm^3) which is greater than for other planets, requiring heavy species. In addition, Iron was quite abundant in the early planetary nebula and, together with Nickel, led to the formation of the cores of terrestrial planets. Consequently, we would expect a high Fe/Si ratio: however, spectral lines associated to ferrous molecules as Iron Oxide (FeO) in the superficial silicates have been detected in the near infrared in smaller quantities with respect to the Moon or asteroids. Furthermore, several models were proposed to explain the anomalous high density such as the ones including high temperatures that would have depleted all volatiles, or the ones considering volatile-rich model compositions (*Morgan & Anders*, 1980).

Mercury's core, which has probably a larger mass fraction than that of the other terrestrial planets (*Siegfried & Solomon*, 1974), is thought to be partially molten (*Smith et al.*, 2012), a condition which also needs the presence of other elements lighter than Fe and Ni in order to stay liquid at the current low temperatures. Computer simulations resulted in a large number of combinations and concentrations of these light elements as the following: i) Carbon, which was probably abundant at the time of the core formation

(maybe as graphite, *Vander Kaaden & McCubbin*, 2015) but disadvantaged by highly reducing conditions; ii) Oxygen, which is an important constituent of the Solar System and present in silicate minerals, but could not melt in the forming metal core due to the insufficiently high temperatures; iii) Silicon, which is a major element in terrestrial planets and alloys strongly with Iron under reducing conditions (the latter confirmed by the high abundance of Sulfur on the surface) as reported in *Hauck et al.* (2013).

The composition of the mantle could be investigated through the analysis of volcanic material coming to the surface from beneath the crust. It follows that it should be rich in Sulfur and alkaline elements and poor in Iron and FeO. As illustrated by *Namur et al.* (2016), two types of lava occur on Mercury, depending on the depth at which it melts: one is associated to older volcanic high-Mg deposits found in the intercrater plains and heavily cratered terrains (IcP-HCT), whose melting may begin at the lower base of the mantle (400 km in depth), the other one is related to the low-Mg northern smooth plains (NSP) and may start melting at 200 km (halfway between the lower base of the mantle and the surface). Generally, the mantle is assumed to be likely a mixture of silicates (SiO_2) and Oxygen compounds, such as TiO_2, Al_2O_3, FeO, MgO, CaO, Na_2O and K_2O.

The turning point for the research on the Hermean composition (especially for the surface) was the beginning of NASA MESSENGER mission. During its five years of operations, MESSENGER allowed to determine the composition of the top $< 100 \ \mu m$ layer of Mercury's crust thanks to the X-Ray Spectrometer (XRS, *Schlemm et al.*, 2007). The first studies of the datasets obtained from XRS showed a wide variety of volatiles, thus refuting the depletion model mentioned above. Craters at polar latitudes, which are mostly in shadow, host Hydrogen and highly-volatile species, while other common volatiles have been found on all the surface. In particular, XRS showed that the surface was: i) rich in Magnesium and Sulfur, ii) poor in Aluminum, Calcium and Iron than the typical materials found on the Earth and the Moon (*Nittler et al.*, 2011; *Evans et al.*, 2012) and iii) highly abundant of volatile elements like Potassium and Sodium (*Peplowski et al.*, 2011, 2012, 2014). The results retrieved by *Weider et al.* (2015), which were used in this thesis, consisted in the generation of Elemental Ratio Maps. These maps express the abundances of elements in the form of ratios computed with respect to Silicon. This expression is preferable for two reasons: rationing reduces some uncertainties on data, and Silicon is more uniform than other elements (it varies only 15% across the surface) becoming a quite reliable comparison term. For each of Mg/Si and Al/Si ratios two different maps were generated, one for the quiet-Sun data and one for solar flare periods. More precise measurements were expected from the solar flare data for the two following reasons: i) solar flares produce spectra with higher signal-to-noise ratios, and ii) Mg/Si and Al/Si ratios

are less sensitive to uncertainties in estimating the solar temperature at flare temperatures than for the quiet-Sun period. In addition, the two maps resulted to be different due to systematic uncertainties affecting the quiet-Sun map that was scaled by empirically derived factors and combined with the flare map, in order to create the elemental ratio maps. The data coverage of final maps is dependent on the element atomic number. As already mentioned in section 1.2.3, heavier elements such as Sulfur, Calcium and Iron could be detected by XRS only during solar flares, while lighter elements such as Magnesium and Aluminum could also be identified during quiet-Sun periods. For these reasons, S/Si, Ca/Si and Fe/Si maps cover only partially the planet, while the Mg/Si and Al/Si maps have an almost global coverage. Several interesting results were reported in *Weider et al.*
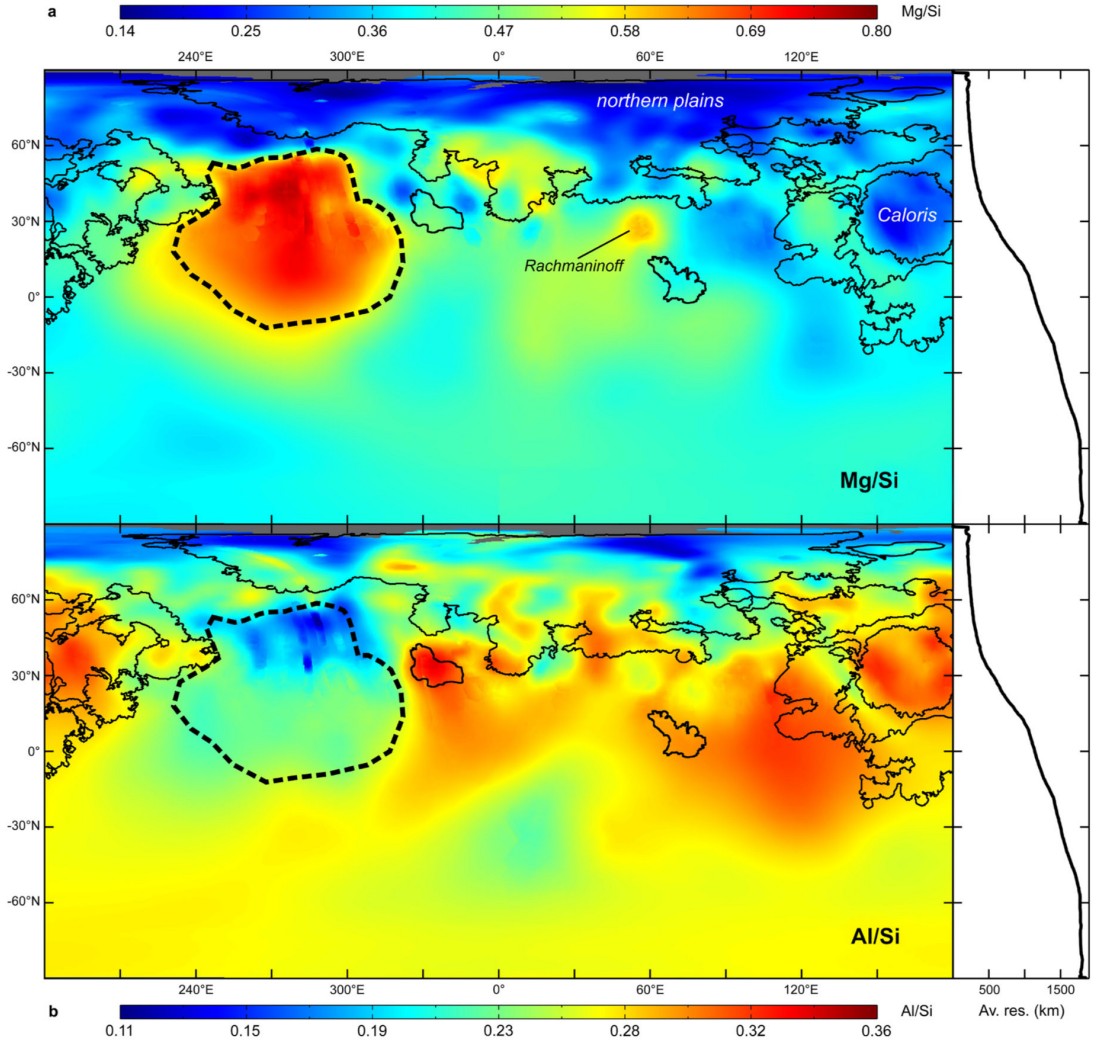
Figure 3.1: *Element ratio maps of (a) Mg/Si and (b) Al/Si obtained from XRS measurements. The solid lines indicate deposits of smooth plains in the northern hemisphere, including those associated with the Caloris and Rachmaninoff basins. The High-Magnesium Region is delimited by the dashed line. The plots on the right represent the average spatial resolution versus latitude. From Weider et al., 2015.*
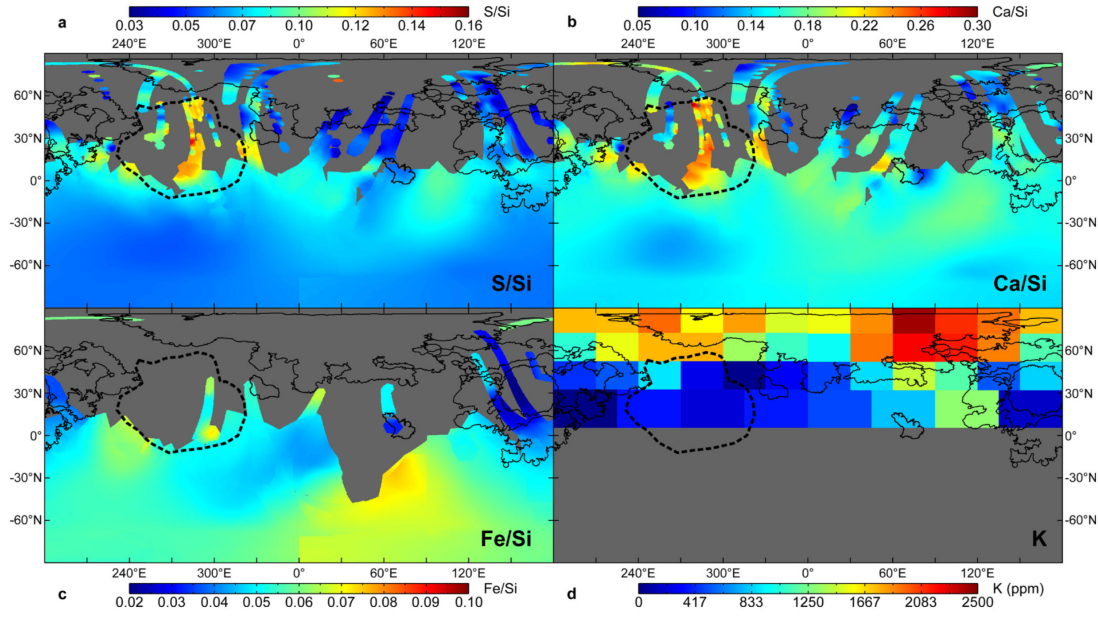
Figure 3.2: *The element ratio maps of (a) S/Si, (b) Ca/Si and (c) Fe/Si have been retrieved from XRS instrument, while (d) the abundance of Potassium was obtained from the Gamma-Ray and Neutron Spectrometer. The dashed and solid lines are the same as in figure 3.1. From Weider et al., 2015.*

(2014, 2015) for each element ratio map. The Mg/Si ratio of Mercury's surface ranges from ~ 0.14, observed in the volcanic smooth plains, such as parts of the northern plains and the Caloris basin, to ~ 0.80, localized in a well delimited region known as the High-Magnesium Region (HMR, see next section). The Al/Si map has a higher variability on smaller spatial scale than the Mg/Si ratio, and a much lower maximum value (~ 0.36) localized in a smooth plain east of the HMR and south of the northern plains (figure 3.1). The southern hemisphere reflected a low abundance in S/Si, Ca/Si and Fe/Si, while nothing could be stated for these elements in the HMR and the northern plains, because the related coverage by XRS was almost null (figure 3.2).

The absolute abundance of Potassium (K-map) was also measured in parts per million by the Gamma Ray and Neutron Spectrometer (*Goldsten et al.*, 2007). The resolution of the K-map (figure 3.2(d)) was much lower than those related to the other elements, hence, the XRS Mg/Si map was re-binned in such a way to match the resolution of the K-map, showing an inverse correlation between the two distributions. In addition, the distribution of Potassium and the limits of the northern plains do not perfectly overlap: to explain this mismatch, *Peplowski et al.* (2012) suggested a thermal redistribution scenario, according to which Potassium is transferred from hotter regions to parts of the planet experiencing lower temperatures. Conversely, this process cannot be applied to Magnesium as it is a non-volatile major element, and this is confirmed by the anticorrelation between the Mg/Si

and the K-map (*Weider et al.*, 2015).

3.1 The High-Magnesium Region

In order to find relationships between the distribution of hollows and the hosting terrain, we focused on a large region resulting to be rich in Magnesium (measured with respect to Silicon, Mg/Si). From the XRS spectrographic map of the surface obtained in *Weider et al.* (2015), the High-Magnesium Region (figure 3.3) is located approximately between 20ºS and 55ºN (∼ 3200 km) in latitude and between -130ºE and -40ºE (∼ 3800 km) in longitude, covering part of H2 (Victoria), H3 (Shakespeare), H6 (Kuiper) and H7 (Beethoven) quadrangles.

The boundaries of the HMR were not an easy task to compute: as several measurements were taken by XRS at different altitudes and resolutions, the map generation process produced an HMR with blurred borders and an average resolution decreasing from North to South (*Frank et al.*, 2017). However, the HMR has been identified as a distinct geochemical terrain by GRNS: it is a region of high thermal neutron absorption implying a high average atomic mass of the elements in the regolith (*Peplowski et al.*, 2015). *Weider et al.* (2015)
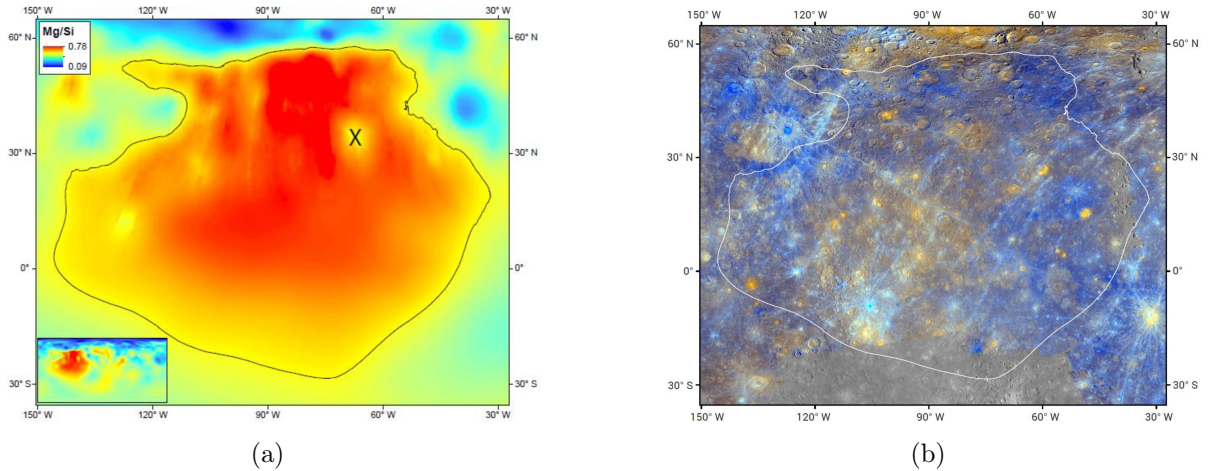
Figure 3.3: *The High-Magnesium Region outlined in: (a) the Mg/Si ratio map obtained from XRS, with an average relative statistical uncertainty for individual pixel of 7% (the X is an anomaly that roughly corresponds with a topographic plateau); (b) the high-resolution enhanced color map, superimposed on the Mercury monochrome basemap. From Frank et al., 2017.*

did not find a correlation between the HMR and its superficial reflectance discussing the fact that the origin of this region may be attributable to an ancient large impact which penetrated into a differentiated mantle. This means that the composition of the HMR would imply a high-degree partial melting of the mantle source. The region is characterized by low elevations, in addition to a thinner crust than the average value.

These characteristics are consistent with its interpretation as an old, heavily degraded impact basin. It does not show a morphological evidence for such explanation, but it hosts very few large basins, compared with other parts of Mercury of similar age. Mercury itself lacks basins above 500 km in diameter, unlike the Moon: this difference can be due to the basin formation process on the two bodies such as larger relaxation of topography after basin formation on Mercury, or a higher rate of volcanism which can subdue and erase basins. These factors may have been significant if Mercury's mantle had a higher average temperature than the lunar mantle at the time of the Late Heavy Bombardment. As a consequence, early impact basins experienced a stronger viscous relaxation and lithospheric deformation, making these structures actually difficult to recognize (the HMR may be one of these suggested basin-like topographies).

More recent studies, by comparing numerical simulations with MESSENGER data, suggested that the processes needed to erase the basin-like topography discussed above should also have erased the strong typical chemical signature of the region (*Frank et al.*, 2017). Therefore, they concluded that the HMR region is more probably due to an effect of high-temperature volcanism. Indeed, the ejecta of a hypothetical impact would have reached the antipode of the HMR, corresponding to an LRM region which has been excavated from beneath volcanic material. Even if this LRM could be considered as the result of a superficial crustal source in ancient terrain, there is no evidence of an antipode deposit of ejecta due to an impact in the HMR. Another characteristic of a possible impact at the origin of the HMR would be the presence of a topographical ring system, though it is not very common on Mercury (*Fassett et al.*, 2011). Actually, no interior rings were seen in the HMR but, considering the northern boundary dividing the HMR and the northern plains as the remnant of a basin rim, the ring structure may have been erased through volcanic resurfacing (*Head et al.*, 2011), later impacts (*Fassett et al.*, 2011) and global contraction (*Byrne et al.*, 2014). As a result of these argumentation, *Frank et al.* (2017) could not exclude the impact hypothesis, but the heterogeneous mantle and the volcanic activity of Mercury have been considered as the main factors for the origin of the HMR.

Chapter 4

Statistical analysis of hollows

In this work we analyzed hollows located in the High-Magnesium Region identified on Mercury to assess if there exists any correlation between these peculiar structures and this geochemical terrain of the planet. To investigate the hollows population of the HMR, we referred to the datasets available in literature. In particular, we considered the databases reported in *Thomas et al.* (2016) and *Blewett et al.* (2016). The first one is a list of 608 groups of hollows found on all over the planet, each one accompanied by its central latitude and longitude, in addition to the measurement of the total areal extension (*Thomas et al.*, 2016). This dataset also includes 445 groups already catalogued in *Thomas et al.* (2014) and was performed thanks to MDIS WAC and NAC images acquired during the MESSENGER mission around Mercury. As mentioned in section 2.1.2, *Thomas et al.* (2014, 2016) defined a hollows 'group' as a set of all the hollows occurring within a particular impact crater or basin, or within 50 km from each other in case they were observed outside craters. This global dataset includes all hollows sites found and identified on the surface of Mercury, even if there could be an observational bias due to the MESSENGER orbit. The second dataset refers to a well-defined group of hollows since in this dataset only NAC high-resolution images were used in order to characterize in greater detail hollows structures. This dataset consists in a list of 882 high-resolution NAC images (resolution < 20 m/px) containing hollows. For each image, it has been indicated the latitude, the longitude, the image resolution and if the depth derived by shadow length measurements was computed or not (*Blewett et al.*, 2016). In addition, another table reported the hollows depth measurements with associated latitude, longitude and the referred NAC high-resolution image used for the measure. Due to the high eccentricity of MESSENGER, which brought the probe closer to the planet at northern latitudes, the NAC images listed in the tables of *Blewett et al.* (2016) are located only in the northern hemisphere, where a much higher resolution was achieved. This means that not all hollows located on the

surface of the planet were observed at high resolution and, hence, only for a small group of these features we can derive additional information as the depth measurement.

As stated before, among these features, we focused our study on hollows located in the High-Magnesium Region. To isolate the features corresponding to this area, we first determined the limits of the High-Magnesium Region. Thanks to the element ratio maps by *Weider et al.* (2015), the area of the High-Magnesium Region could be delimited. This operation was made quite rough by the fact that the borders of the HMR were not sharp and well defined, but rather faded (as discussed in section 3.1). As a result, we considered a rectangular map portion between -120ºE and -40ºE, 10ºS and 57ºN. The hollows group list reported by *Thomas et al.* (2016) was restricted only to those located in that region, and, after the removal of groups occurring inside the rectangular portion but outside the HMR (due to its irregular shape), we finally obtained a list of 85 hollows groups that we used for our analysis. To better describe these 85 hollows groups, we downloaded all WAC and NAC images from the online resource PILOT[1], developed by NASA USGS Astrogeology Science Center. We selected WAC images with resolution up to 300-400 m/px, in order to provide the geological context in which hollows are located. This was useful for the first part of the analysis to identify the terrain associated to each hollows group found. Then, we selected NAC images with resolution up to 50-60 m/px to analyze hollows in greater detail providing quantitative measurements of their properties. The subsequent step consisted in discerning the groups within impact craters and those not associated to craters. To do this, we examined carefully all the WAC images downloaded, also with the support of the online NASA MESSENGER Quickmap[2] developed by the Applied Coherent Technology Corporation, an interactive map of Mercury composed by global and regional mosaics, which provides several useful tools. As mentioned in chapter 2, hollows are characterized by high reflectance (*Blewett et al.*, 2013) and, additionally, the crater slopes on which these features occur have a critical importance as they appear more or less bright depending on the lighting condition, (i.e. the angle of solar insolation). Consequently, as the MESSENGER Quickmap offers the map of Mercury under different lighting conditions, we were able to spot the bright patches of hollows in all the 85 sites by making a cross-check between the Quickmap maps and the WAC images available.

We also analyzed the WAC images to verify the possible presence of peculiar features different from hollows in the geomorphological settings. Actually, as a consequence of the association with different units discussed in section 2.1.1, we can state the presence of LRM as a very common characteristic (96% of the total hollowed area examined in

---

[1]https://pilot.wr.usgs.gov/
[2]https://messenger.quickmap.io

Thomas et al., 2014), while HRP and LBP are quite rarer (7% and 8%, respectively).

In addition, we expected to find hollows in association with features of volcanic origin such as pyroclastic deposits covering the LRM substrate (*Blewett et al.*, 2013) or pits, resulting from the collapse of underground chambers previously hosting magmatic material. These are recognizable from their 'redder' reflectance spectrum (*Thomas et al.*, 2014) and their yellowish hue, which highlights the bright bluish appearance of hollows. We analyzed the 3-color high-resolution Quickmap map of the northern hemisphere, thus noting clusters of hollows within Praxiteles, Scarlatti and Lermontov craters. As already reported in *Blewett et al.* (2011), these three craters are partially covered by a sheet of pyroclastic material (Praxiteles in the eastern portion, Scarlatti in the northern part). In addition, they host hollows in the proximity of small scattered pits on the floor of Lermontov and on the rims of volcanic vents skirting the peak-rings in the eastern part of Praxiteles and in the northern part of Scarlatti. We searched for further evidences of hollows associated with volcanic material. Crater Chaikowskij (figure 4.1(a)) hosts hollows within a worm-shaped structure with pyroclastic material, likely an old lava channel. Crater Mistral and unnamed crater (figure 4.1(b), lat. 5.382°N, long. -55.807°E) are characterized by expanses of pyroclastic material filled with hollows clusters. Finally, we found hollows on the rims of large volcanic pits of irregular shape in the center of craters Gibran (figure 4.1(c)) and Glinka (figure 4.1(d), showing the typical color of pyroclastic material). All these cases are clear proofs in favor of the existence of a direct relation between the dynamics of volcanism (and the composition of pyroclasts), and the formation of hollows on Mercury. Indeed, the 'volcanic-sequestration hypothesis' proposed by *Blewett et al.* (2013) and illustrated in section 2.1.3 seems to explain well the presence of hollows in volcanic sites, considering the volatiles that are mainly involved in the sequestration beneath cap rock and the depletion (Chlorine and Sulfur, for instance). This is supported by the observation that 77% of pits within craters have nearby hollows on all the surface of Mercury (*Thomas et al.*, 2014). In addition, this evidence defends the theory reported in *Thomas et al.* (2014), according to which the areal extension of hollows near pyroclastic pits is on average higher than elsewhere, thus suggesting that hollow formation is greater in proximity of these volcanic features.

Therefore, we list in Appendix A the 85 hollows groups identified associating the same identification number and coordinates defined by *Thomas et al.* (2014, 2016) global hollows map for consistency. In addition, we report the name of the crater hosting hollows (retrieved from the Quickmap, where possible) or the caption 'not crater' if the group is not related to craters. Finally, we report an image of the geomorphological settings in which hollows are located outlined by red arrows. In this way, we perform a complete

database of all hollows located in the High-Mg Region thanks to the complete availability of all the WAC and NAC images available after the end of MESSENGER mission.
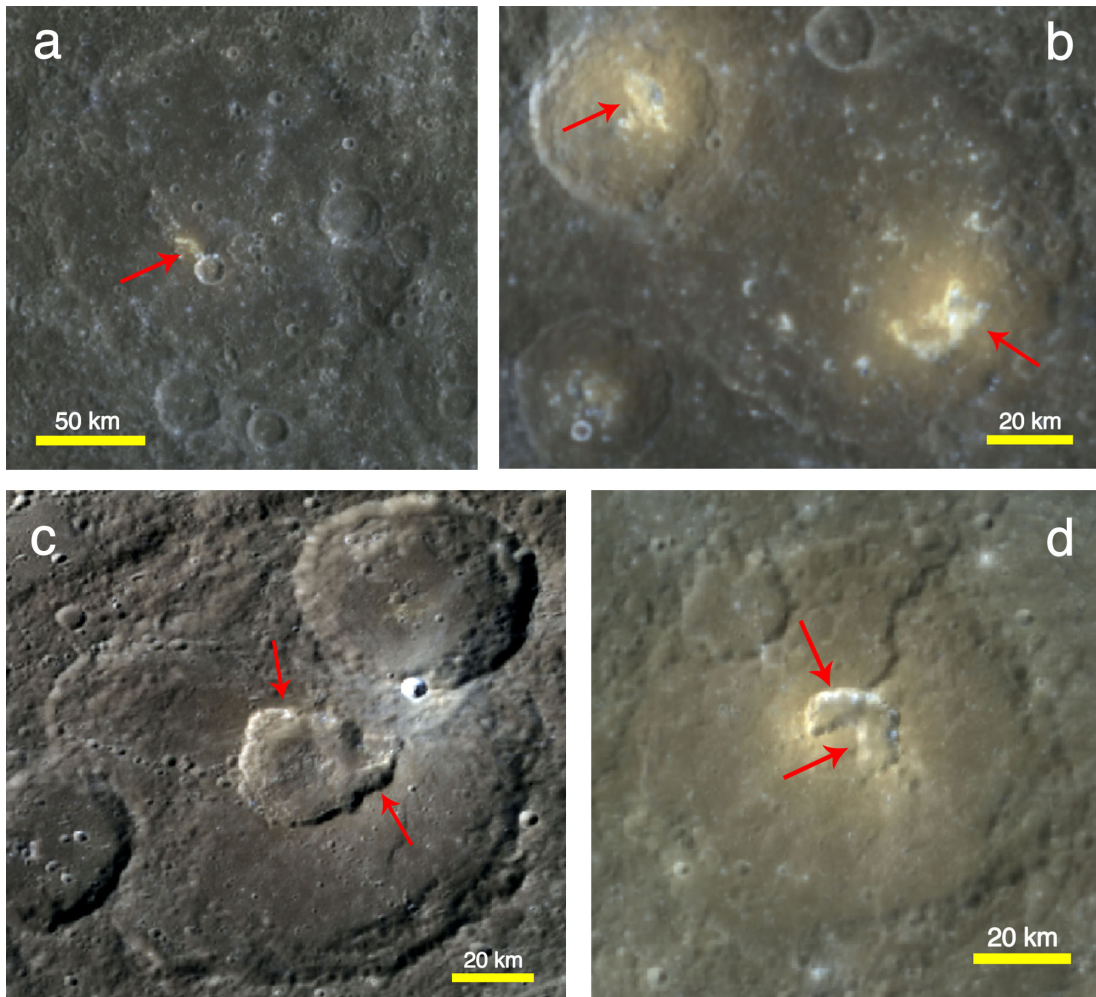
Figure 4.1: *Images taken from the Quickmap 3-color high-resolution map of the northern hemisphere. The red arrows outline hollows in the proximity of pits and pyroclastic material. (a) Probably tubular lava channel hosting hollows in crater Chaikovskij. (b) Large expanses of hollows in areas covered by pyroclasts in crater Mistral (on the right) and unnamed crater (upper left). (c) Hollows on the rims of a large irregular volcanic vent in the center of crater Gibran. (d) Hollows on the rims of an irregular pit surrounded by pyroclastic material in crater Glinka.*

## 4.1 Location of hollows depending on their geological setting

From the analysis of WAC images and the Quickmap, in the HMR we noticed the presence of hollows in a variety of geological settings of the HMR, most of which occurring within impact craters and basins. In order to make a more refined analysis, for each hollows

group we identified the precise geological settings in which they are located. If hollows were found within craters or basins, we distinguished among those occurring on the flat or bowl-shaped bottoms (floors), interior sides and walls (rims), central peaks, peak-rings (typical of large complex craters) and inner smaller craters (within larger and older basins) in order to find connections between the type of feature (and its generation) and the formation mechanisms of hollows. In the following section we give a short summary of the main characteristics of impact craters formation.

4.1.1   Overview on impact craters

When a small body (a meteoroid, an asteroid or a comet) crosses the orbit of a greater rocky body (such as a planet) or is captured by its gravity field, if it survives the atmospheric friction it can strike the surface of the planet at a speed of tens of km/s, thus forming an impact crater. At the very first contact with the surface, the meteoroid compresses the top layer forming shockwaves which propagate in the target material and in the impactor itself. Subsequently, a release wave propagates from the impactor to the surface, and the meteorite can melt or be vaporized. After the phase of contact and compression, the shockwave and the release wave decay in strength as the impact area enlarges, thus starting the excavation phase. The compressed material is pushed downward and out of the rims, forming the ejecta which are a mixture of melt and fractured rock: the result is known as transient crater. When the excavation force cannot throw material outside the crater anymore, there is the modification phase. During this phase, the higher rims of the crater tend to collapse inward under the gravity force, forming part of a breccia lens inside the crater. The appearance of the structures which characterize an impact crater depends on the complexity of the crater itself, that is the result of several factors, among which the size, density and speed of the meteorite and the density of the crust and the total mass of the planet. As a consequence, craters can be classified in simple craters, complex craters and multi-ring basins. If the projectile is small, it can create a simple crater according to the phase-sequence described above. The result is a bowl-shaped crater characterized by a slope rapidly decreasing from the rims towards the center (figure 4.2). If the impacting body is larger, it can penetrate deeper in the crust through different layers. The rock is melted and made flow downward and outward (as in the simple case) but, after the crust is compressed downward by the shockwave, the release wave passes and the crust rebounds. This deeper crust then rapidly uplifts, forming a central peak or a similar ring-shaped structure (the peak-ring) without the presence of breccia or melt. The floor of these complex craters is covered in a sheet of melt above a melt-breccias

mixture, while the surrounding terrain is overlaid by the ejecta, as in the previous case.

In addition, the rim is a composition of terraces of material collapsing towards the crater floor in the modification phase. Finally, the largest type of craters is known as 'multi-ring basin', and consists of two asymmetric, inward-facing scarped rings (one of which may be the original rim, *Hartmann & Wood*, 1971). This kind of craters can have the aspect of complex peak-ring craters, but basins are not characterized by collapsing terraces at the rim. Indeed, these basins are not thought to form in the same way as the complex craters but are probably affected by differences in the structure and the composition of the planetary crust.
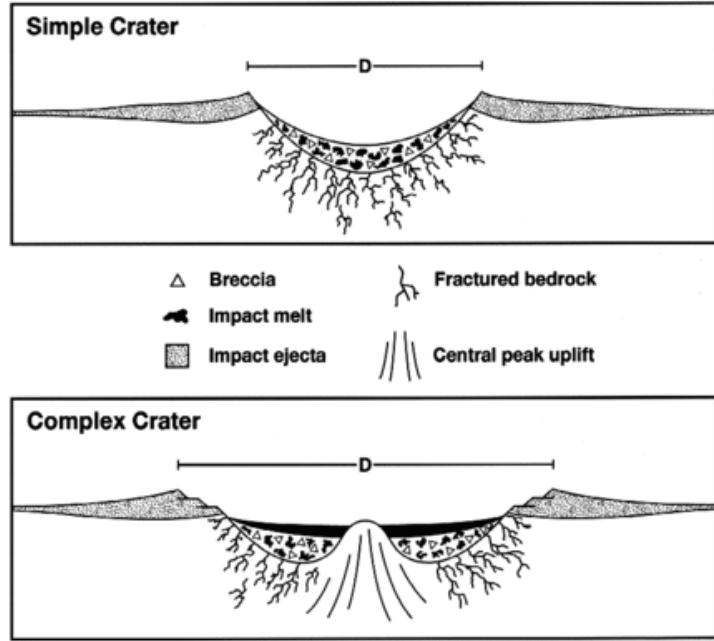
Figure 4.2: *Illustration of the structures of simple and complex craters. Small craters are filled of melt and breccias, while larger craters present a central or ring-like uplift of deeper material.*

## 4.1.2 Analysis of the geological settings in the High-Magnesium Region

It is important to point out the different nature of the geological settings in which hollows have been found. As explained above, the crater floor is made of melt material and fractured rock, the rim is an accumulation of the top layers collapsing and sliding down the scarp, while the central peaks and peak-rings are the result of the exhuming of deep crustal layers. As a consequence, hollows could expose different types of material coming from different depths, which may influence their formation. In addition, considering the volatile-depletion theories discussed in section 2.1.3, the determination of the nature of these volatiles can be a powerful tool to constrain the composition of Mercury's crust (and vice versa) and to understand the criteria for the formation of hollows. Indeed, we found hollows only in some places and, hence, there could be similarities between these different regions. At the same time, hollows have also been noticed on flat or rough terrains not

associated to craters, and consequently we considered these as a stand-alone class.

Therefore, we divided the 85 groups in the following four categories (figure 4.3):

- Floor/rim

- Peak/peak-ring

- Inner craters

- Not-crater terrains

Floor and rim were considered as a single category, being common parts of all simple and complex craters, while peak and peak-ring were grouped together for their common origin and their similar structure as prominent features above the floor level. The four categories were not disjoint sets as hollows have been observed in more settings within the same crater, hence, several groups appeared in multiple categories (obviously, those belonging to the 'not-crater terrains' category could not be part of the other ones). In order to
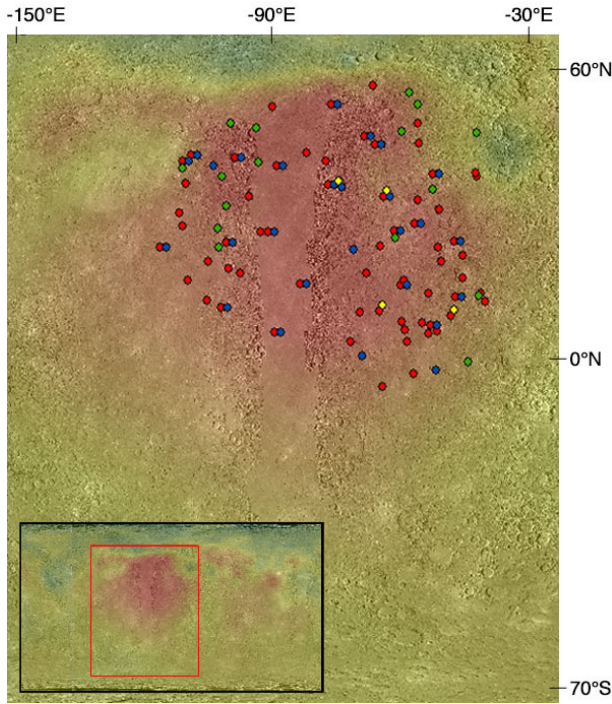
Figure 4.3: *Illustration of the High-Magnesium Region extracted from the Mercury global ratio map obtained by Weider et al. (2015) (shown in the lower left corner). The background colors represent the relative abundance of Mg/Si, increasing from green to red. The circles denote hollows in the four categories: red for floor/rim, blue for peak/peak-ring, yellow for inner craters and green for not crater terrains.*

provide concrete statistical results, we organized the four classes in different tables, that are shown from page 43 to 50. Each table reports the hollows group identification number, its latitude and longitude, its areal extension in km^2 (these four data were retrieved from *Thomas et al.*, 2016), the crater name (where possible) and the hosting geological settings for the given group. In addition, we report if at least one high-resolution image of the hollows group had been catalogued by *Blewett et al.* (2016) (HR column), and if at least

one hollow depth was calculated by *Blewett et al.* (2016) (Depth column). Eventually, in the "Notes" column we specify if these groups were then mapped in greater detail to measure the hollows dimension and extension (the full procedure is explained in section 4.2) and if they are found in association with volcanic pits and pyroclastic material. The analysis developed in this section allowed to retrieve important statistical constraints on the distribution of hollows in the HMR. It results that hollows are associated to impact craters in 69 out of 85 groups, corresponding to the 81.2% of the entire dataset, which is quite consistent with the 84.5% out of 608 groups retrieved by *Thomas et al.* (2014) for the whole surface of the planet. It is evident that hollows tend to form preferentially on the floor of craters and basins: quantitatively they are 64 groups, (75.3%), of which 30 occurred only on the floor (46.9%) and 9 only on the rim (14.1%). It may be likely due to the larger superficial extension covered by these kinds of settings and must be considered in the evaluation of the formation hypotheses described in section 2.1.3. Indeed, the bombardment of the surface due to ions, micrometeoroids and solar radiation may be principally responsible for the depletion of volatiles, and hence, the formation of shallow depressions (*Blewett et al.*, 2013). Crater floors and rims are covered in a thin sheet of melt material and rock in a phase that is susceptible to decomposition caused by sputtering and solar heating, thus favoring the formation and growth of hollows until the hollow floor gets covered in a layer of protective lag which interrupts the volatile-depletion. Based on this assumption, larger and older craters should be completely covered in hollows. However, there is no evidence of this, thus hollows may form only in places in which the suitable conditions of temperature and volatiles concentration are fulfilled (*Blewett et al.*, 2016). Actually, the perfect conditions of hollows formation are still under study, but the forthcoming start of ESA BepiColombo mission will hopefully provide useful results in the next future. Beyond crater floors and rims, we identified hollows on craters peaks and peak-rings. Indeed, we found 26 groups (30.6%) on these structures, which are almost equally distributed between peaks and peak-rings (12 on central peaks and 14 on peak-rings). The formation and growth on such prominent structures should be strongly linked to the parent material, which is pushed from greater depth to the surface by large impacts (*Blewett et al.*, 2011). This means that hollows found on these craters features are constituted by material coming from larger depth compared to hollows found on floors and can provide additional information about the composition of the planet. Moreover, small impactors striking the floor of older deep basins may have the capability to further excavate the same deeper crustal layers, thus forming smaller (often complex) craters covered in this deep low-reflectance material and surrounded by the LRM shallower material overlaying the basin floors. We found hollows within these fresher 'offspring' craters in 4 groups (4.7%),

proving i) either the innate presence of 'depletable' volatiles at very different depths or the high efficiency of a volatile-transfer mechanism, and ii) the existence of a unique process of hollow formation acting on different crustal layers exposed to extreme space weathering, even in locations not related to impacts. Hollows occurring on terrains not associated to impacts constitutes a clear peculiarity. The fraction of groups of this category in the HMR is 18.8% (16 groups), which is in good accordance with the 15.5% reported in *Thomas et al.* (2014) for the total groups on the whole surface of Mercury and corresponding to the 2.5% of the total hollowed area. This shows that the occurrence of hollows outside impact craters represents an anomaly whose formation needs an explanation which would be interesting to investigate (that, however, goes beyond the purposes of this thesis).

In order to verify if the occurrence of groups of each category is directly correlated with the total areal extensions of hollows, we performed the following analysis. We retrieved the overall hollowed area in the floor/rim, peak/peak-ring and not-crater terrains categories, by summing up the areas of the single groups. Additionally, we computed the mean and the median values of the areas for the same three groups. We neglected the inner craters category due to the exiguity of its groups (only 4 out of the total 85). The results are shown in table 4.1. Moreover, we realized a histogram for each category, indicating the frequency of occurrence of groups in areal bins of different width. We set 5 km^2 bins for the floor/rim, 5 km^2 for the peak/peak-ring and 0.1 km^2 for the not-crater terrains, thus obtaining the histograms in figure 4.4.

	Floor/rim	Peak/peak-rim	Not-crater terrains
Total area [km^2]	17912.21	3982.88	42.29
Mean area [km^2]	279.88	153.19	2.64
Median area [km^2]	18.70	44.63	0.29

Table 4.1: *Total, mean and median areas of hollows groups for the three categories considered in the analysis.*

This analysis returned interesting results. The first evidence is a confirmation of the correlation between the number of hollows groups for each category and their total areal extension. They fill the largest area on the floors and rims of impact craters, while outside craters hollows occupy an area which is (a bit less than) three orders of magnitude smaller than those associated to craters. Indeed, the total area of hollows within craters is the 99.8% of the total area of hollows in the High-Magnesium Region, which is consistent with the 97.5% reported in *Thomas et al.* (2014) for the whole surface of Mercury. The mean value of the areas of groups follow the same trend as the total areas of the categories: the floor/rim is almost twice the peak/peak-ring, while the not-crater terrains is about two orders of magnitude smaller. However, the most peculiar characteristic concerns the
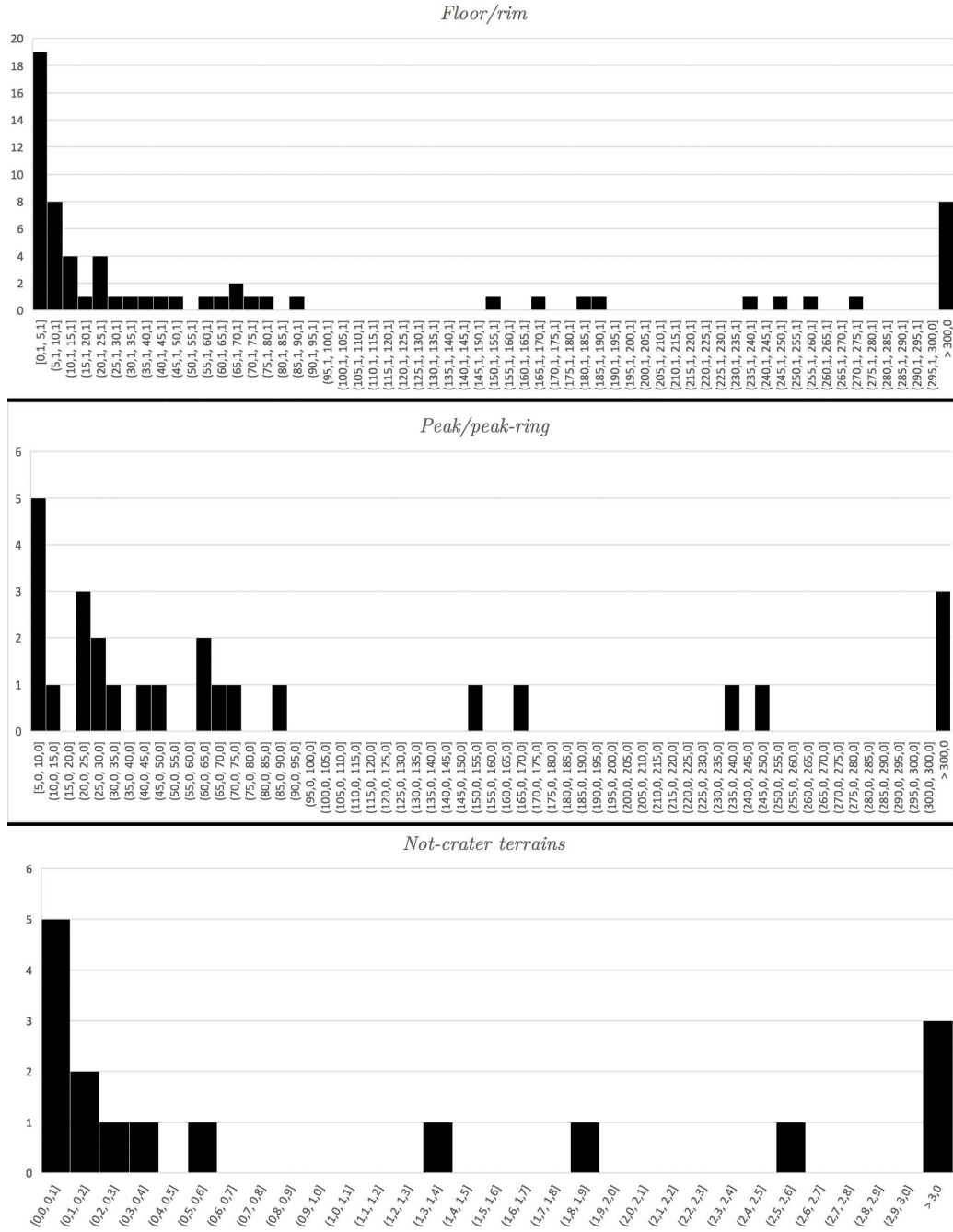
Figure 4.4: *The three histograms show the frequency of the hollows groups (on the Y-axis) depending on their areas (on the X-axis, in km^2) for the three categories. We used 5 km^2 bins for floor/rim and peak/peak-ring, and 0.1 km^2 bins for not-crater terrains.*

distribution of areas in the histograms and the related median values, mainly for the floor/rim and the peak/peak-ring. Indeed, the floor/rim is more peaked for areas below 10 km^2, while the peak/peak-ring category has a more spread distribution having a larger median area than the former.

In the next 8 pages we list the tables relative to the four categories.

Floor/Rim

Group	Lat. °N	Long. °E	Ext. [km²]	HR	Depth	Feature name	Position	Notes
1001	37,392	-55,262	43,147	Yes	Yes	Velazquez	Floor/peak-ring	
1002	47,943	-58,768	0,072	Yes	No	Unnamed crater	Rim	
1003	43,869	-58,498	5,083	No	No	Unnamed crater	Floor	
1010	29,942	-53,798	78,333	No	No	Kuan Han Ching	Floor/rim	
1012	31,957	-58,732	1,071	Yes	No	Unnamed crater	Rim	
1013	26,964	-59,575	1236,514	Yes	Yes	Praxiteles	Floor/peak-ring	Pit, pyroclastic
1014	21,875	-53,965	271,312	No	No	Unnamed crater	Floor	
1015	12,212	-56,344	706,626	No	No	Giotto	Floor/rim	Pit, pyroclastic
1016	5,382	-55,807	64,465	No	No	Unnamed crater	Floor/peak	Measured hollow area
1017	4,327	-54,208	575,253	No	No	Mistral	Floor/rim	Measured hollow area
1018	7,577	-51,176	181,445	No	No	Chaikovskij	Floor/Inner craters	Pit, pyroclastic
1019	11,574	-50,056	22,255	No	No	Unnamed crater	Floor/peak	
1020	15,472	-48,426	6942,687	No	No	Lermontov	Floor/rim	Pit, pyroclastic
1024	3,707	-56,158	328,542	No	No	Unnamed crater	Floor	Pyroclastic
1044	18,877	-53,221	4206,395	No	No	Unnamed crater	Floor/rim	Pyroclastic
1048	14,01	-62,764	422,622	No	No	Unnamed crater	Floor/rim/peak-ring	
1055	14,99	-61,928	20,942	No	No	Unnamed crater	Floor/rim	
1060	25,374	-64,311	74,153	Yes	No	Unnamed crater	Floor/rim/peak	Pyroclastic
1061	6,275	-62,437	4,839	No	No	Unnamed crater	Rim	
1062	4,506	-61,747	35,827	No	No	Unnamed crater	Floor/rim	

Floor/rim

Group	Lat. °N	Long. °E	Ext. [km²]	HR	Depth	Feature name	Position	Notes
1063	-4,695	-59,663	186,754	No	No	Unnamed crater	Floor/Rim	
1075	23,067	-50,236	4,956	No	No	Unnamed crater	Floor/peak	
1077	20,177	-48,203	14,318	No	No	Unnamed crater	Floor/rim	
1080	5,898	-57,871	3,286	No	No	Unnamed crater	Floor/rim	
1081	2,122	-61,3	1,191	No	No	Unnamed crater	Floor/rim	
1082	37,521	-45,354	0,466	Yes	No	Unnamed crater	Floor/rim	
1083	36,799	-44,987	0,346	No	No	Unnamed crater	Floor	
7001	52,025	-78,864	6,994	Yes	Yes	Stravinsky	Floor/peak-ring	
7002	32,72	-98,031	4,422	Yes	Yes	Mussorgskij	Floor	Pyroclastic
7009	43,557	-68,636	166,21	Yes	Yes	Larrocha	Floor/rim/peak-ring	Pyroclastic
7011	35,05	-79,582	46,109	No	No	Unnamed crater	Floor/rim/peak	
7014	32,626	-66,788	28,13	Yes	Yes	Jobim	Floor/peak-ring/inner crater	
7015	45,161	-71,294	6,981	Yes	Yes	Unnamed crater	Floor/peak	
7016	51,5	-92,56	256,357	Yes	Yes	Sholem Aleichem	Floor/rim	Pyroclastic
7018	40,705	-101,255	249,03	Yes	Yes	Scarlatti	Floor/rim/peak-ring	Pit, pyroclastic
7025	41,394	-111,567	6,211	No	No	Whitman	Floor/peak	
7028	39,143	-91,535	86,502	Yes	Yes	Al Hamadhani	Floor/Rim/peak-ring	
7033	39,976	-80,259	4,801	No	No	Unnamed crater	Floor/rim	
7059	41,752	-84,535	2,819	No	No	Unnamed crater	Floor	

Floor/rim

Group	Lat. °N	Long. °E	Ext. [km²]	HR	Depth	Feature name	Position	Notes
7073	21,917	-118,745	152,9	No	No	Durer	Floor/peak-ring	
7112	23,025	-103,195	69,635	Yes	Yes	Mickiewicz	Floor/peak-ring	
7113	26,294	-113,344	57,035	Yes	Yes	Unnamed crater	Floor/rim	Measured hollow area
7120	9,322	-104,432	235,798	No	No	Wang Meng	Floor/peak-ring	Pyroclastic
7122	17,431	-102,68	5,693	No	No	Unnamed crater	Floor	Pyroclastic
7123	18,963	-107,521	4,68	No	No	Unnamed crater	Rim	
7124	15,028	-112,241	13,638	Yes	Yes	Glinka	Central pit	Pit, pyroclastic
7130	16,339	-70,807	1,697	No	No	Unnamed crater	Rim	
7131	14,135	-86,179	874,555	No	No	Vivaldi	Floor/peak-ring	Pyroclastic
7136	10,74	-107,774	5,422	Yes	Yes	Judah Ha Levi	Floor/rim	Measured hollow area
7137	25,072	-95,329	5,603	Yes	Yes	Unnamed crater	Floor	
7138	22,217	-67,584	5,356	Yes	Yes	Catullus	Floor/rim	Pyroclastic
7144	25,079	-93,443	21,65	Yes	Yes	Du Fu	Floor/rim/peak	Pyroclastic
7147	8,473	-67,816	21,163	No	No	Unnamed crater	Floor/inner craters	Pyroclastic
7148	4,033	-92,07	12,586	No	No	Unnamed crater	Floor/peak	
7153	1,933	-74,53	65,4	No	No	Unnamed crater	Floor/rim	
7155	-7,314	-66,92	10,137	No	No	Unnamed crater	Floor	
7156	8,224	-72,062	16,457	No	No	Unnamed crater	Floor/rim	
7169	16,475	-99,92	1,069	No	No	Unnamed crater	Rim	
7179	40,056	-113,513	0,22	Yes	No	Unnamed crater	Floor	

Floor/rim

Group	Lat. ºN	Long. ºE	Ext. [km²]	HR	Depth	Feature name	Position	Notes
7180	55,963	-69,141	0,066	Yes	Yes	Unnamed crater	Rim	
7193	29,209	-114,181	0,135	Yes	No	Unnamed crater	Floor	
7194	35,319	-112,634	0,09	Yes	Yes	Gibran	Floor/central pit	Pit, pyroclastic
8184	12,216	-44,185	32,548	No	No	Unnamed crater	Rim	Pyroclastic
8187	10,565	-43,001	1,212	No	No	Unnamed crater	Rim	

Peak/Peak-Ring

Group	Lat. °N	Long. °E	Ext. [km²]	HR	Depth	Feature name	Position	Notes
1001	37,392	-55,262	43,147	Yes	Yes	Velazquez	Floor/Peak-Ring	
1013	26,964	-59,575	1236,514	Yes	Yes	Praxiteles	Floor/Peak-Ring	Pit, pyroclastic
1016	5,382	-55,807	64,465	No	No	Unnamed crater	Floor/Peak	Pyroclastic
1019	11,574	-50,056	22,255	No	No	Unnamed crater	Floor/Peak	
1026	-3,95	-56,143	8,317	No	No	Calvino	Peak	
1048	14,01	-62,764	422,622	No	No	Unnamed crater	Floor/Rim/Peak-Ring	
1060	25,374	-64,311	74,153	Yes	No	Unnamed crater	Floor/Rim/Peak	Pyroclastic
1075	23,067	-50,236	4,956	No	No	Unnamed crater	Floor/Peak	
7001	52,025	-78,864	6,994	Yes	Yes	Stravinsky	Floor/Peak-Ring	
7009	43,557	-68,636	166,21	Yes	Yes	Larrocha	Floor/Rim/Peak-Ring	Measured hollow area
7010	34,646	-78,011	60,041	Yes	Yes	Aksakov	Peak-Ring/Inner Crater	
7011	35,05	-79,582	46,109	Yes	Yes	Unnamed crater	Floor/Peak/Rim	
7014	32,626	-66,788	28,13	Yes	Yes	Jobim	Floor/Peak-Ring/Inner Crater	
7015	45,161	-71,294	6,981	Yes	Yes	Unnamed crater	Floor/Peak	
7018	40,705	-101,255	249,03	Yes	Yes	Scarlatti	Floor/Rim/Peak-Ring	Measured hollow area
7025	41,394	-111,567	6,211	No	No	Whitman	Floor/Peak	
7028	39,143	-91,535	86,502	Yes	Yes	Al Hamadhani	Floor/Rim/Peak-Ring	
7029	38,976	-107,794	22,026	Yes	Yes	Unnamed crater	Peak	Measured hollow area
7070	-0,976	-73,192	32,621	No	No	Boethius	Peak-Ring	
7073	21,917	-118,745	152,9	Yes	Yes	Durer	Floor/Peak-Ring	Measured hollow area

Peak/peak-ring

Group	Lat. °N	Long. °E	Ext. [km²]	Depth	HR	Feature name	Position	Notes
7112	23,025	-103,195	69,635	Yes	Yes	Mickiewicz	Floor/Peak-Ring	
7120	9,322	-104,432	235,798	No	No	Wang Meng	Floor/Peak-Ring	Pyroclastic
7131	14,135	-86,179	874,555	No	No	Vivaldi	Floor/Peak-Ring	Pyroclastic
7139	21,52	-75,048	28,469	No	No	Unnamed crater	Peak	
7144	25,079	-93,443	21,65	Yes	Yes	Du Fu	Floor/Rim/Peak	Pyroclastic
7148	4,033	-92,07	12,586	No	No	Unnamed crater	Floor/Peak	

Inner Craters

Group	Lat. °N	Long. °E	Ext. [km²]	HR	Depth	Feature name	Position	Notes
1018	7,577	-51,176	181,445	No	No	Chaikovskij	Floor/Inner craters	Measured hollow area
7010	34,646	-78,011	60,041	Yes	Yes	Aksakov	Peak-ring/inner crater	Measured hollow area
7014	32,626	-66,788	28,13	Yes	Yes	Jobim	Floor/peak-ring inner craters	Measured hollow area
7147	8,473	-67,816	21,163	No	No	Unnamed crater	Floor/inner craters	Measured hollow area

Not Related to Craters

Group	Lat. °N	Long. °E	Ext. [km²]	HR	Depth	Feature name	Notes
1022	51,553	-59,484	0,324	Yes	Yes	Not crater	
1032	-2,59	-47,827	7,767	No	No	Not crater	
1064	53,894	-61,498	0,127	No	No	Not crater	
1069	33,505	-56,003	0,604	No	No	Not crater	
1073	45,837	-63,167	9,283	No	No	Not crater	
1085	45,57	-45,785	0,141	No	No	Not crater	
1094	11,189	-45,457	1,826	No	No	Not crater	
7072	23,512	-64,795	17,794	No	No	Not crater	
7119	25,383	-105,991	2,59	Yes	Yes	Not crater	Measured hollow area
7172	39,23	-96,487	1,392	No	No	Not crater	
7176	30,05	-103,971	0,257	No	No	Not crater	
7177	21,311	-105,647	0,088	Yes	Yes	Not crater	Measured hollow area
7183	46,621	-96,935	0,026	Yes	No	Not crater	Measured hollow area
7184	36,448	-105,054	0,041	Yes	Yes	Not crater	Measured hollow area
7185	47,565	-103,116	0,005	No	No	Not crater	
7195	38,046	-114,072	0,024	No	No	Not crater	

4.2 Detailed mapping of hollows

One of the main characteristics of hollows is their areal extension. Indeed, this is closely connected with the mechanisms of formation, which determine the initial size of hollows, and the growth rate, which can explain the dimensions that we can measure today. Consequently, the measurement of the areal extension of hollows may be a powerful tool to put constraints on the formation process. Therefore, in order to obtain quantitative results to be compared with the data from the literature, we selected four hollows groups for each category in which to analyze hollows in greater detail. The choice was made on the base of the availability of sufficiently-high-resolution NAC images covering the majority of hollows for a given group. This activity was carried out thanks to ArcGIS software, a Geographic Information System (GIS) developed by ESRI for the creation and visualization of maps, as well as for the analysis and the sharing of geographic information and used in a wide range of application fields. In particular, we made use of ArcMap, which is the main component of ArcGIS, to edit geospatial data. This allows to project geospatially referenced images on a global map and retrieve useful parameters. In our case, the background map was the Mercury MESSENGER Global Basemap, a monochromatic mosaic of Mercury surface imaged by MDIS at a resolution of ~ 166 m/px and 750 nm wavelength, with a $\sim 74^{\circ}$ lighting angle. For each of the 16 groups selected, we considered only the NAC images containing hollows: these images were geometrically and photometrically calibrated in such a way to perfectly overlap the global basemap, and then projected on the basemap itself. Subsequently, we made use of the 'shapefile' tool of ArcMap, which permits to generate a geospatial data vector under the form of points, lines and polygons, from which it is possible to compute distances and areas on the global map. Therefore, we created a shapefile by drawing polygonal broken lines in order to cover all the hollows displayed in the NAC images projected on the basemap. Figures 4.5 and 4.6 show four examples (one for each category) of the mapping of hollows described in this section. The main difficulties in this procedure were due to the fact that some clusters of hollows included in two or more images having different resolutions or imaged only partially, and unsuitable lighting conditions faded and blurred the margins of hollows. For each single hollow or small cluster mapped in the shapefile, we used the ArcMap tool "Calculate Geometry" to retrieve the related area in km^2. Then, we first extracted the radii from all these areas (assuming a circular shape for hollows), and subsequently we summed these areas together, which yielded the total areal extension of the hollows group. Tables 4.2 list the group ID, the latitude, the longitude and the area computed in *Thomas et al.* (2016) for the 16 hollow sites analyzed. Furthermore, we report the minimum, maximum and mean radius

of hollows and the total area of the hollows group measured with the procedure described in this section.

Floor/rim

Group	Lat. °N	Long. °E	R_{min} [m]	R_{max} [m]	R_{mean} [m]	A_{our} [km²]	A_{Th} [km²]
1016	5.382	-55.807	51.82	782.81	234.66	20.97	64.47
1017	4.327	-54.208	100.72	1264.08	315.00	52.76	575.25
7113	26.294	-113.344	18.54	1078.87	105.40	15.16	57.03
7136	10.74	-107.774	37.14	309.47	106.08	1.03	5.42

Peak/peak-ring

Group	Lat. °N	Long. °E	R_{min} [m]	R_{max} [m]	R_{mean} [m]	A_{our} [km²]	A_{Th} [km²]
7009	43.557	-68.636	64.19	632.04	240.53	42.11	166.21
7018	40.705	-101.255	53.94	1299.04	178.88	45.46	249.03
7029	38.976	-107.794	40.95	527.31	146.51	6.02	22.03
7073	21.917	-118.745	38.79	866.28	288.50	25.52	152.90

Inner craters

Group	Lat. °N	Long. °E	R_{min} [m]	R_{max} [m]	R_{mean} [m]	A_{our} [km²]	A_{Th} [km²]
1018	7.577	-51.176	65.99	951.80	300.87	24.21	181.45
7010	34.646	-78.011	32.33	1171.39	199.88	33.24	60.04
7014	32.626	-66.788	56.86	598.03	213.09	9.04	28.13
7147	8.473	-67.816	86.63	825.91	318.58	11.22	21.163

Not-crater terrains

Group	Lat. °N	Long. °E	R_{min} [m]	R_{max} [m]	R_{mean} [m]	A_{our} [km²]	A_{Th} [km²]
7119	25.383	-105.991	205.06	205.06	205.06	0.13	2.59
7177	21.311	-105.647	113.90	148.23	134.83	0.17	0.09
7183	46.621	-96.935	16.13	34.19	27.38	0.02	0.03
7184	36.448	-105.054	38.14	69.59	53.87	0.02	0.04

Table 4.2: *The tables related to the four categories list the ID number of hollows groups, its latitude and longitude, the minimum (R_{min}), maximum (R_{max}) and mean (R_{mean}) radius of the groups, the areal extension computed in this work (A_{our}) and that (A_{Th}) obtained by Thomas et al. (2016).*

We can deduce significant considerations from these data. Firstly, the areal extension of hollows measured in this work are much smaller than those obtained by *Thomas et al.* (2014, 2016). The reason for this discrepancy should be attributed to the different NAC images used to analyze the hollows. Indeed, *Thomas et al.* (2014, 2016) considered NAC images with resolutions < 180 m/px and with an average value of 106 m/px, probably overestimating the real hollows extension. In our work, we used the NAC images having resolution less than of 50-60 m/px, which is a higher value with respect to *Thomas et al.* (2014, 2016) work. This allowed to distinguish the irregular rims of hollows with higher precision. Furthermore, we retrieved an important result regarding the typical size of hollows. As shown in the tables, if we neglect the last two groups of the 'not-crater terrains' category, which refer to single scattered hollows and may be treated as exceptions,

the average size of hollows in our measurements ranges from 105.40 m to 318.58 m. Hence, it is possible to state that, on average, small and large hollows have very similar dimensions of the same order of magnitude and we do not see very large difference between the groups. This characteristic is independent on the category and, hence, from this evidence we can infer that the mechanism which produces hollows could be the same for all the features located in HMR. This means that the volatiles involved in the formation of hollows should be the same because they could be the main responsible in the formation process. The difference between hollows may consist in the bedrock material in which they formed. This results in a similar appearance of hollows, but in a different spectral behavior that depends not only on the volatile components responsible for the formation, but also from the different terrains in which hollows originate (maybe terrains that are excavated by different depths as the crater central peaks).
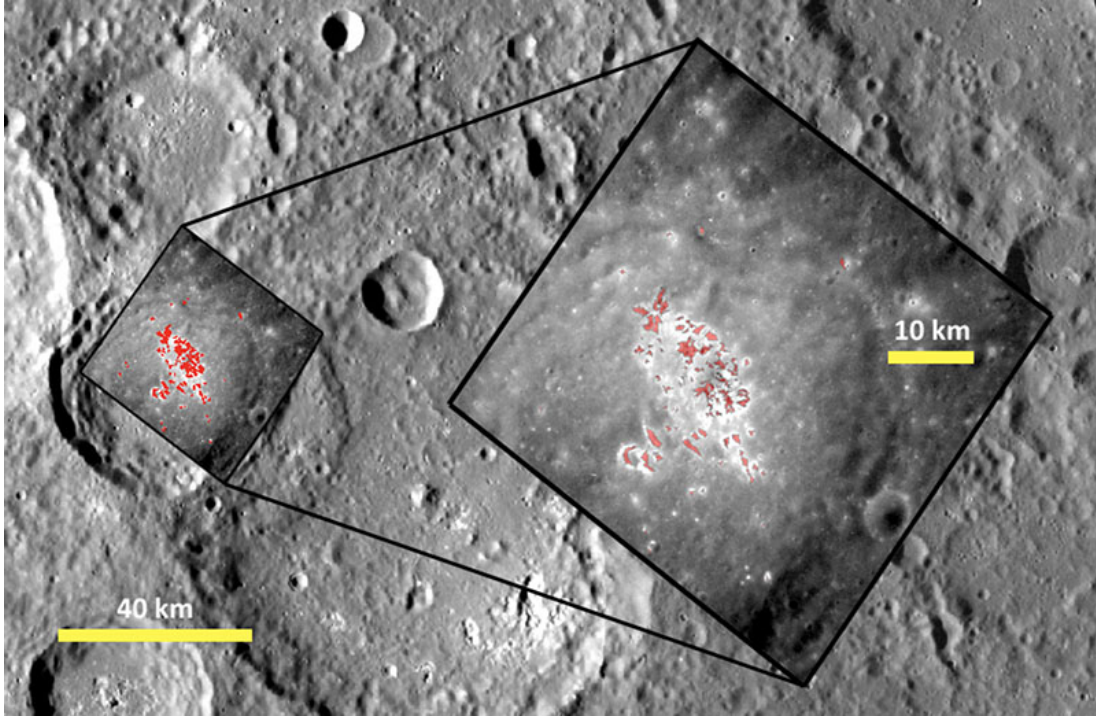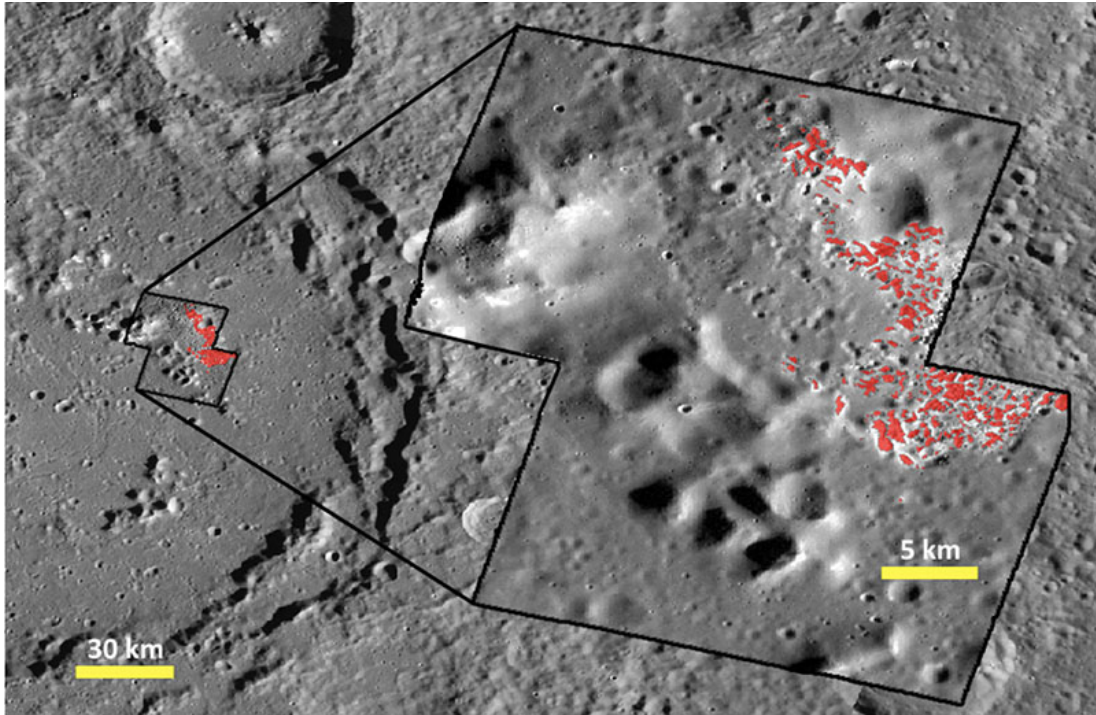
Figure 4.5: *Examples of hollow mapping. (a) Unnamed crater (group ID 1016, centered at 5.382º N, -55.807º E) with floor hosting hollows. The enlarged NAC image on the right is EN1020752552M. (b) Hollows mapped at the base of the peak-ring in Larrocha crater (ID 7009, centered at 43.557º N, -68.636º E). The NAC images are EN0223831195M and EN0223831200M.*
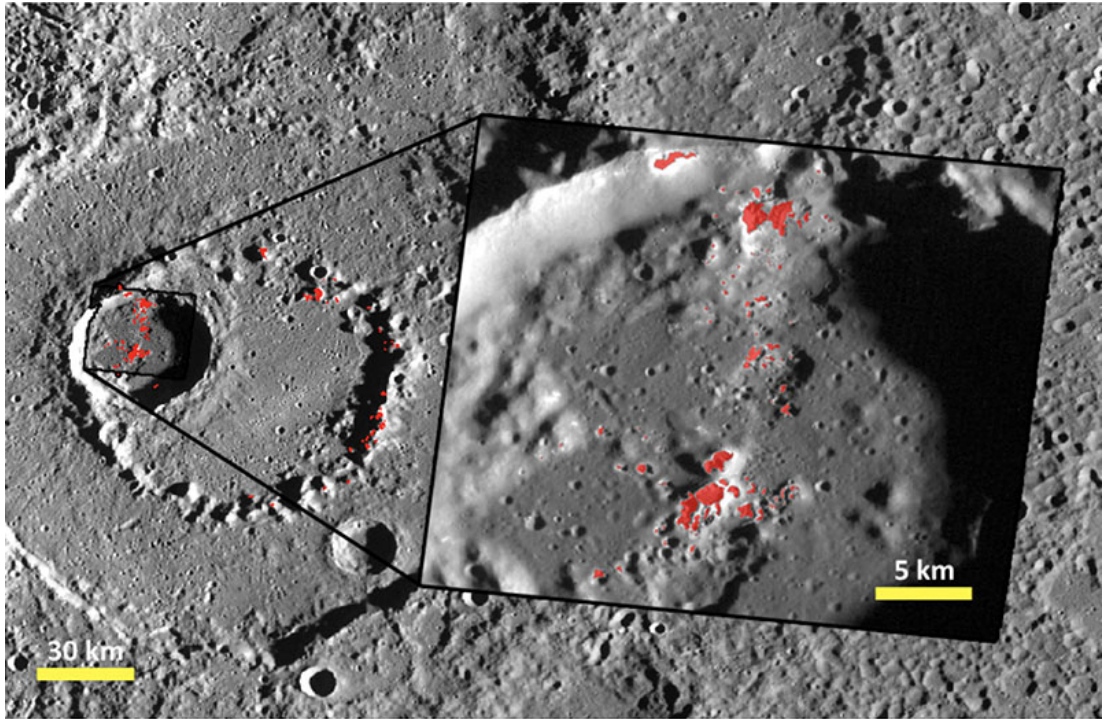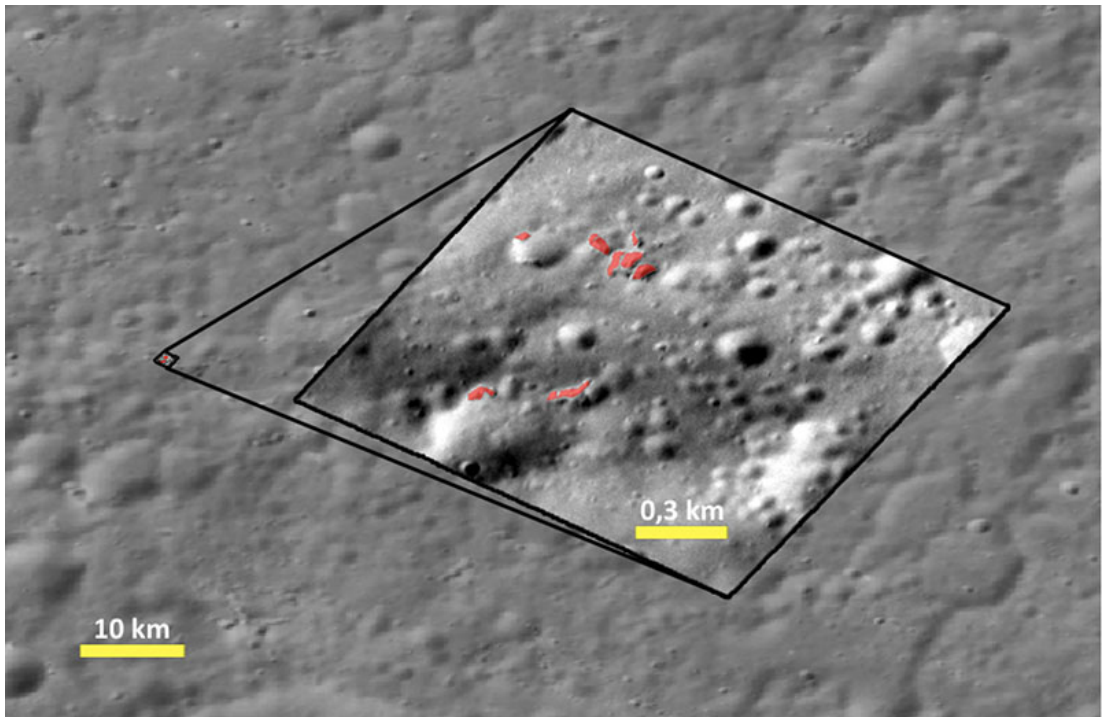
Figure 4.6: *Examples of hollow mapping. (a) Hollows mapped in a small crater within Aksakov crater (ID 7010, centered at 34.646º N, -78.011º E). The NAC image on the right is EN1003298241M. (b) Small disperse hollows on a rolling terrain far from impact craters (ID 7183, centered at 46.621º N, -96.935º E). The NAC image is EN1066914923M.*

Conclusion

In this work we focus on the analysis of hollows located in a restricted region characterized by a high abundance of Magnesium (High-Magnesium Region, HMR) on the surface of Mercury. Thanks to the compositional data from the X-Ray Spectrometer and the images acquired by the Mercury Dual Imaging Camera of NASA MESSENGER mission, we study the statistical distribution of hollows in the HMR that occur within impact craters and basins and on terrains not directly related to impacts structures. The Hermean surface has been subjected to volcanism and impact processes that excavated, mixed and remodeled the top crustal layers. Hence, the correlation between hollows and their host geological settings allow us to make interesting considerations about the theories on hollows formation.

First, we consider the association between hollows in the HMR and volcanic sites, such as pits, vents and pyroclastic deposits. Indeed, we found this relation rather frequent, as already stated in *Thomas et al.* (2014), thus supporting the 'sequestration' hypothesis proposed by *Blewett et al.* (2013) according to which volcanic material has a primary role in the trapping of volatiles, whose depletion originates hollows. Subsequently, we consider the hollows groups (reported in *Thomas et al.*, 2014) occurring only in the HMR and divide them in the following four categories, according to their geological host setting: floor/rim, peak/peak-ring, smaller craters within larger craters and not related to impact craters. We find that hollows occur within craters and basins in 81.2% of cases, consistently with the statistical results reported in *Thomas et al.* (2014) for the whole planetary surface, hence, we mainly focus on the different geological settings present inside craters. 75.3% of hollows groups are located on the floor and the rim of impact craters. This may be due to the fact that the floor, constituting the greatest surface of a crater, is covered in a layer of melt and breccias that are subject to sputtering by extreme space weathering. It causes the depletion of volatiles in the underlying layer, generating hollows through collapse (*Blewett et al.*, 2013). We also point out the occurrence of hollows on the floor of small craters excavated within larger craters or basins (4.7%). In this case, the formation of hollows occurs on deeper layers exposed by fresher impacts. In the case of hollows located on

central peaks and peak-rings (30.6%), we suggest that they form on deep bedrock layers that have been exposed and uplifted much above the floor level because of the impact crater formation. Even if these three host settings are associated to material coming from different depths and with different compositions, we show that their formation process is probably the same. Hollows occurring on terrains not related to craters (18.8%) are a clear peculiarity, which will be studied in greater detail in the next future. We statistically analyzed the frequency of areal extensions of hollows in the floor/rim, peak/peak-ring and not-crater terrains categories, while inner craters were neglected due to their exiguity. As a result, the total and the mean areas of the groups of the floor/rim category have the largest values, followed by peak/peak-ring and not-crater terrains (in the same decreasing order as for the percentage of groups in each category computed previously). Conversely, the median area of the peak/peak-ring groups is larger than the one of the floor/rim category, due to the fact that most of the floor/rim groups areas are accumulated at relatively smaller values than for the peak/peak-ring groups areas, being relatively more spread even at larger values.
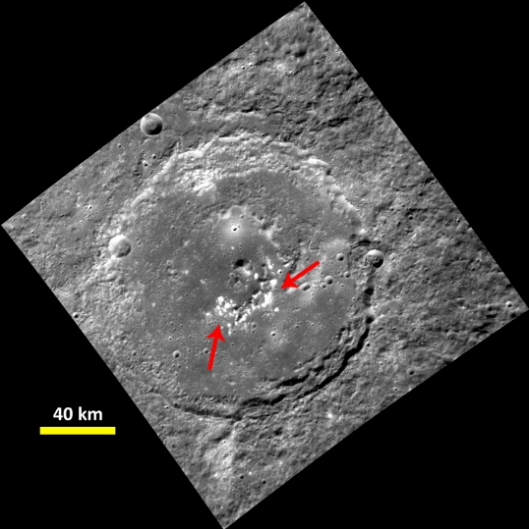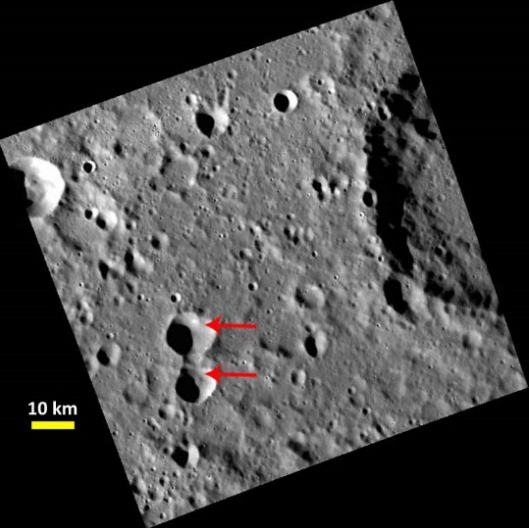
As a second part of our analysis, we selected four hollows groups for each category with a suitable high-resolution images coverage, and we proceeded to map all hollows thanks to ESRI ArcGIS software. For each hollow we calculated the areal extension and the radius, hence, we obtained the typical mean radii of hollows and the total hollowed area in each group. As a result, we found that the groups areas computed in this work are much smaller than those measured by *Thomas et al.* (2016), as in our case a larger availability of high-resolution images was available, and therefore, our measurements are more detailed. In addition, the mean radii of hollows retrieved in our procedure are included between 105.40 m and 318.58 m. It means that hollows have a very similar size regardless the terrain and the geological setting in which they occur, hence, we can deduce that the process of hollow formation and the volatiles involved should be the same for all the categories. However, though hollows have the same appearance, the main difference between these structures could be the composition which is based on the volatile components (that should be similar because directly linked to the formation process) and the different host bedrock terrains.

ESA/JAXA BepiColombo mission will be crucial for the study of this aspect and for the analysis of hollows outside impact craters. Indeed, the upcoming mission will provide satisfying answers to the actual questions on the formation and nature of the hollows on Mercury.

Appendix A

In this table we list all the 85 groups of hollows within the High-Magnesium Region. For each group we indicate the group ID number, the latitude and the longitude (as defined in *Thomas et al.*, 2014, 2016), and the name of the host crater (if present) or the expression 'not crater' if hollows are not associated with impact craters. In the right column, we show an image (or mosaic) with an overview on the geological environment, in which hollows are pointed by red arrows, and the names of the WAC or NAC images used. All images are aligned with the cardinal points and display a yellow scalebar.

Group	Lat. (N)	Long. (E)	Crater name	Image
1001	37,392	-55,262	Velazquez	 EW1005601149G
1002	47,943	-58,768	Unnamed crater	 EW0213416842G

1003	43,869	-58,498	Unnamed crater
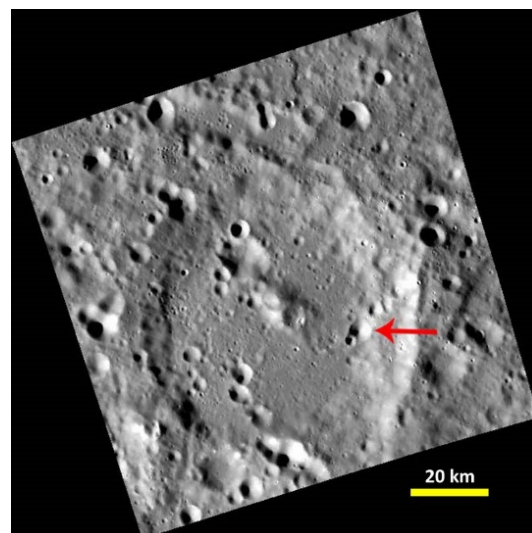
EW0213460365G

1010	29,942	-53,798	Kuan Han Ching
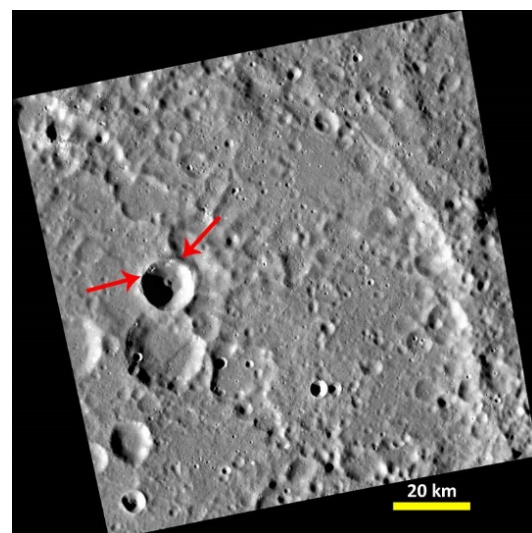
EW0228587174G

1012	31,957	-58,732	Unnamed crater
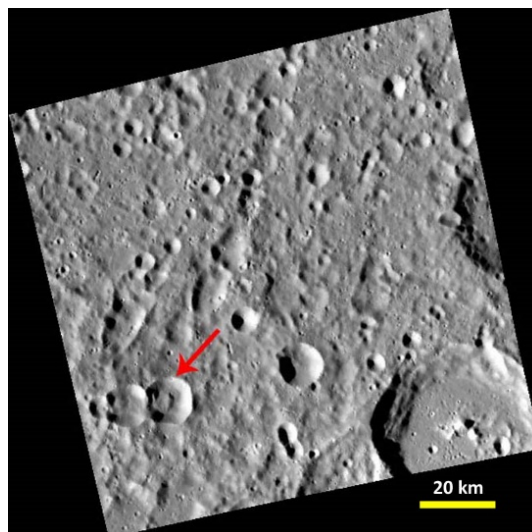
EW0213503995G

1013	26,964	-59,575	Praxiteles
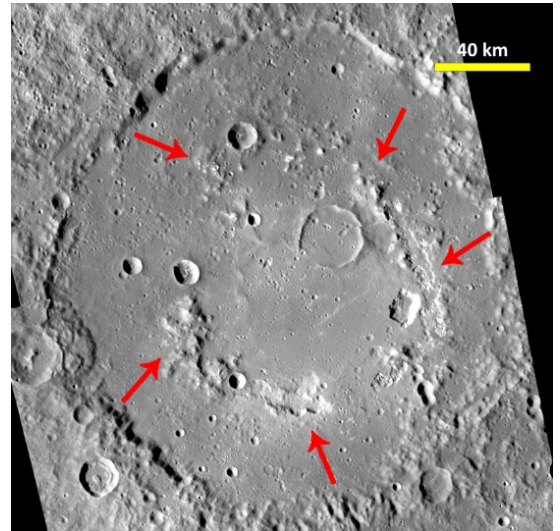
EW0259120911G and EW0259120989G

1014	21,875	-53,965	Unnamed crater
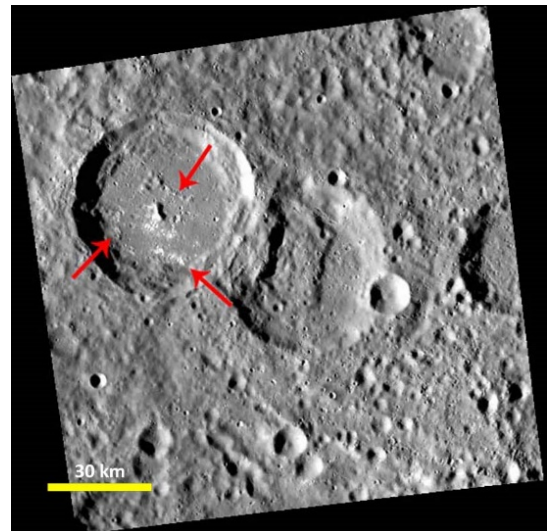
EW0213460704G

1015	12,212	-56,344	Giotto

EW0228673888G

61
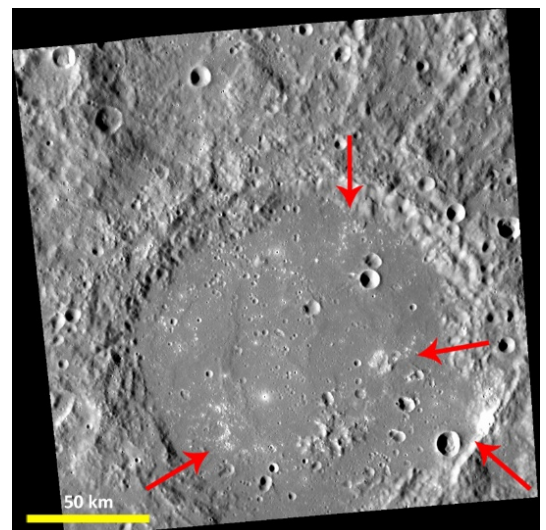
| 1016 | 5,382 | -55,807 | Unnamed crater |
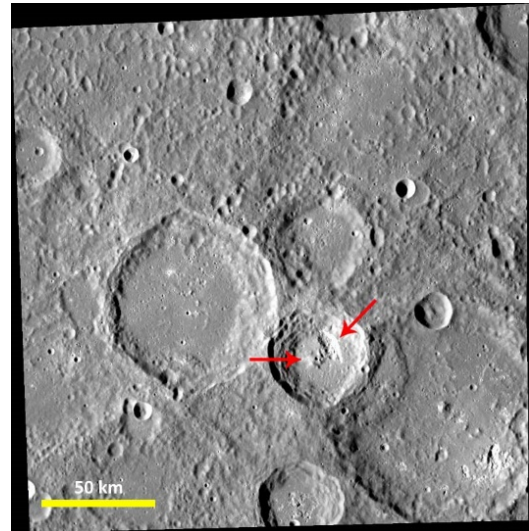
EW0228717251G

| 1017 | 4,327 | -54,208 | Mistral |
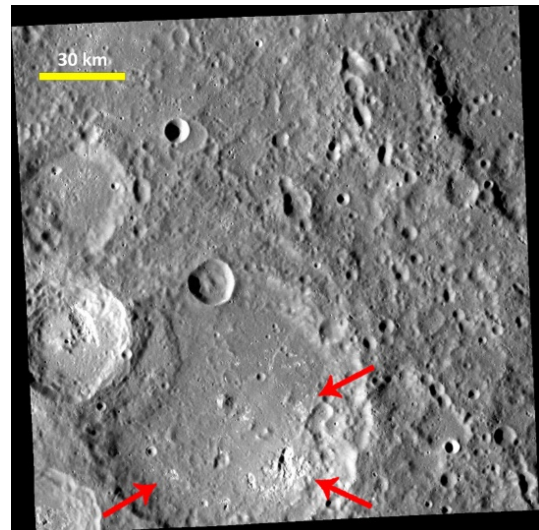
EW0213460985G

| 1018 | 7,577 | -51,176 | Chaikovskij |
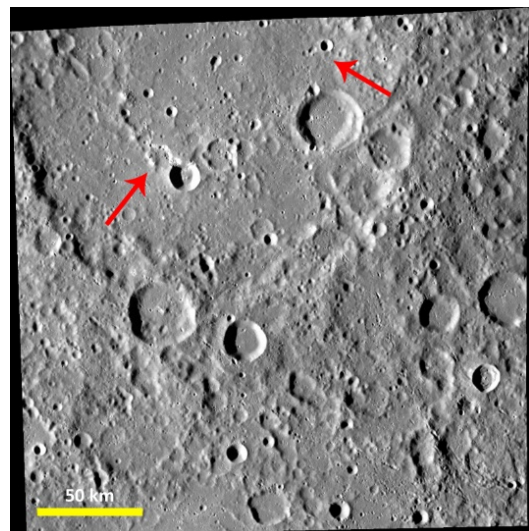
EW0228630853G

| 1019 | 11,574 | -50,056 | Unnamed crater |
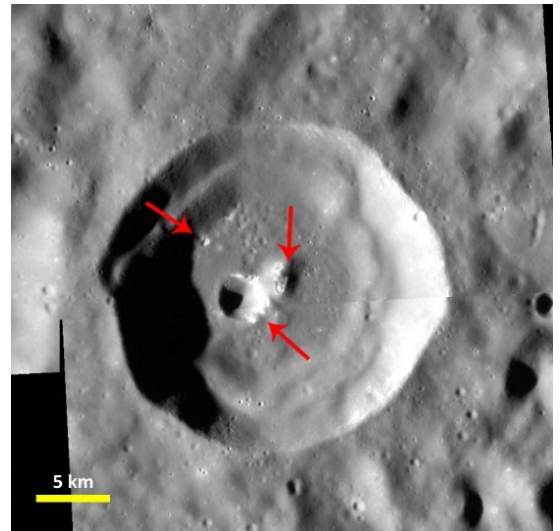
EN0258977274M and EN0258977295M

| 1020 | 15,472 | -48,426 | Lermontov |
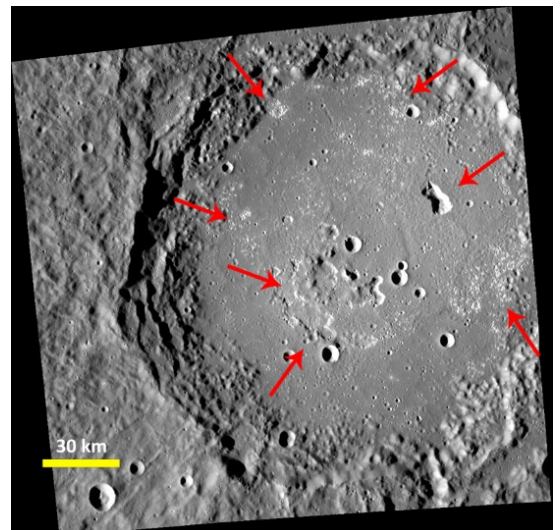
EW0243797322G

| 1022 | 51,553 | -59,484 | Not crater |
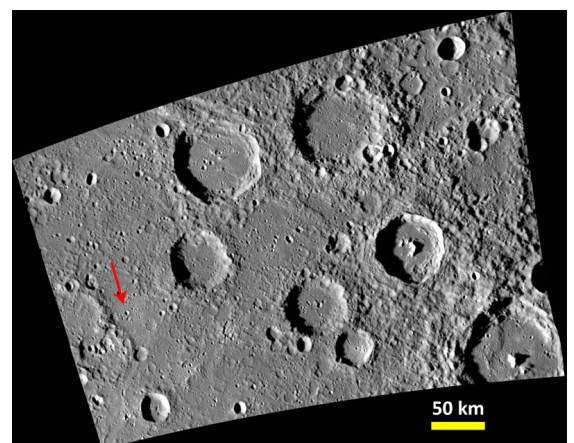
EW1023433318G

| 1024 | 3,707 | -56,158 | Unnamed crater |
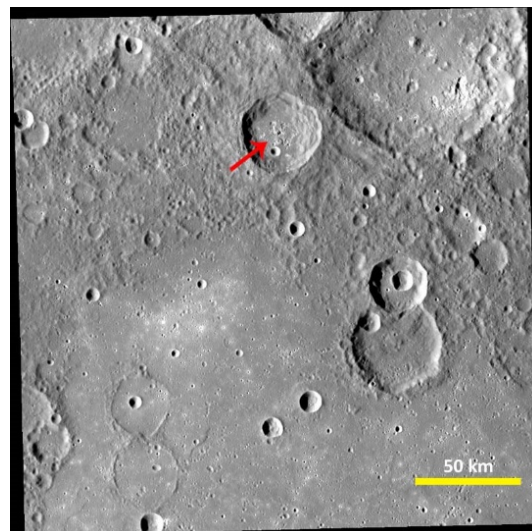
EW0243855215G

| 1026 | -3,95 | -56,143 | Calvino |
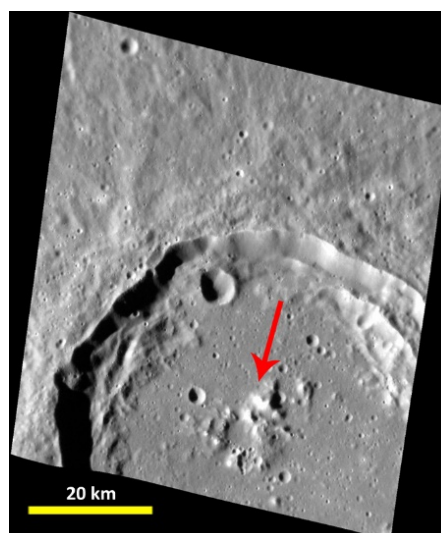
EN0228674673M

| 1032 | -2,59 | -47,827 | Not crater |
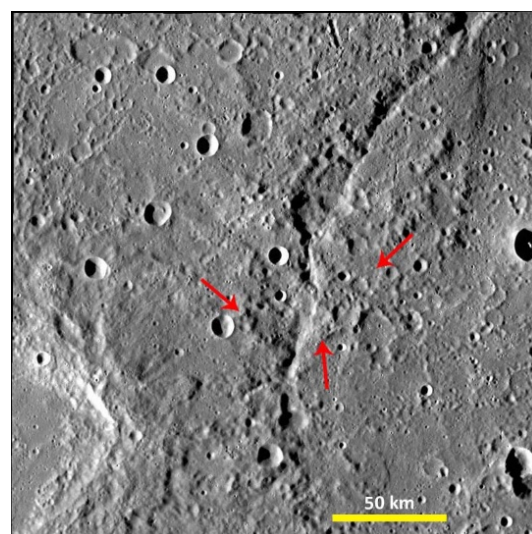
EW0213417704G

1044	18,877	-53,221	Unnamed crater	
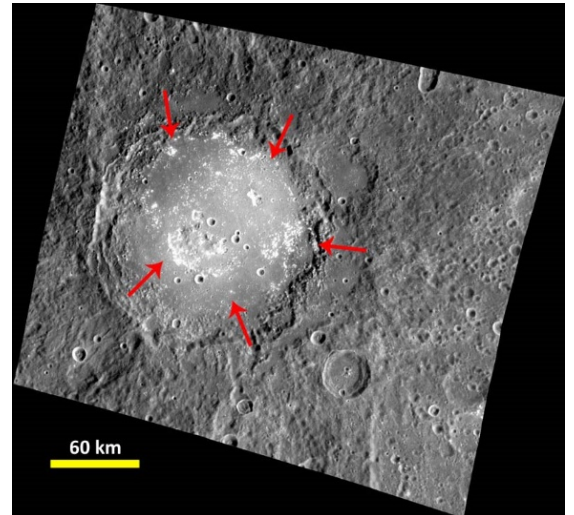
EW1003010557G

1048	14,01	-62,764	Unnamed crater	
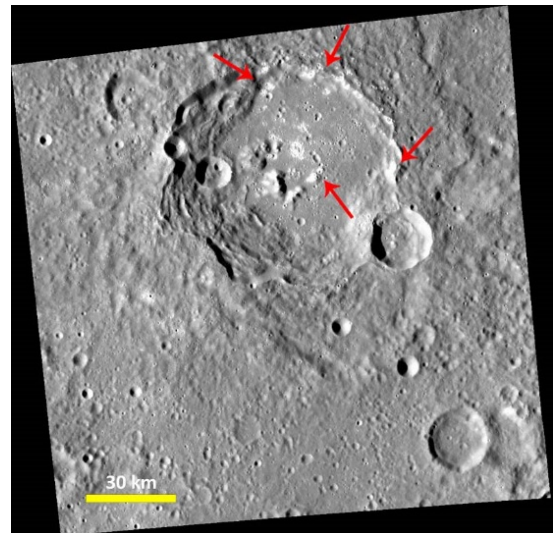
EW0213634699G

1055	14,99	-61,928	Unnamed crater	
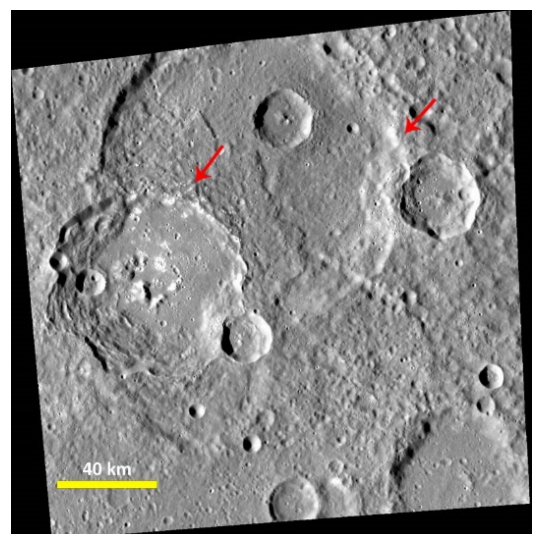
EW0228803487G

| 1060 | 25,374 | -64,311 | Unnamed crater |
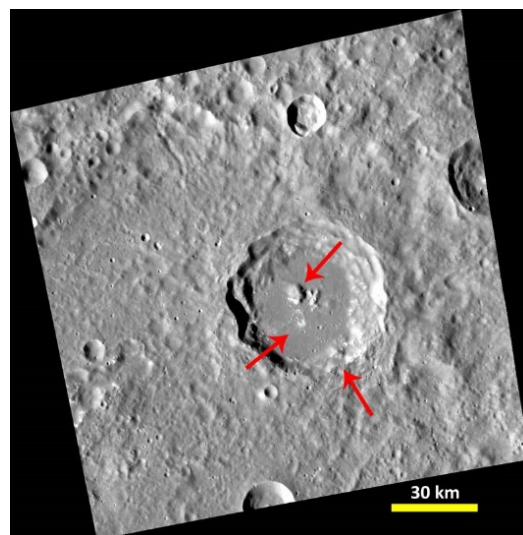
EW0228803252G

| 1061 | 6,275 | -62,437 | Unnamed crater |
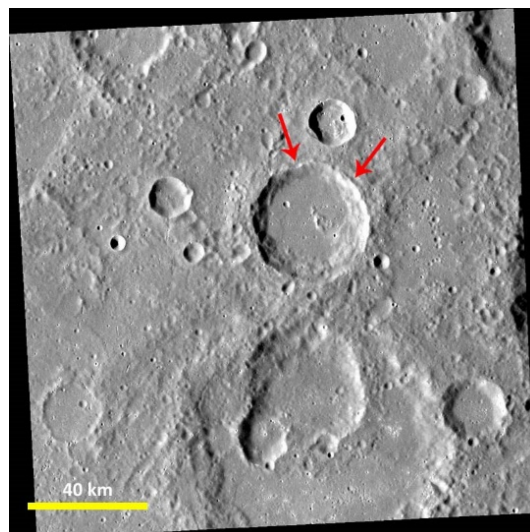
EW0213591369G

| 1062 | 4,506 | -61,747 | Unnamed crater |
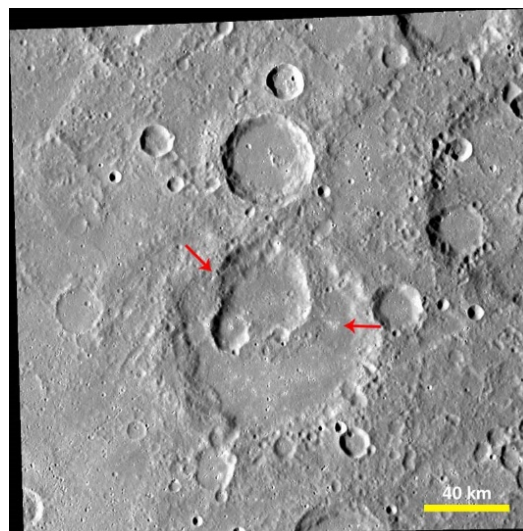
EW0228803683G

1063	-4,695	-59,663	Unnamed crater
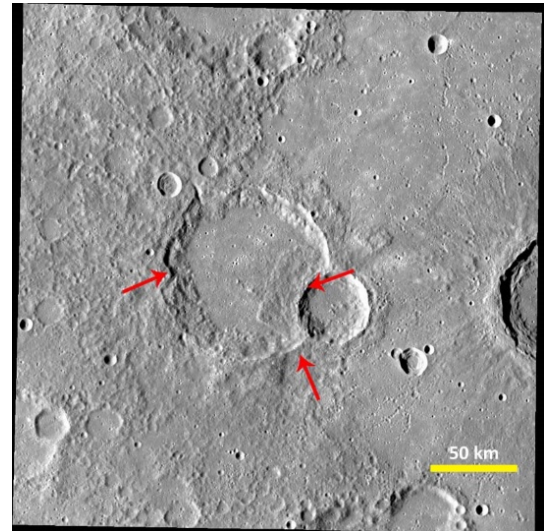
EW0243912976G

1064	53,894	-61,498	Not crater
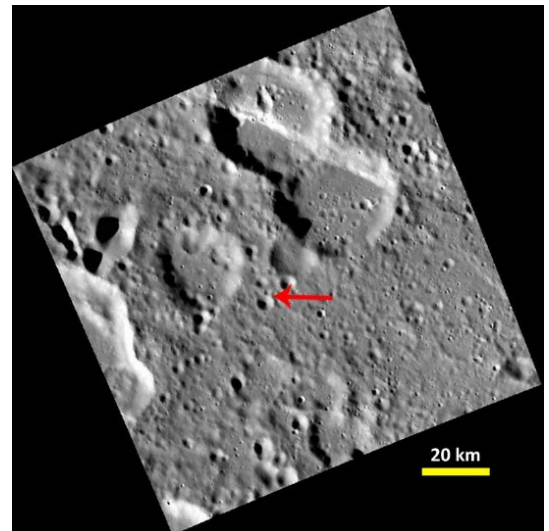
EW0213460230G

1069	33,505	-56,003	Not crater
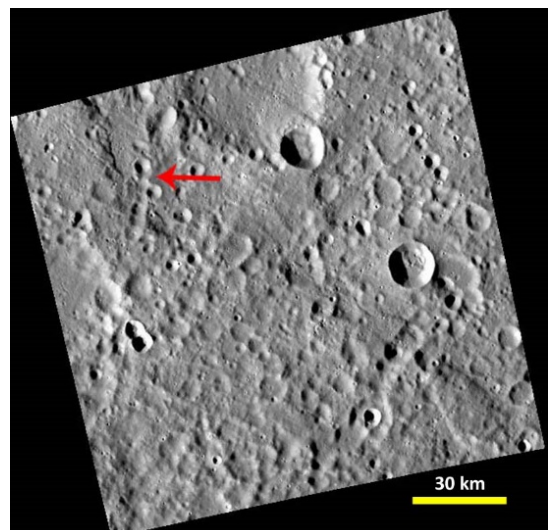
EW0243825802G

| 1073 | 45,837 | -63,167 | Not crater |
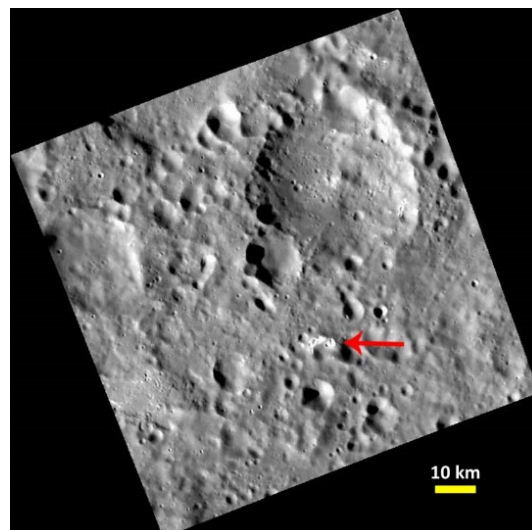
EW0213503794G

| 1075 | 23,067 | -50,236 | Unnamed crater |
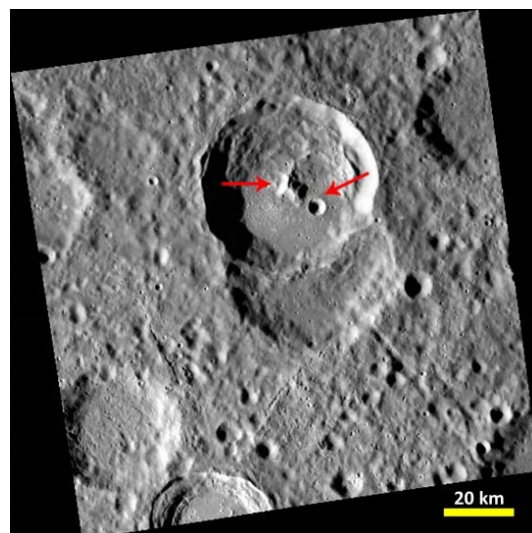
EW0213373762G

| 1077 | 20,177 | -48,203 | Unnamed crater |
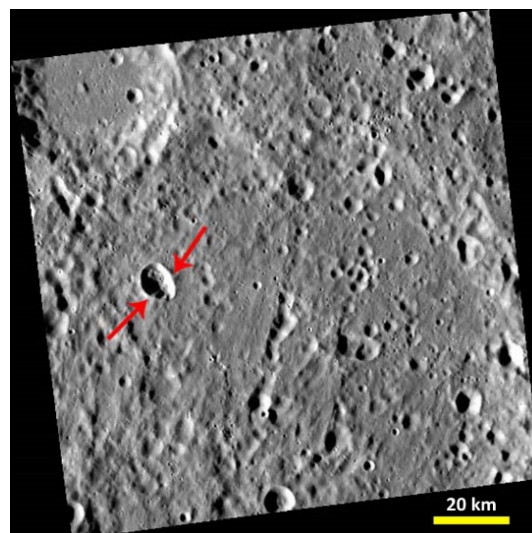
EW0213330342G

| 1080 | 5,898 | -57,871 | Unnamed crater |
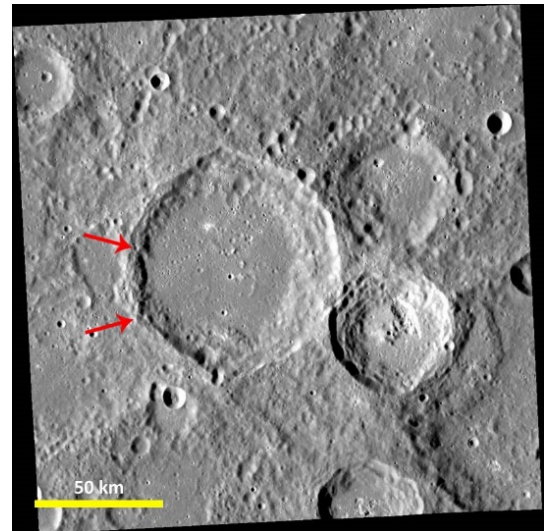
EW0213504446G

| 1081 | 2,122 | -61,3 | Unnamed crater |
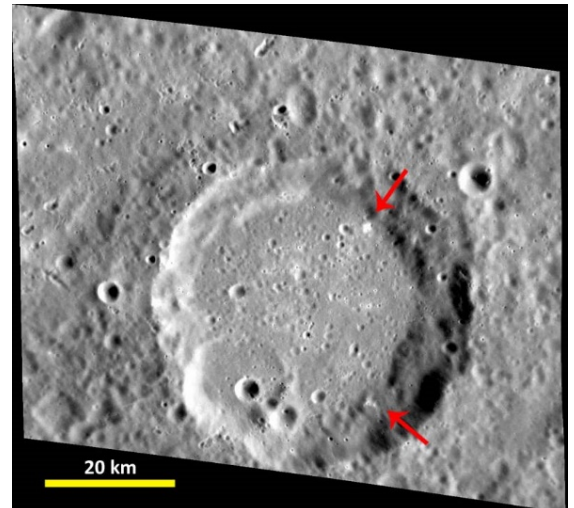
EN1018508513M

| 1082 | 37,521 | -45,354 | Unnamed crater |
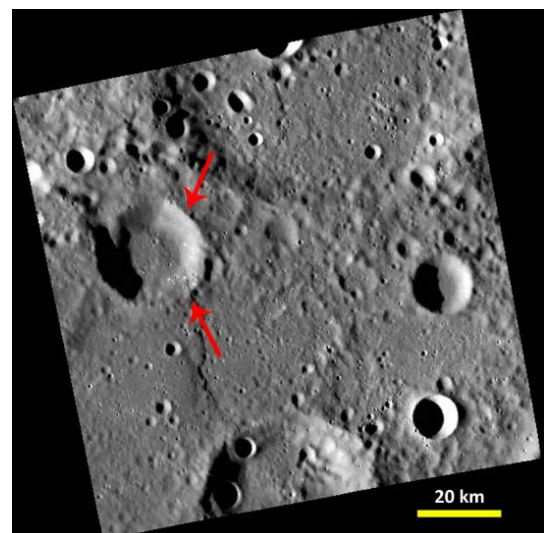
EW0213286621G

EW0213243173G

| 1083 | 36,799 | -44,987 | Unnamed crater |

EW0258832567G

| 1085 | 45,57 | -45,785 | Not crater |
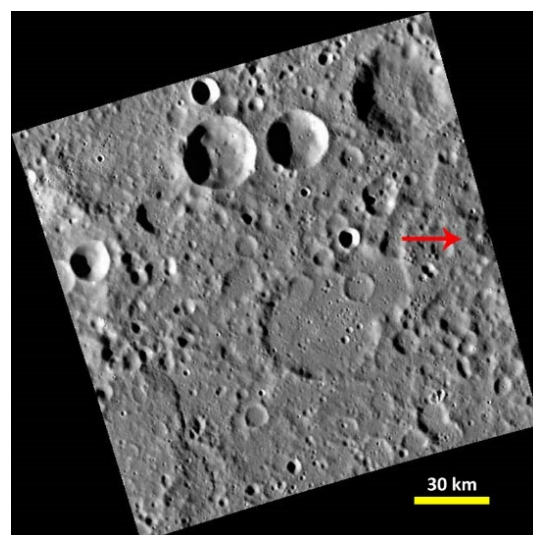
EW0228587545G

| 1094 | 11,189 | -45,457 | Not crater |
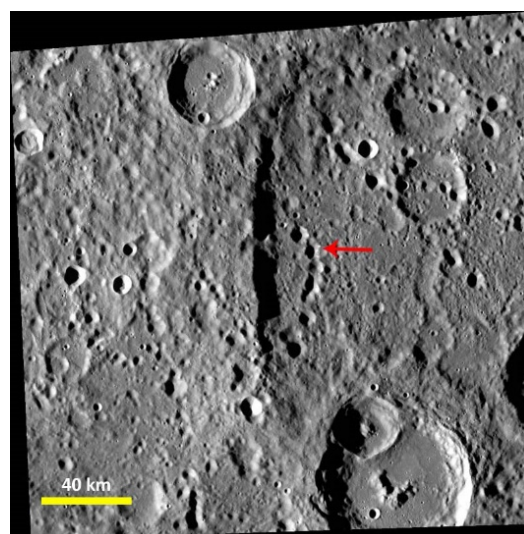
7001	52,025	-78,864	Stravinsky
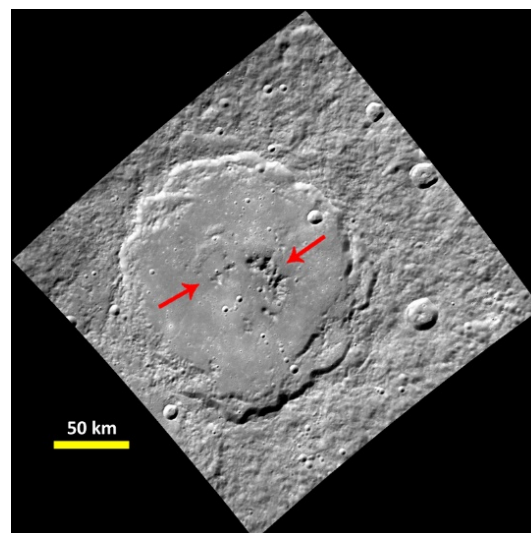
EW0226583677G

7002	32,72	-98,031	Mussorgskij
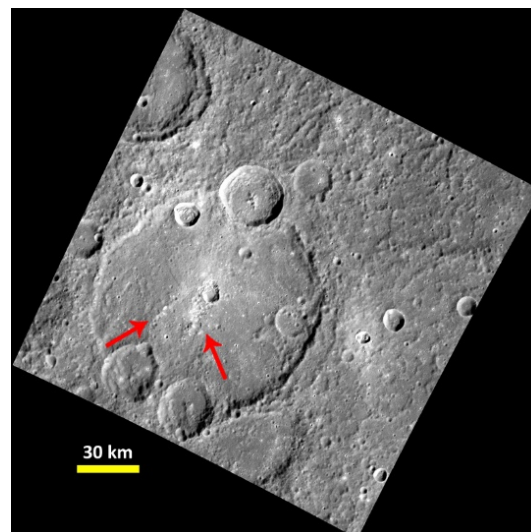
EW1006148313F

7009	43,557	-68,636	Larrocha
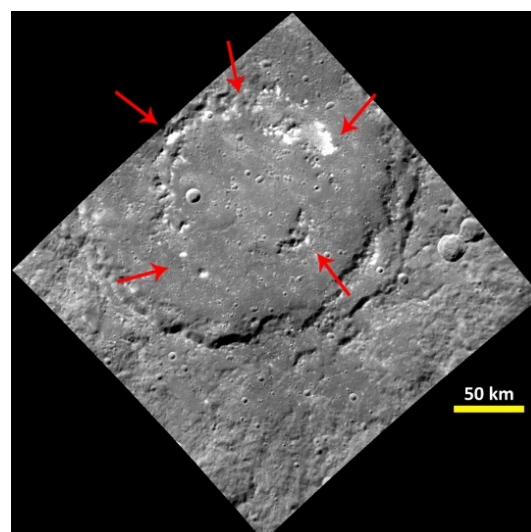
EW0241586303I

7010	34,646	-78,011	Aksakov
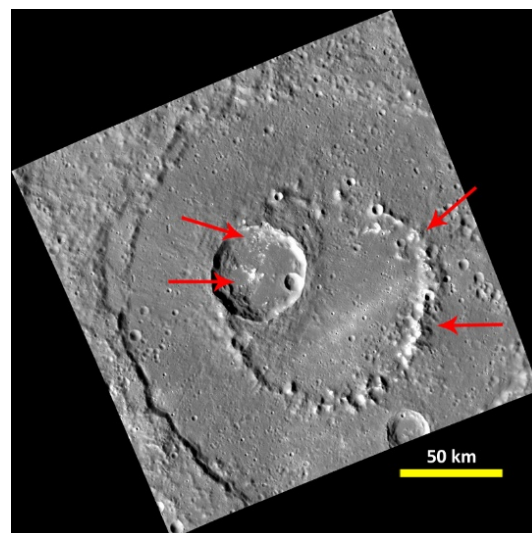
EW0259322404G

7011	35,05	-79,582	Unnamed crater
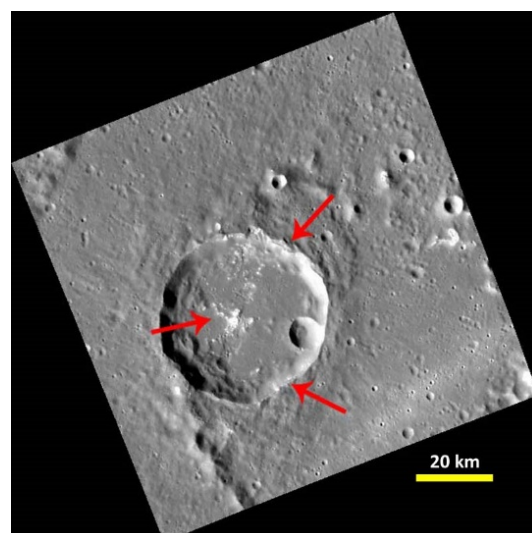
EW0213764708G

7014	32,626	-66,788	Jobim
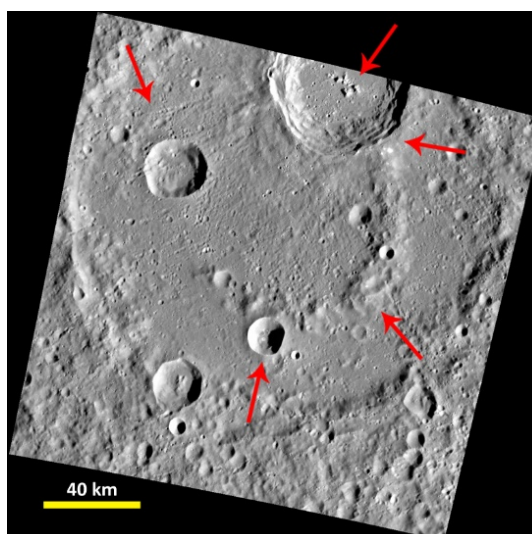
EW0254022495G

7015	45,161	-71,294	Unnamed crater	
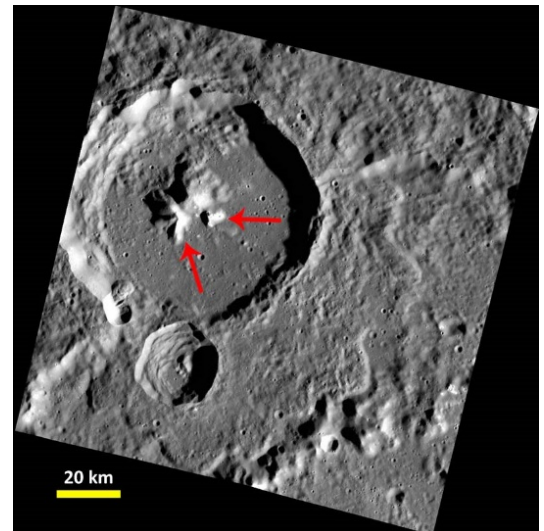
EW0238908808G

7016	51,5	-92,56	Sholem Aleichem	
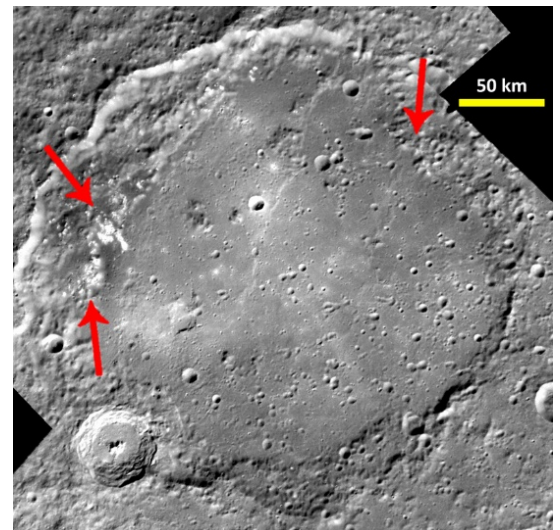
EW0211546814G and EW0211633839G

7018	40,705	-101,255	Scarlatti	
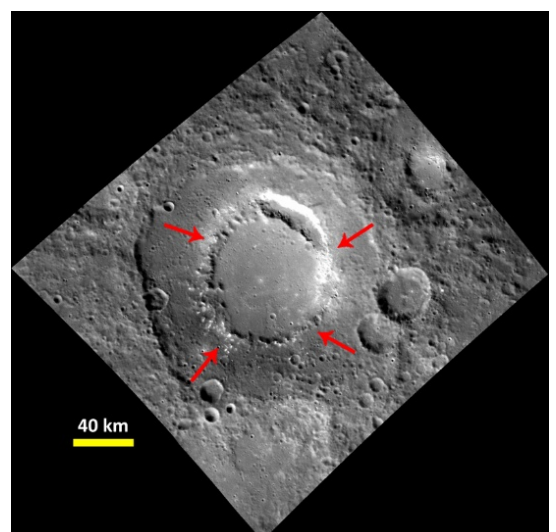
EW1023663791J

7025	41,394	-111,567	Whitman
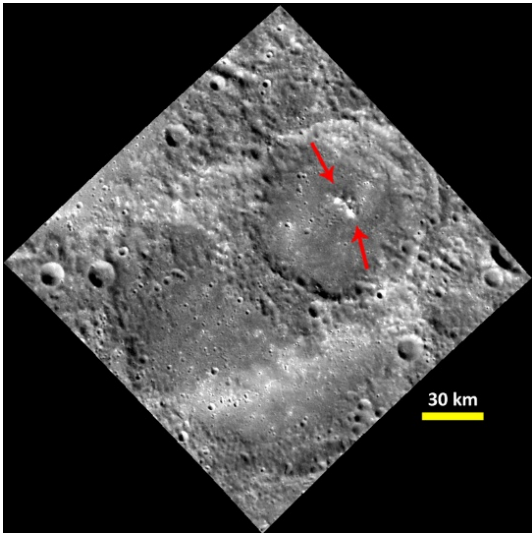
EW0259725508G

7028	39,143	-91,535	Al Hamadhani
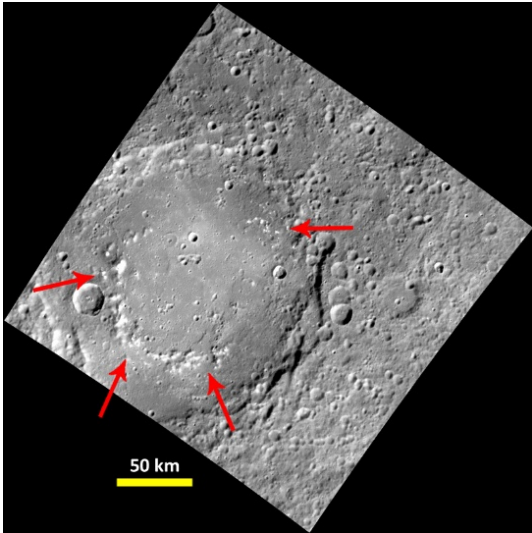
EW0241878696I

7029	38,976	-107,794	Unnamed crater
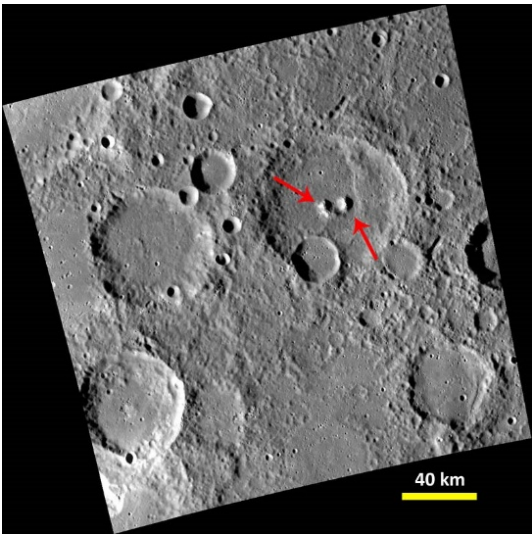
EW0247194282G

| 7033 | 39,976 | -80,259 | Unnamed crater |
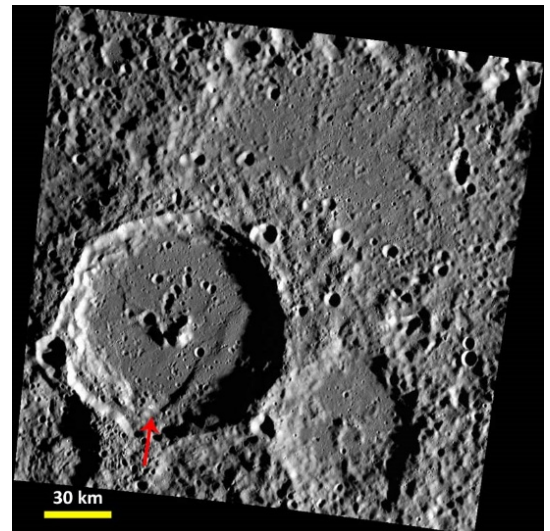
EW1003240513G

| 7059 | 41,752 | -84,535 | Unnamed crater |
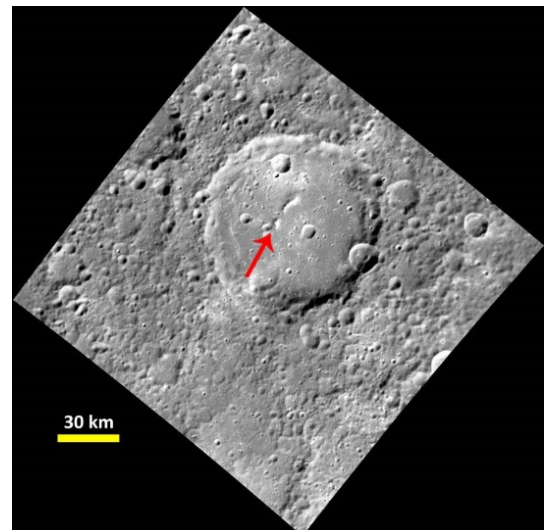
EW1006033281G

| 7070 | -0,976 | -73,192 | Boethius |
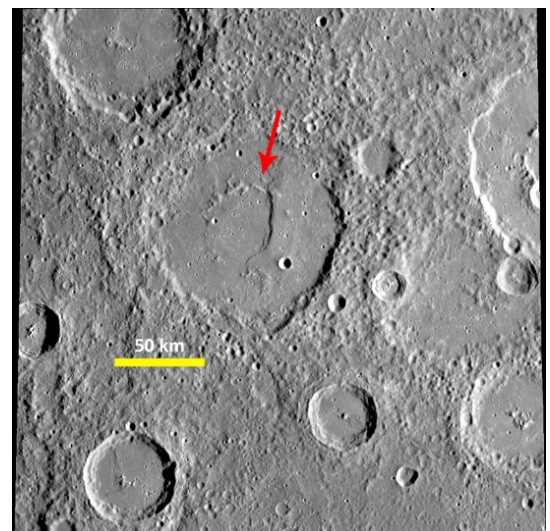
EW0239036965G

7072	23,512	-64,795	Not crater
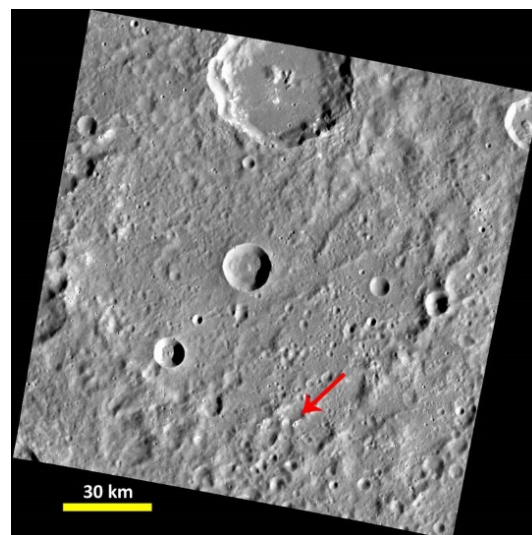
EW0223701935G

7073	21,917	-118,745	Durer
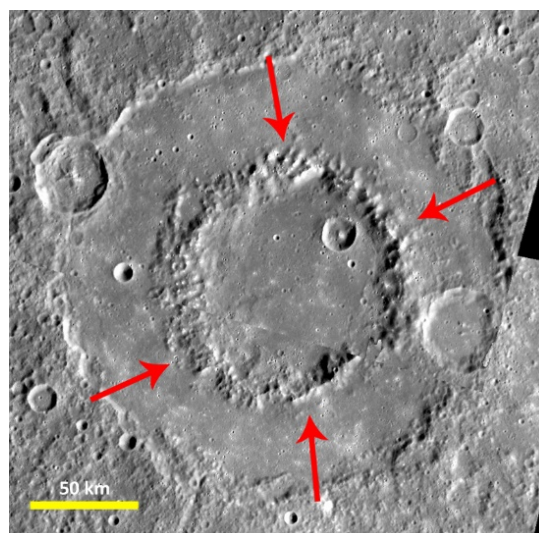
EW1006493663G and EW1006493777G

7112	23,025	-103,195	Mickiewicz
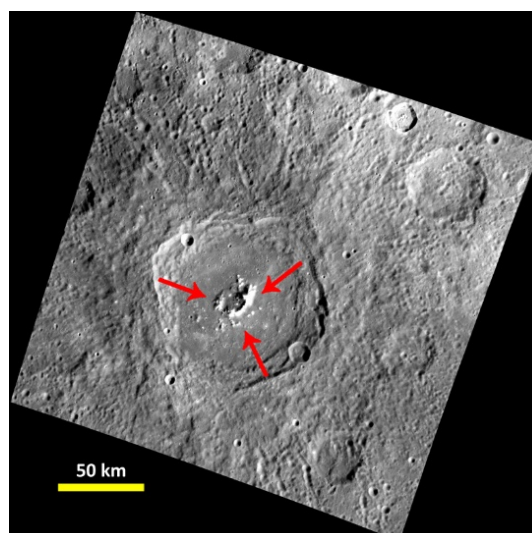
EW1006263338G

| 7113 | 26,294 | -113,344 | Unnamed crater |
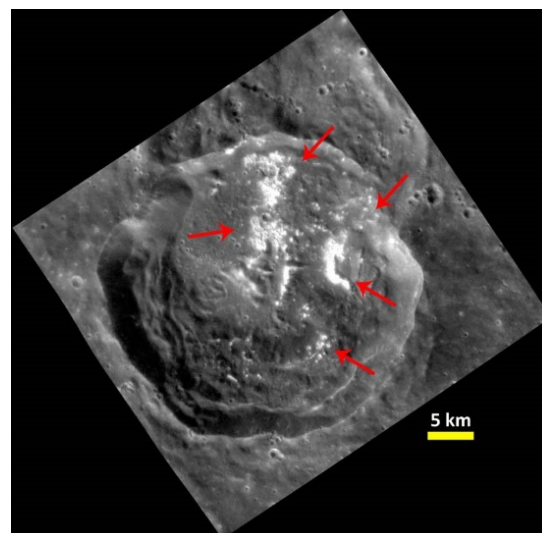
EN1008713791M

| 7119 | 25,383 | -105,991 | Not crater |
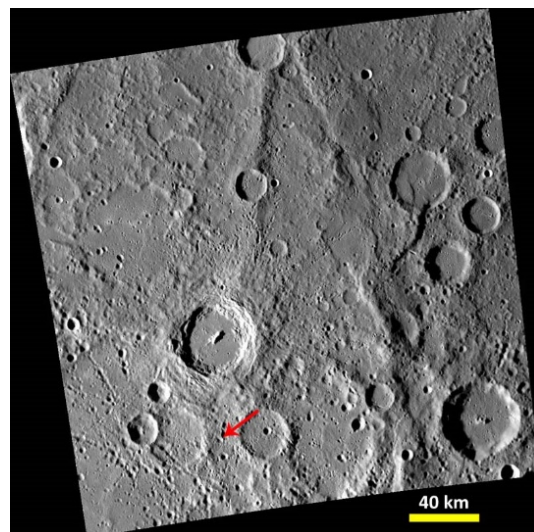
EW0247107643G

| 7120 | 9,322 | -104,432 | Wang Meng |
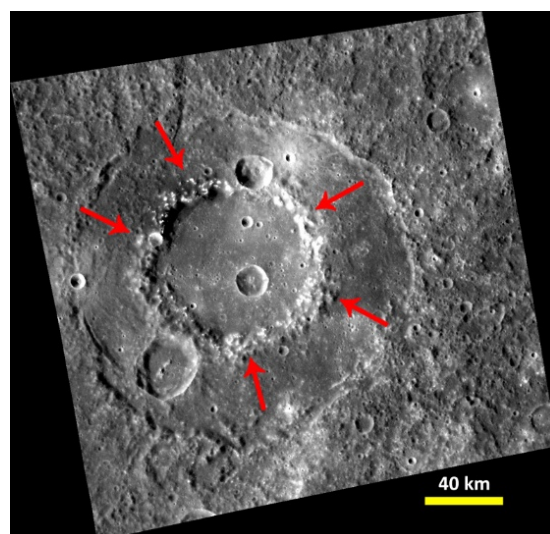
EW0244431096G

7122	17,431	-102,68	Unnamed crater
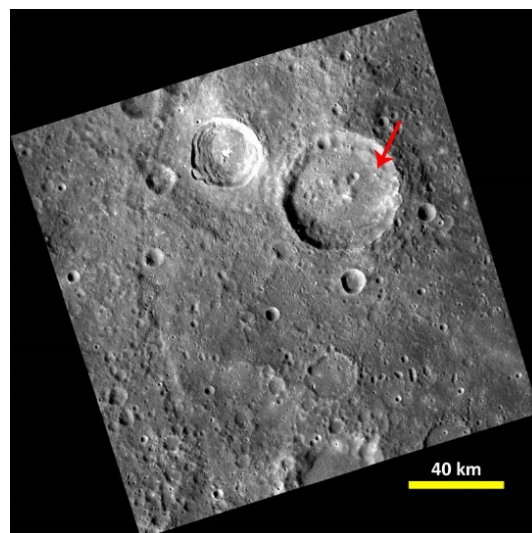
EW0244488547G

7123	18,963	-107,521	Unnamed crater
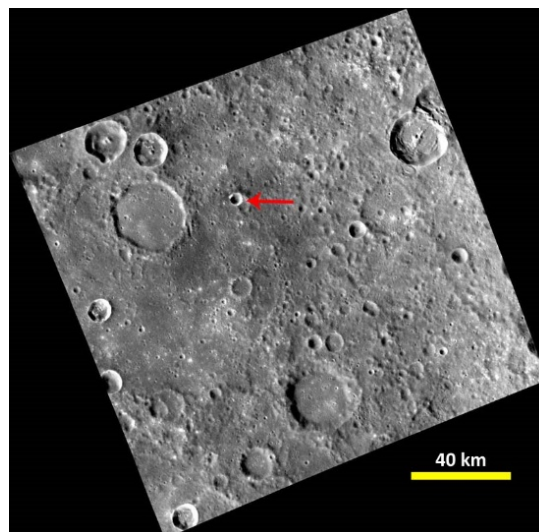
EW0244488492G

7124	15,028	-112,241	Glinka
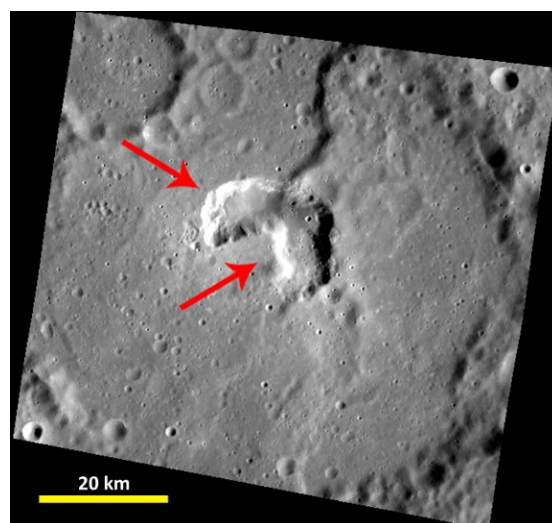
EW1067093278G

| 7130 | 16,339 | -70,807 | Unnamed crater |
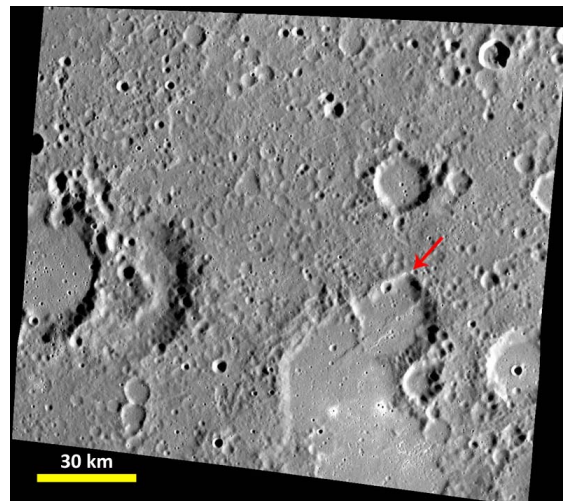
EW0223917530G

| 7131 | 14,135 | -86,179 | Vivaldi |
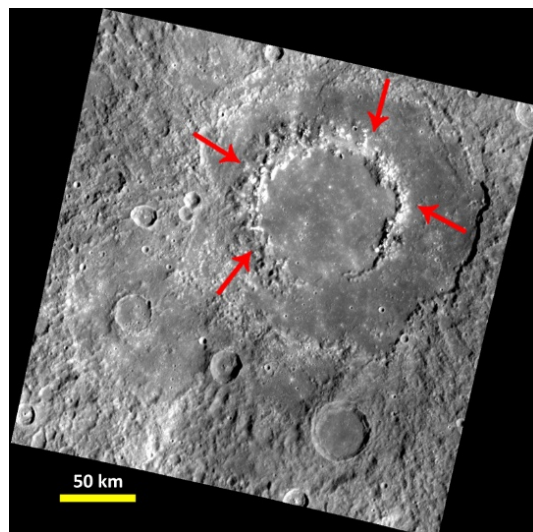
EW1005974980I

| 7136 | 10,74 | -107,774 | Judah Ha Levi |
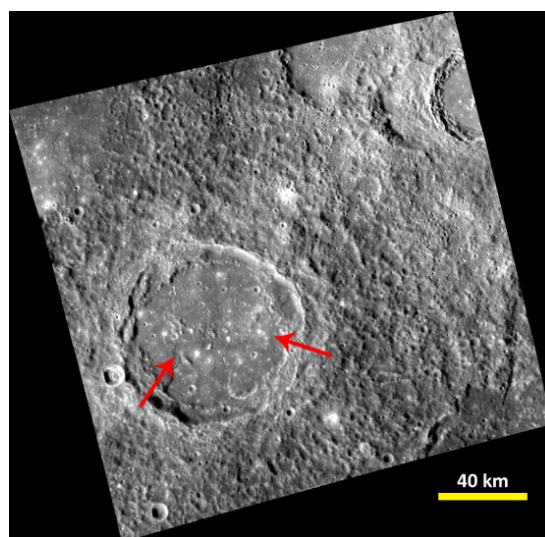
EW0244488637G

| 7137 | 25,072 | -95,329 | Unnamed crater |
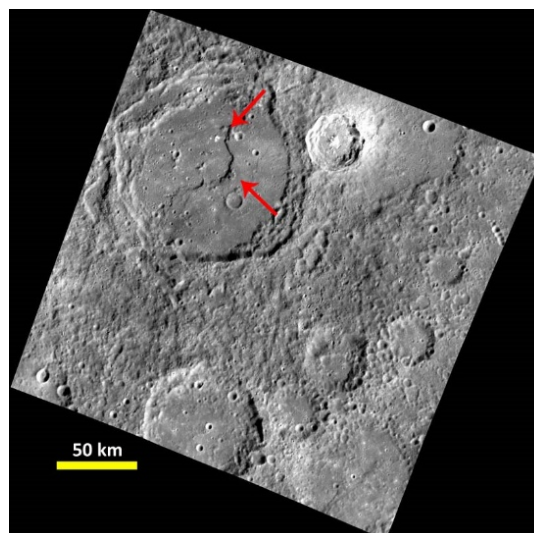
EW1006148119G

| 7138 | 22,217 | -67,584 | Catullus |
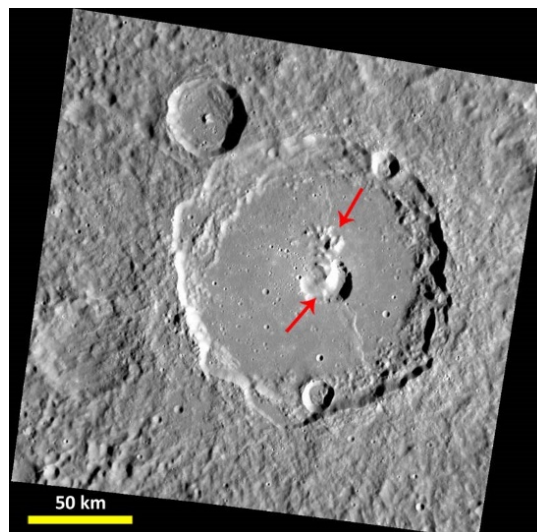
EW0223701985G

| 7139 | 21,52 | -75,048 | Unnamed crater |
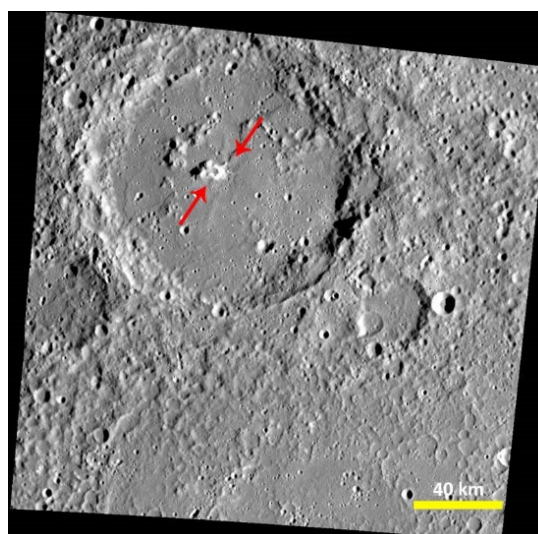
EW0254137945G

7144	25,079	-93,443	Du Fu
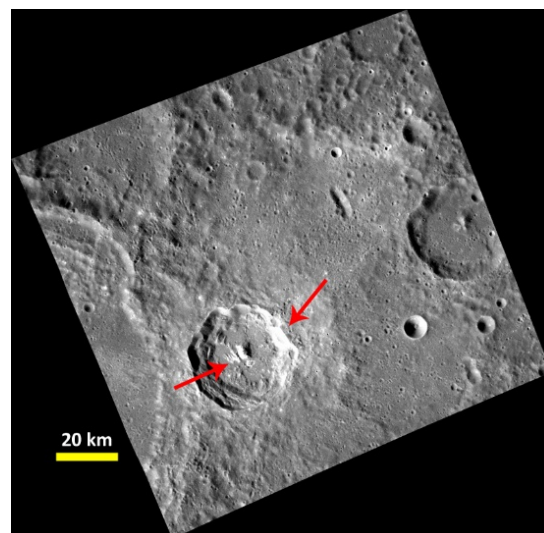
EW0229105588F

7147	8,473	-67,816	Unnamed crater
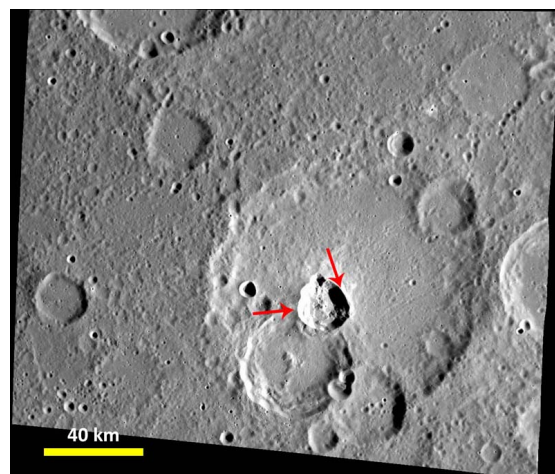
EW0223917664G

7148	4,033	-92,07	Unnamed crater
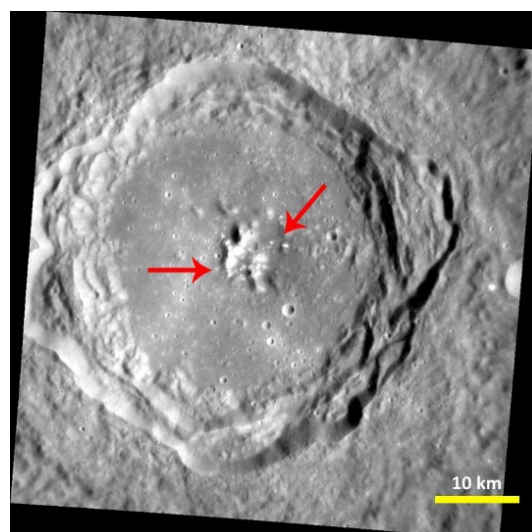
EN0256986726M

7153	1,933	-74,53	Unnamed crater
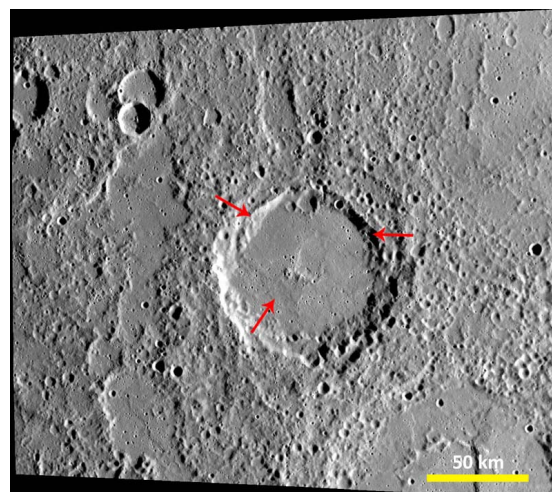
EW0224044850G

7155	-7,314	-66,92	Unnamed crater
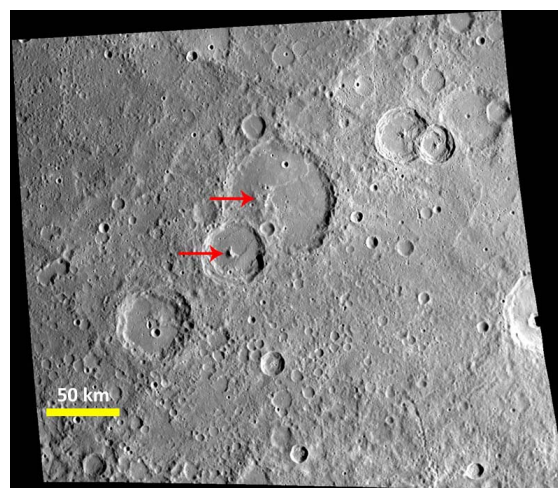
EW0239122006G

7156	8,224	-72,062	Unnamed crater
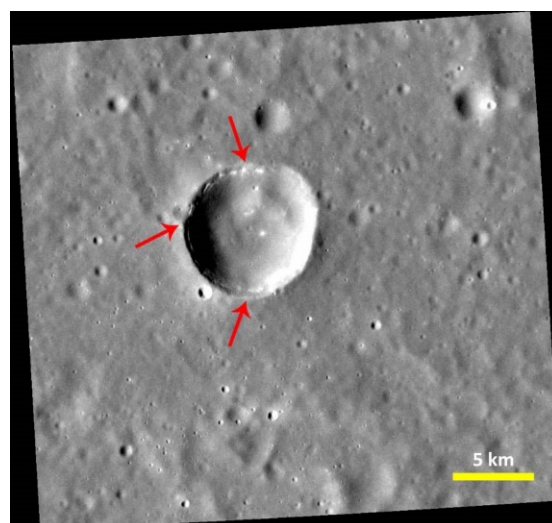
EN0244171913M

7169	16,475	-99,92	Unnamed crater
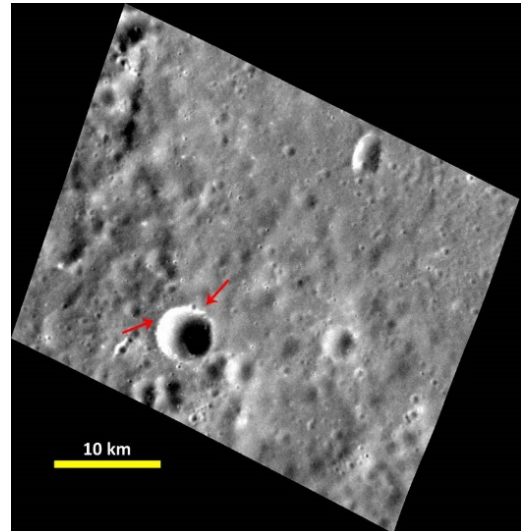
EN1021501748M

7172	39,23	-96,487	Not crater
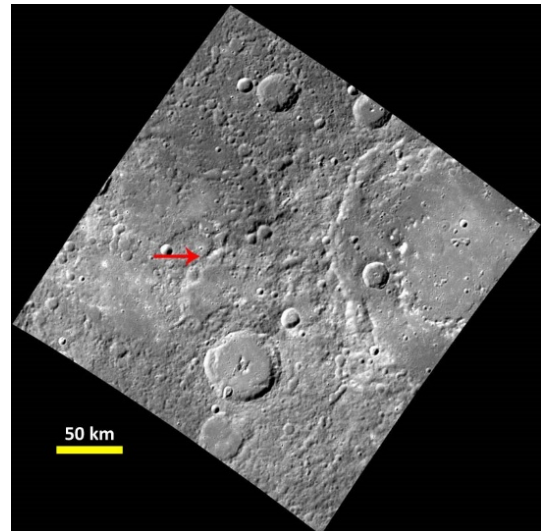
EW0226752816G

7176	30,05	-103,971	Not crater
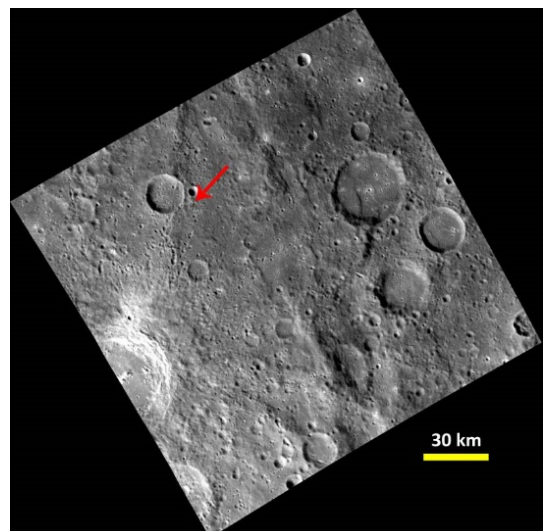
EW0259610509G

7177	21,311	-105,647	Not crater
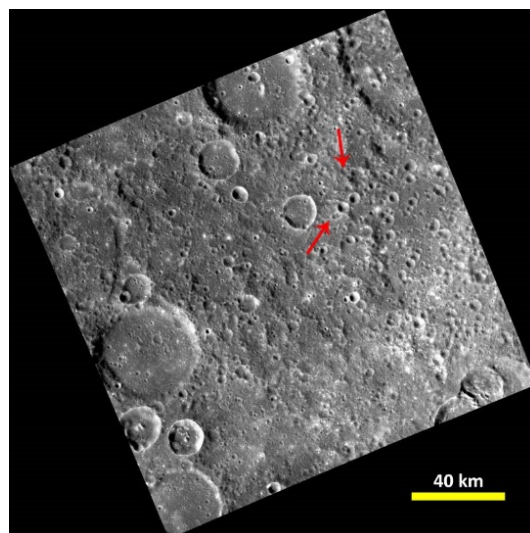
EW0244546074F

7179	40,056	-113,513	Unnamed crater
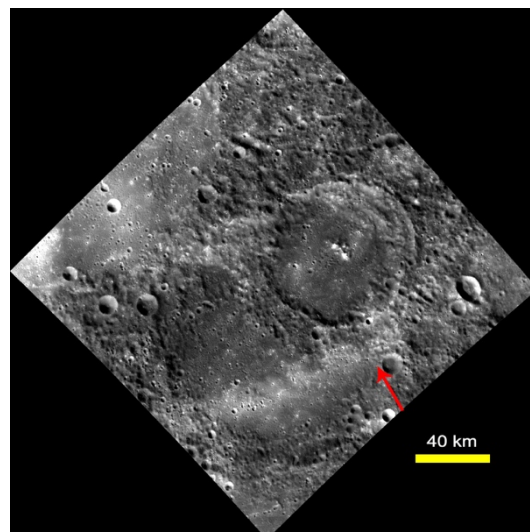
EW1008771167G

7180	55,963	-69,141	Unnamed crater
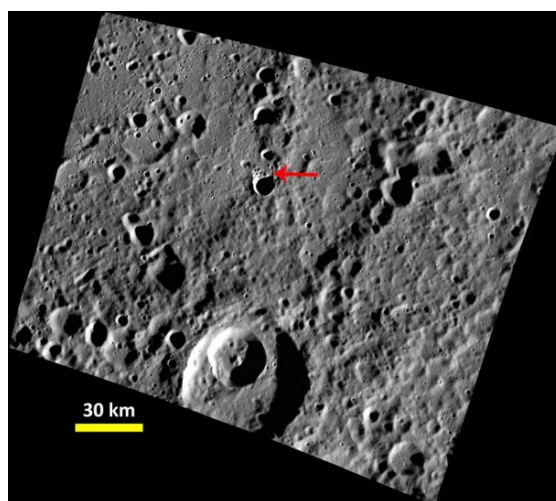
EW0223831018G

7183	46,621	-96,935	Not crater
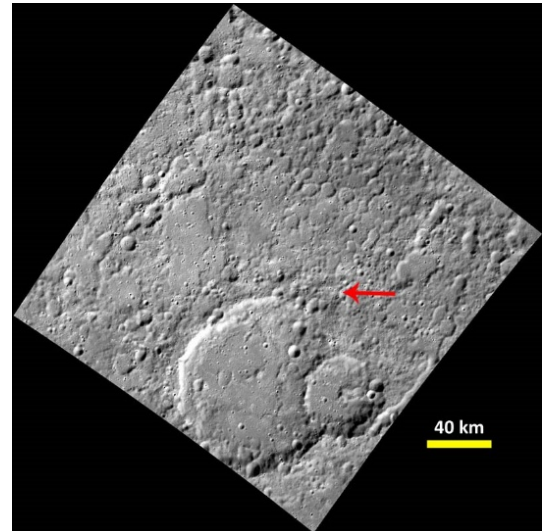
EW0242004187G

7184	36,448	-105,054	Not crater
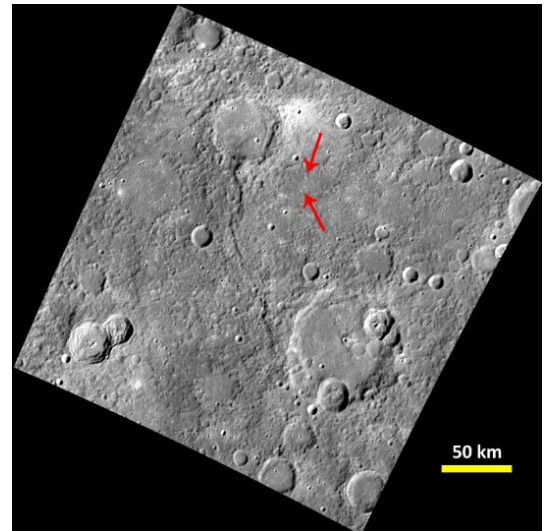
EW0242087490G

7185	47,565	-103,116	Not crater
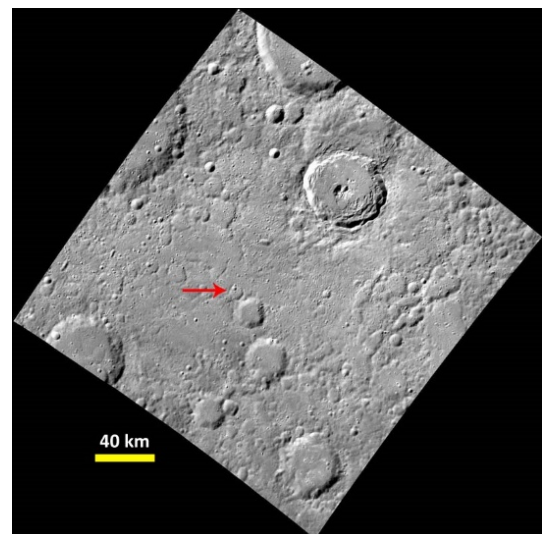
EW0226880033G

7193	29,209	-114,181	Unnamed crater
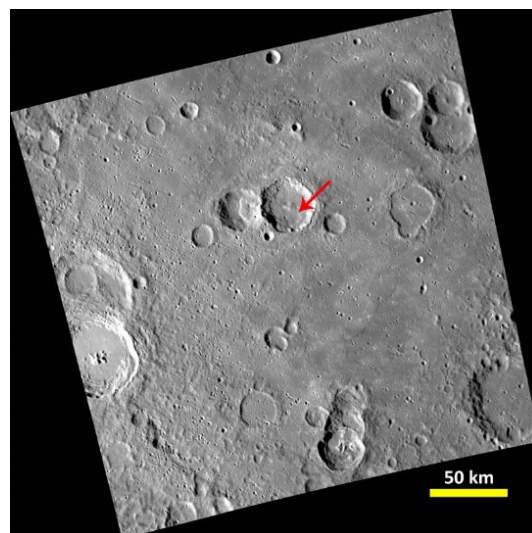
EW0247251664G

7194	35,319	-112,634	Gibran
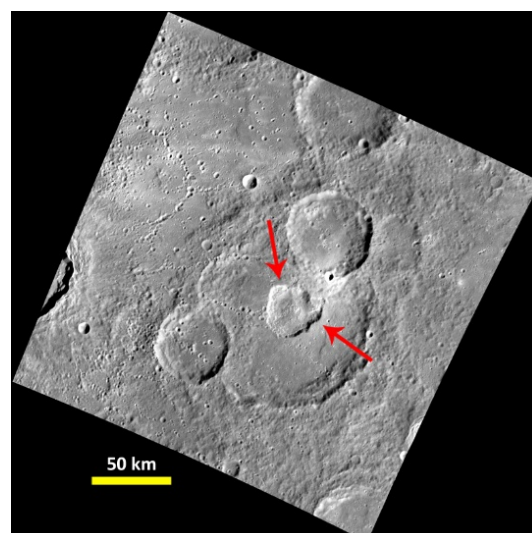
EW0242171073G

7195	38,046	-114,072	Not crater
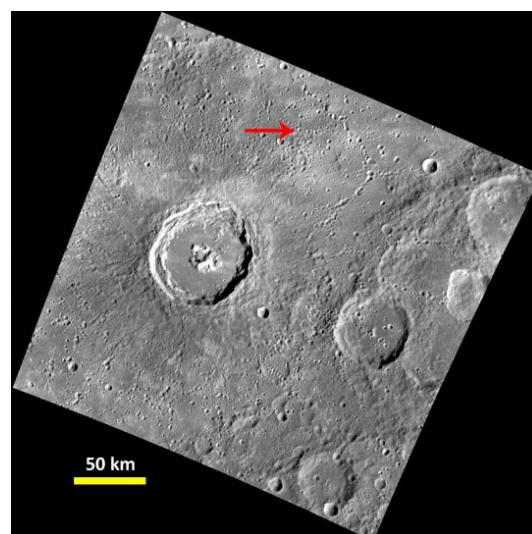
EW0242212846G

8184	12,216	-44,185	Unnamed crater
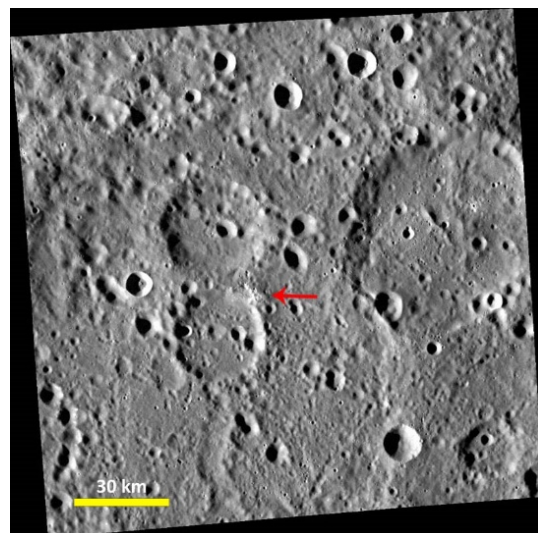
EW0213287022G

8187	10,565	-43,001	Unnamed crater
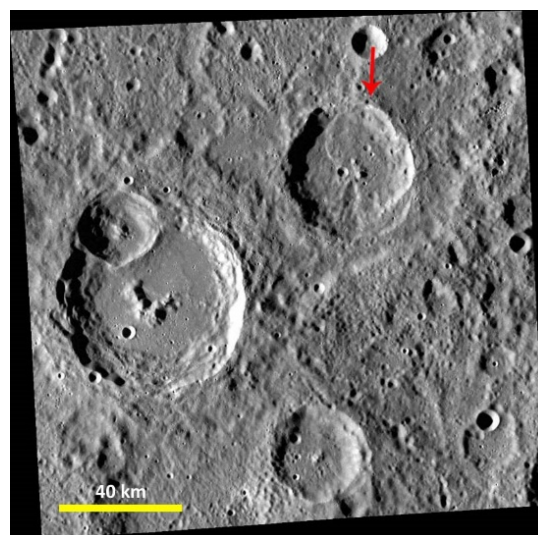
EW0213287080G

Bibliography

AHARONSON, O., Zuber, M. T. & Solomon, S. C. (2004). Crustal remanence in an internally magnetized non-uniform shell: a possible source for Mercury's magnetic field? *Earth and Planetary Science Letters, Vol. 218, Issue 3-4*, 261-268, DOI: 10.1016/S0012-821X(03)00682-4.

ANDERSON, J. D., Colombo, G., Espsitio, P. B., Lau, E. L. & Trager, G. B. (1987). The mass, gravity field, and ephemeris of Mercury. *Icarus, Vol. 71, Issue 3*, 337–349, DOI: 10.1016/0019-1035(87)90033-9.

ANDERSON, B. J., Acuňa, M. H., Lohr, D. A., Scheifele, J., Raval, A., Korth, H. & Slavin, J. A. (2007). The Magnetometer instrument on MESSENGER. *Space Science Reviews, Vol. 131, Issue 1-4*, 417-450, DOI: 10.1007/s11214-007-9246-7.

ANDREWS, G. B., Zurbuchen, T. H., Mauk, B. H., Malcom, H., Fisk, L. A., Gloeckler, G., Ho, G. C., Kelley, J. S., Koehn, P. L., Lefevere, T. W., Livi, S. S., Lundgren, R. A. & Raines, J. M. (2007). The Energetic Particle and Plasma Spectrometer instrument on the MESSENGER spacecraft. *Space Science Reviews, Vol. 131, Issue 1-4*, 523-556, DOI: 10.1007/s11214-007-9272-5.

BENKHOFF, J., van Casteren, J., Hayakawa, H., Fujimoto, M., Laakso, H., Novara, M., Ferri, P., Middleton, H. R. & Ziethe, R. (2010). BepiColombo - Comprehensive exploration of Mercury: Mission overview and science goals. *Planetary and Space Science, Vol. 58, Issue 1-2*, 2-20, DOI: 10.1016/j.pss.2009.09.020.

BLEWETT, D. T., Robinson, M. S., Denevi, B. W., Gillis-Davis, J. J., Head, J. W., Solomon, S. C., Holsclaw, G. M. & McClintock, W. E. (2009). Multispectral images of Mercury from the first MESSENGER flyby: Analysis of global and regional color trends. *Earth and Planetary Science Letters, Vol. 285, Issue 3-4*, 272–282, DOI: 10.1016/j.epsl.2009.02.021.

BLEWETT, D. T., Chabot, N. L., Denevi, B. W., Ernst, C. M., Head, J. W., Izenberg, N. R., Murchie, S. L., Solomon, S. C., Nittler, L. R., McCoy, T. J., Xiao, Z., Baker, D. M. H., Fassett, C. I., Braden, S. E., Oberst, J., Scholten, F., Preusker, F. & Hurwitz, D. M. (2011). Hollows on Mercury: MESSENGER evidence for geologically recent volatile-related activity. *Science, Vol. 333, Issue 6051*, 1856–1859, DOI: 10.1126/science.1211681.

BLEWETT, D. T., Vaughan, W. M., Xiao, Z., Chabot, N. L., Denevi, B. W., Ernst, C. M., Helbert, J., D'Amore, M., Maturilli, A., Head, J. W. & Solomon, S. C. (2013). Mercury's hollows: Constraints on formation and composition from analysis of geological setting and spectral reflectance. *Journal of Geophysical Research: Planets, Vol. 118, Issue 5*, 1013-1032, DOI: 10.1029/2012JE004174.

BLEWETT, D. T., Levy, C. L., Chabot, N. L., Denevi, B. W., Ernst, C. M. & Murchie, S. L. (2014). Phase-ratio images of the surface of Mercury: Evidence for differences in sub-resolution texture. *Icarus, Vol. 242*, 142–148, DOI: 10.1016/j.icarus.2014.08.024.

BLEWETT, D. T., Stadermann, A. C., Susorney, H. C., Ernst, C. M., Xiao, Z., Chabot, N. L., Denevi, B. W., Murchie, S. L., McCubbin, F. M., Kinczyk, M. J., Gillis-Davis, J. J. & Solomon, S. C. (2016). Analysis of MESSENGER high-resolution images of Mercury's hollows and implications for hollow formation. *Journal of Geophysical Research, Vol. 121, Issue 9*, 1798–1813, DOI: 10.1002/2016JE005070.

BROADFOOT, A. L., Kumar, S., Belton, M. J. S. & McElroy, M. B. (1974). Mercury's atmosphere from Mariner 10: Preliminary results. *Science, Vol. 185, Issue 4146*, 166-169, DOI: 10.1126/science.185.4146.166.

BROADFOOT, A. L., Shemansky, D. E. & Kumar, S. (1976). Mariner 10 - Mercury atmosphere. *Geophysical Research Letters, Vol. 3, Issue 10*, 577-580, 10.1029/GL003i010p00577.

BYRNE, P. K., Klimczak, C., Celâl Şengör, A. M., Solomon, S. C., Watters, T. R. & Hauck II, S. A., (2014). Mercury's global contraction much greater than earlier estimates. *Nature Geoscience, Vol. 7, Issue 4*, 301–307, DOI: 10.1038/ngeo2097.

CAVANAUGH, J. F., Smith, J. C., Sun, X., Bartels, A. E., Ramos-Izquierdo, L., Krebs, D. J., McGarry, J. F., Trunzo, R., Novo-Gradac, A. M., Britt, J. L., Karsh, J., Katz, R. B., Lukemire, A. T., Szymkiewicz, R., Berry, D. L., Swinski, J. P., Neumann, G. A., Zuber, M. T. & Smith, D. E. (2007). The Mercury Laser Altimeter Instrument for the MESSENGER mission. *Space Science Reviews, Vol. 131, Issue 1-4*, 451-479, DOI: 10.1007/s11214-007-9273-4.

CHASE, S. C., Miner, E. D., Morrison, D., Munch, G., Neugebauer, G. & Schroeder, M. (1974). Preliminary Infrared radiometry of the night side of Mercury from Mariner 10. *Science, Vol. 185, Issue 4146*, 142-145, DOI: 10.1126/science.185.4146.142.

COLOMBO, G. & Shapiro, I. I. (1966). The rotation of the planet Mercury. *Astrophysical Journal, Vol. 145*, 296-307, DOI: 10.1086/148762.

DAVIES, M. E., Dornik, S. E., Gault, D. E. & Strom, R. G. (1978). Atlas of Mercury. *NASA SP-423.*

DENEVI, B. W., Robinson, M. S., Solomon, S. C., Murchie, S. L., Blewett, D. T., Domingue, D. L., McCoy, T. J., Ernst, C. M., Head, J. W., Watters, T. R. & Chabot, N. L. (2009). The evolution of Mercury's crust: A global perspective from MESSENGER. *Science, Vol. 324, Issue 5927*, 613-618, DOI: 10.1126/science.1172226.

DOMINGUE, D. L., Koehn, P. L., Killen, R. M., Sprague, A. L., Sarantos, M., Cheng, A. F., Bradley, E. T. & McClintock, W. E. (2007). Mercury's atmosphere: A surface-bounded exosphere. *Space Science Reviews, Vol. 131, Issue 1-4*, 161-186, DOI: 10.1007/s11214-007-9260-9.

DZURISIN, D. (1977). Mercurian bright patches: Evidence for physio-chemical alteration of surface material? *Geophysical Research Letters, Vol. 4, Issue 10*, 383-386, DOI: 10.1029/GL004i010p00383.

EINSTEIN A. (1915). Erklarung der perihelionbewegung der Merkur aus der allgemeinen relativitatstheorie. *Sitzungsber. preuss.Akad. Wiss., Vol. 47, No. 2*, 831-839.

EVANS, L. G., Peplowski, P. N., Rhodes, E. A., Lawrence, D. J., McCoy, T. J., Nittler, L. R., Solomon, S. C., Sprague, A. L., Stockstill-Cahill, K. R., Starr, R. D., Weider, S. Z., Boynton, W. V., Hamara, D. K. & Goldsten, J. O. (2012). Major-element abundances on the surface of Mercury: Results from the MESSENGER Gamma-Ray Spectrometer. *Journal of Geophysical Research, Vol. 117, Issue 11, No. E00L07*, DOI: 10.1029/2012JE004178.

FASSETT, C. I., Kadish, S. J., Head, J. W., Solomon, S. C. & Strom, R. G. (2011). The global population of large craters on Mercury and comparison with the Moon. *Geophysical Research Letters, Vol. 38, Issue 10, No. L10202*, DOI: 10.1029/2011GL047294.

FRANK, E. A., Potter, R. W. K., Abramov, O., James, P. B., Klima, R. L., Mojzsis, S. J. & Nittler, L. R. (2017). Evaluating an impact origin for Mercury's high-magnesium region. *Journal of Geophysical Research: Planets, Vol. 122, Issue 3*, 614-632, DOI: 10.1002/2016JE005244.

GILLIS-DAVIS, J. J., Blewett, D. T., Gaskell, R. W., Denevi, B. W., Robinson, M. S., Strom, R. G., Solomon, S. C. & Sprague A. L. (2009). Pit-floor craters on Mercury: Evidence for near-surface igneous activity. *Earth and Planetary Science Letters, Vol. 285, Issue 3-4*, 243–250, DOI: 10.1016/j.epsl.2009.05.023.

GOLDSTEN, J. O., Rhodes, E. A., Boynton, W. V., Feldman, W. C., Lawrence, D. J., Trombka, J. I., Smith, D. M., Evans, L. G., White, J., Madden, N. W., Berg, P. C., Murphy, G. A., Gurnee, R. S., Strohbehn, K., Williams, B. D., Schaefer, E. D., Monaco, C. A., Cork, C. P., Del Eckels, J., Miller, W. O., Burks, M. T., Hagler, L. B., Deteresa, S. J. & Witte, M. C. (2007). The MESSENGER Gamma-Ray and Neutron Spectrometer. *Space Science Reviews, Vol. 131, Issue 1-4*, 339-391, DOI: 10.1007/s11214-007-9262-7.

HARTMANN, W. K. & Wood, C. A. (1971). Moon: Origin and evolution of multi-ring basins. *The Moon, Vol. 3, Issue 1*, 3-78, DOI: 10.1007/BF00620390

HAUCK, S. A. II, Margot, J. L., Solomon, S. C., Phillips, R. J., Johnson, C. L., Lemoine, F. G., Mazarico, E., McCoy, T. J., Padovan, S., Peale, S. J., Perry, M. E., Smith, D. E. & Zuber, M. T. (2013). The curious case of Mercury's internal structure. *Journal of Geophysical Research: Planets, Vol. 118, Issue 6*, 1204–1220, DOI: 10.1002/jgre.20091.

HAWKINS, S. E., Boldt, J. D., Darlington, E. H., Espiritu, R., Gold, R. E., Gotwols, B., Grey, M. P., Hash, C. D., Hayes, J. R., Jaskulek, S. E., Kardian, C. J., Keller, M. R., Malaret, E. R., Murchie, S. L., Murphy, P. K., Peacock, K., Prockter, L. M., Reiter, R. A., Robinson, M. S., Schaefer, E. D., Shelton, R. G., Sterner, R. E., Taylor, H. W., Watters, T. R. & Williams, B. D. (2007). The Mercury Dual Imaging System on the MESSENGER Spacecraft. *Space Science Reviews, Vol. 131, Issue 1-4*, 247-338, DOI: 10.1007/s11214-007-9266-3.

HAYAKAWA, H., Kasaba, Y., Yamakawa, H., Ogawa, H. & Mukai, T. (2004). The Bepi-Colombo/MMO model payload and operation plan. *Advances in Space Research, Vol. 33, Issue 12*, 2142-2146, DOI: 10.1016/S0273-1177(03)00438-1.

HEAD, J. W., Chapman, C. R., Strom, R. G., Fassett, C. I., Denevi, B. W., Blewett, D. T., Ernst, C. M., Watters, T. R., Solomon, S. C., Murchie, S. L., Prockter, L. M., Chabot, N. L., Gillis-Davis, J. J., Whitten, J. L., Goudge, T. A., Baker, D. M. H., Hurwitz, D. M., Ostrach, L. R., Xiao, Z., Merline, W. J., Kerber, L., Dickson, J. L., Oberst, J., Byrne, P. K., Klimczak, C. & Nittler, L. R. (2011). Flood volcanism in the northern high latitudes of Mercury revealed by MESSENGER. *Science, Vol. 333, Issue 6051*, 1853–1856, DOI: 10.1126/science.1211997.

KLIMA, R. L., D'Amore, M., Denevi, B. W., Ernst, C. M., Gillis-Davis, J. J., Helbert, J., Izenberg, N. R., Pashai, P., Strom, R. G. & Vilas, F. (2011). Spectral properties of an unusual impact melt flow on Mercury: Integrating color imagery with spectral data acquired by Mascs on MESSENGER. *Geological Society of America Abstracts with Programs, Vol. 43, No. 5*, 360.

LOWELL, P. (1897). Drawings of Mercury. *Astronomische Nachrichten, Vol. 142, Issue 23*, DOI: 10.1002/asna.18971422306.

LUCCHETTI, A., Pajola, M., Galluzzi, V., Giacomini, L., Carli, C., Cremonese, G., Marzo, G. A., Ferrari, S., Massironi, M. & Palumbo P. (2018). Mercury hollows as remnants of original bedrock materials and devolatilization process: A spectral clustering and geomorphological analysis. *Journal of Geophysical Research: Planets, Vol. 123*.

MCCLINTOCK, W. E. & Lankton, M. R. (2007). The Mercury Atmospheric and Surface Composition Spectrometer for the MESSENGER mission. *Space Science Reviews, Vol. 131, Issue 1-4*, 481-521, DOI: 10.1007/s11214-007-9264-5.

MCCLINTOCK, W. E., Burger, M., Cassidy, T., Killen, R., Merkel, A., Sarantos, M. & Vervack, R. (2016). Mercury's surface-bounded exosphere as seen from orbit during the MESSENGER mission: Mercury Atmospheric and Surface Composition Spectrometer results. *EGU General Assembly 2016, id. EPSC2016-11019.*

MORGAN, J. W. & Anders, E. (1980). Chemical composition of Earth, Venus, and Mercury. *Proceedings of the National Academy of Sciences of the USA, Vol. 77, Issue 12,* 6973–6977, DOI: 10.1073/pnas.77.12.6973.

MURRAY, B. C., Belton, M. J. S., Danielson, G. E., Davies, M. E., Gault, D. E., Hapke, B., O'Leary, B., Strom, R. G., Suomi, V. & Trask, N. (1974). Mercury's surface: Preliminary description and interpretation from Mariner 10 pictures. *Science, Vol. 185, Issue 4146,* 169-179, DOI: 10.1126/science.185.4146.169.

MURRAY, B. C. (1975). The Mariner 10 pictures of Mercury - an overview. *Journal of Geophysical Research, Vol. 80, Issue 17,* 2342-2344, DOI: 10.1029/JB080i017p02342.

NAMUR, O., Collinet, M., Charlier, B., Grove, T. L., Holtz, F. & McCammon, C. (2016). Melting processes and mantle sources of lavas on Mercury. *Earth and Planetary Science Letters, Vol. 439,* 117–128, DOI: 10.1016/j.epsl.2016.01.030.

NESS, N. F., Behannon, K. W., Lepping, R. P., Whang, Y. C. & Schatten, K. H. (1974). Magnetic field observations near Mercury: Preliminary results from Mariner 10. *Science, Vol. 185, Issue 4146,* 151-160, DOI: 10.1126/science.185.4146.151.

NESS, N. F., Behannon, K. W., Lepping, R. P. & Whang, Y. C. (1975). Magnetic field of Mercury confirmed. *Nature, Vol. 255,* 204-205, DOI: 10.1038/255204a0.

NEUKUM, G., Oberst, J., Hoffmann, H., Wagner, R. & Ivanov, B. A. (2001). Geologic evolution and cratering history of Mercury. *Planetary and Space Science, Vol. 49, Issue 14-15,* 1507-1521, DOI: 10.1016/S0032-0633(01)00089-7.

NITTLER, L. R., Starr, R. D., Weider, S. Z., McCoy, T. J., Boynton, W. V., Ebel, D. S., Ernst, C. M., Evans, L. G., Goldsten, J. O., Hamara, D. K., Lawrence, D. J., McNutt Jr., R. L., Schlemm II, C. E., Solomon, S. C. & Sprague, A. L. (2011). The major-element composition of Mercury's surface from MESSENGER X-ray spectrometry. *Science, Vol. 333, Issue 6051,* 1847–1850, DOI: 10.1126/science.1211567.

OGILVIE, K. W., Scudder, J. D., Hartle, R. E., Siscoe, G. L., Bridge, H. S., Lazarus, A. J., Asbridge, J. R., Bame, S. J. & Yeates, C. M. (1974). Observations at Mercury encounter by the Plasma Science Experiment on Mariner 10. *Science, Vol. 185, Issue 4146,* 145-151, DOI: 10.1126/science.185.4146.145.

PEPLOWSKI, P. N., Evans, L. G., Hauck II, S. A., McCoy, T. J., Boynton, W. V., Gillis-Davis, J. J., Ebel, D. S., Goldsten, J. O., Hamara, D. K., Lawrence, D. J., McNutt Jr., R. L., Nittler, L. R., Solomon, S. C., Rhodes, E. A., Sprague, A. L., Starr, R.

D. & Stockstill-Cahill, K. R. (2011). Radioactive elements on Mercury's surface from MESSENGER: Implications for the planet's formation and evolution. *Science, Vol. 333, Issue 6051*, 1850–1852, DOI: 10.1126/science.1211576.

PEPLOWSKI, P. N., Lawrence, D. J., Rhodes, E. A., Sprague, A. L., McCoy, T. J., Denevi, B. W., Evans, L. G., Head, J. W., Nittler, L. R., Solomon, S. C., Stockstill-Cahill, K. R. & Weider, S. Z. (2012). Variations in the abundances of Potassium and Thorium on the surface of Mercury: results from the MESSENGER Gamma-Ray Spectrometer. *Journal of Geophysical Research, Vol. 117, Issue E12, No. E00L04*, DOI: 10.1029/2012JE004141.

PEPLOWSKI, P. N., Evans, L. G., Stockstill-Cahill, K. R., Lawrence, D. J., Goldsten, J. O., McCoy, T. J., Nittler, L. R., Solomon, S. C., Sprague, A. L., Starr, R. D. & Weider, S. Z. (2014). Enhanced Sodium abundance in Mercury's north polar region revealed by the MESSENGER Gamma-Ray Spectrometer. *Icarus, Vol. 228*, 86–95, DOI: 10.1016/j.icarus.2013.09.007.

PEPLOWSKI, P. N., Lawrence, D. J., Feldman, W. C., Goldsten, J. O., Bazell D., Evans, L. G., Head, J. W., Nittler, L. R., Solomon, S. C. & Weider S. Z. (2015). Geochemical terranes of Mercury's northern hemisphere as revealed by MESSENGER neutron measurements. *Icarus, Vol. 253*, 346-363, DOI: 10.1016/j.icarus.2015.02.002.

PEPLOWSKI, P. N., Klima, R. L., Lawrence, D. J., Ernst, C. M., Denevi, B. W., Frank, E. A., Goldsten, J. O., Murchie, S. L., Nittler, L. R. & Solomon, S. C. (2016). Remote sensing evidence for an ancient carbon-bearing crust on Mercury. *Natural Geoscience, Vol. 9*, 273–276, DOI: 10.1038/NGEO2669.

SCHLEMM, C. E., Starr, R. D., Ho, G. C., Bechtold, K. E., Hamilton, S. A., Boldt, J. D., Boynton, W. V., Bradley, W., Fraeman, M. E., Gold, R. E., Goldsten, J. O., Hayes, J. R., Jaskulek, S. E., Rossano, E., Rumpf, R. A., Schaefer, E. D., Strohbehn, K., Shelton, R. G., Thompson, R. E., Trombka, J. I. & Williams, B. D. (2007). The X-Ray Spectrometer on the MESSENGER spacecraft. *Space Science Reviews, Vol. 131, Issue 1-4*, 393-415, DOI: 10.1007/s11214-007-9248-5.

SIEGFRIED, R. W. II, & Solomon, S. C. (1974). Mercury: Internal structure and thermal evolution. *Icarus, Vol. 23, Issue 2*, 192–205, DOI: 10.1016/0019-1035(74)90005-0 .

SIMPSON, J. A., Eraker, J. H., Lamport, J. E. & Walpole, P. H. (1974). Electrons and protons accelerated in Mercury's magnetic field. *Science, Vol. 185, Issue 4146*, 160-166, DOI: 10.1126/science.185.4146.160.

SMITH, D. E., Zuber, M. T., Phillips, R. J., Solomon, S. C., Hauck, S. A., Lemoine, F. G., Mazarico, E., Neumann, G. A., Peale, S. J., Margot, J., Johnson, C. L., Torrence, M. H., Perry, M. E., Rowlands, D. D., Goossens, S., Head, J. W. & Taylor, A. H. (2012). Gravity field and internal structure of Mercury from MESSENGER. *Science, Vol. 336, Issue 6078*, 214-217, DOI: 10.1126/science.1218809.

SOLOMON, S. C., McNutt, R. L., Gold, R. E. & Domingue, D. L. (2007). MESSENGER Mission Overview. *Space Science Reviews, Vol. 131, Issue 1-4*, 3-39, DOI: 10.1007/s11214-007-9247-6.

SPUDIS, P. D. & Guest, J. E. (1988). Stratigraphy and geologic history of Mercury. In: Vilas, F., Chapman, C.R., Matthews, M.S. (Eds.), Mercury. *University of Arizona Press, Tucson, AZ*, 118–164.

SRINIVASAN, D. K., Perry, M. E., Fielhauer, K. B., Smith, D. E. & Zuber, M. T. (2007). The Radio Frequency Subsystem and Radio Science on the MESSENGER mission. *Space Science Reviews, Vol. 131, Issue 1-4*, 557-571, DOI: 10.1007/s11214-007-9270-7.

STEPHENSON, A. (1976). Crustal remanence and the magnetic moment of Mercury. *Earth and Planetary Science Letters, Vol. 28, Issue 3*, 454-458, DOI: 10.1016/0012-821X(76)90206-5.

STROM, R. G. (1997). Mercury – an overview. *Advances in Space Research, Vol. 19, Issue 10*, 1471-1485, DOI: 10.1016/S0273-1177(97)00346-3.

STROM, R. G., Chapman, C. R., Merline, W. J., Solomon, S. C. & Head J. W. (2008). Mercury cratering record viewed from MESSENGER's first flyby, *Science, Vol. 321, Issue 5885*, 79–81, DOI: 10.1126/science.1159317.

THOMAS, R. J., Rothery, D. A., Conway, S. J. & Anand, M. (2014). Hollows on Mercury: Materials and mechanisms involved in their formation. *Icarus, Vol. 229*, 221–235. DOI: 10.1016/j.icarus.2013.11.018.

THOMAS, R. J., Hynek, B. M., Rothery, D. A. & Conway, S. J. (2016). Mercury's low-reflectance material: Constraints from hollows. *Icarus, Vol. 277*, 455–465, DOI: 10.1016/j.icarus.2016.05.036.

VANDER KAADEN, K. E. & McCubbin, F. M. (2015). Exotic crust formation on Mercury: Consequences of a shallow, FeO-poor mantle. *Journal of Geophysical Research: Planets, Vol. 120, Issue 2*, 195–209, DOI: 10.1002/2014JE004733.

VASAVADA, A. R., Paige, D. A. & Wood, S. E. (1999). Near-surface temperatures on Mercury and the Moon and the stability of polar ice deposits. *Icarus, Vol. 141, Issue 2*, 179-193, DOI: 10.1006/icar.1999.6175.

VAUGHAN, W. M., Helbert, J., Blewett, D. T., Head, J. W., Murchie, S. L., Gwinner, K., McCoy, T. J. & Solomon, S. C. (2012). Hollowforming layers in impact craters on Mercury: Massive sulfide deposits formed by impact melt differentiation? *Lunar and Planetary Science, Vol. 43*, abstract 1187.

WEIDER, S. Z., Nittler, L. R., Starr, R. D., Crapster-Pregont, E. J. & Solomon, S. C. (2014). Geochemical terranes on the innermost planet: Possible origins of Mercury's high-Magnesium region. *45th Lunar and Planetary Science Conference, LPI Contribution No. 1777*, 1866.

WEIDER, S. Z., Nittler, L. R., Starr, R. D., Crapster-Pregont, E. J., Peplowski, P. N., Denevi, B. W., Head, J. W., Byrne, P. K., Hauck II, S. A., Ebel, D. S. & Solomon, S. C. (2015). Evidence for geochemical terranes on Mercury: Global mapping of major elements with MESSENGER's X-Ray Spectrometer. *Earth and Planetary Science Letters, Vol. 416*, 109–120, DOI: 10.1016/j.epsl.2015.01.023.

WICHT, J. & Heyner, D. (2017). Mercury's magnetic field in the MESSENGER era. *Planetary Geodesy and Remote Sensing*, 223-262, DOI: 10.1201/b17624-11.

XIAO, Z., Strom, R. G., Blewett, D. T., Byrne, P. K., Solomon, S. C., Murchie, S. L., Sprague, A. L., Domingue, D. L. & Helbert, J. (2013). Dark spots on Mercury: A distinctive low-reflectance material and its relation to hollows. *Journal of Geophysical Research: Planets, Vol. 118, Issue 9*, 1752–1765, DOI: 10.1002/jgre.20115.

Acknowledgements

First, I wish to acknowledge the help provided by Prof. Francesco Marzari, who gave me the possibility to pursue a project in the field of planetary science.

I would like to offer my special thanks to Dr. Gabriele Cremonese and Dr. Alice Lucchetti for their tireless supervision of all the work I performed during my internship and the development of this thesis.

A great appreciation to all the beautiful people I met during the Master years in Padova and during my Erasmus+ in Liège, you made me feel less lonely so far from home.

Thanks to all my friends: if 'friends are the family you choose', I could not have made a better choice.

Thanks to all my family, who gave me confidence and supported me and my anxiety unconditionally. Dear beloved granny Luisa, this thesis is dedicated to you.